Title

Characterization of the Catalytic Life-Cycle of Metal Organic Framework UiO-66 in Methanol and Isopropanol Dehydration Catalysis

Author

Conley, Edward Thomas

Publication Date

2022

Characterization of the Catalytic Life-Cycle of Metal Organic Framework UiO-66 in Methanol and Isopropanol Dehydration Catalysis

By

EDWARD THOMAS CONLEY
DISSERTATION

Submitted in partial satisfaction of the requirements for the degree of

DOCTOR OF PHILOSOPHY

in

Materials Science and Engineering

in the

OFFICE OF GRADUATE STUDIES

of the

UNIVERSITY OF CALIFORNIA

DAVIS

Approved:

Bruce C. Gates, Chair

Jeffery C. Gibeling

Ricardo H. R. Castro

Committee in Charge

2022

ABSTRACT. Metal organic frameworks (MOFs) are a novel class of solid materials, comprising inorganic metal nodes and multidentate organic ligands. These materials have drawn wide attention as potential catalysts. Microscopic characterization of these structures has become routine with x-ray diffraction (XRD) crystallography and determination of surface area/pore volume data by analysis of adsorption isotherms, analyzed with Brunauer-Emmett-Teller (BET) theory. However, competition for the nodes in synthesis between the organic linkers, acid modulators, and the solvent matrix results in structural defects that are not resolved by these microscopic techniques. These defects are capped with inhibiting ligands that block access to catalytically active sites. Alcohol dehydration reactions offer opportunities to investigate these active sites as reactant alcohol will remove the inhibiting capping species, and (more slowly) the organic linker. Revealed vacancies will expose different active sites capable of catalyzing alcohol dehydration reactions. MOF UiO-66, which incorporates Zr_6O_8 nodes and 1,4-benzene dicarboxylate linkers and is known for its stability, was investigated with methanol and isopropanol dehydration as test reactions. Catalyst performance was determined with a once-through flow reactor at atmospheric pressure and temperatures of 473–573 K. The products were analyzed by on-line gas chromatography, and catalyst samples removed from the reactor after various times on stream were characterized by X-ray diffraction crystallography, surface area measurements, scanning electron microscopy, and ^{1}H NMR spectroscopy of samples digested in NaOH characterizing the collapse of the MOF structure and deactivation of the catalyst. The deactivation was caused by alcohol reacting to form node alkoxy ligand and to break node–linker bonds, unzipping the MOF and creating amorphous material preferentially near the MOF particle surfaces. The methods implemented in this work are suggested to be of value for assessing the strengths and limitations of MOFs as practical catalysts.

CHAPTER ONE

A Review of Metal-Organic Frameworks and Alcohol Dehydration Reactions Catalyzed by Metal-Oxides, Zeolites, and MOFs

1. A GENERAL OVERVIEW OF METAL ORGANIC FRAMEWORKS

Metal organic frameworks (MOFs) are a novel class of solid materials, comprising inorganic metal nodes and multidentate organic ligands.[1] Inorganic nodes can range from single metal atoms to few-atom metal oxide polyhedra (clusters) that are bonded to organic groups (including linkers and possibly other groups) through nucleophilic functional groups. During synthesis, multidentate organic ligands bridge two or more inorganic nodes that have formed in the synthesis solution, creating a crystalline superstructure of alternating inorganic and organic pieces. High acidity of the aqueous synthesis solution and modulators can lower the nucleation rate, sometimes giving more highly crystalline MOF.[2] The versatility of this reticular synthesis, which allows for combinations of various organic linkers, metal salts, and solvothermal reaction conditions, has resulted in a vast and accelerating library of MOF structures.[3]

Many MOFs in this library contain variations beyond the resolution of microscopic characterization techniques. These variations are not all well understood because knowledge of MOF defect chemistry is still in its infancy.

Properties and Applications. MOFs have pore volumes and surface areas that are significantly larger than those of any other group of hybrid organic/inorganic solids. These properties have encouraged investigations of MOFs for potential gas adsorption and catalysis applications and have also led to investigations of MOFs as supports for structures such as encapsulated metal nanoparticles, formed inside the MOF pores via ship-in-a-bottle syntheses.[4–6] The chemical flexibility of the organic linkers provides opportunities to control MOF compositions and structures. The syntheses may involve incorporating functionalized organic linker precursors into the synthesis mixture or post-synthetic modification of the MOF.[7] Thus, there are many opportunities to engineer unique environments in MOF pores for catalysis.

However, the intrinsic mechanical, thermal, and oxidative instability of MOFs and their organic linkers, and challenges in synthesis scale-up, limit current commercial employment of MOFs, and there are no large-scale applications of MOFs as catalysts.[8] Thus, MOFs are not yet likely to compete in practical catalytic applications with inexpensive, commercially available materials such as metal oxides and zeolites. However, MOFs may be ideal for specialized catalytic applications, such as those giving regiospecific catalytic selectivity.

Characterization of the bulk structures of MOFs is well developed, with the principal techniques being x-ray diffraction (XRD) crystallography and determination of surface area/pore volume data by analysis of adsorption isotherms, analyzed with Brunauer-Emmett-Teller (BET) theory.[9] However, the results of these experimental techniques can be imprecise, yielding large calculated differences in measured surface properties, because of inconsistencies in syntheses giving materials with various nanoscale structural properties including defects—many of which are beyond the resolution of adsorption isotherms and undetectable by x-ray diffraction crystallography. These inconsistencies influence the porosity, stability, and acidic properties of MOFs, among others.[10] Simple reactions catalyzed by the MOFs offer opportunities to probe the MOF defect sites.

Catalytic dehydration reactions of small, simple alcohols provide opportunities to explore reactivity of acidic and basic sites on MOF nodes, to distinguish between Lewis and Brønsted acid sites, and to determine reaction mechanisms that are sensitive to the positioning of active sites.[11]

Recently, Yang et al. used ethanol dehydration as a probe reaction to explore some of the nano-scale properties of MOFs in the UiO family (details below).[12] In this study, initial conversion differed between structures synthesized with acetic acid and hydrochloric acid as modulators and between structures with the same modulator but varied methoxy, formate, and hydroxy capping groups that formed on the MOF nodes, which were Zr_6O_8 clusters. Density functional theory (DFT) models showed the importance of neighboring defect sites in the bimolecular step required for dehydration of ethanol to form diethyl ether.

MOFs with Zirconium-Containing Nodes. A series of metal-organic frameworks has been synthesized from zirconium salts and multidentate aromatic organic complexes with carboxylate functional groups derived from carboxylic acid precursors. The octahedral inorganic node-linker combination, approximated as $Zr_6O_4(OH)_4(R\text{-}CO_2)_{12}$, consists of six zirconium atoms in square antiprismatic coordination with oxygen, four from the organic linkers and the other from alternating μ_3-O/μ_3-OH atoms centered on the eight triangular faces of the inorganic octahedron. Coordination with the organic linkers 1,4-benzene-dicarboxylate, biphenyl-dicarboxylate, terphenyl dicarboxylate, and 1,3,6,8-tetrakis(*p*-benzoic-acid)pyrene (H_4TBAPy) results in isoreticular synthesis of the MOFs UiO-66, UiO-67, UiO-68, and Nu-1000, respectively.[13,14] Furukawa et al. synthesized MOF-808 from zirconyl chloride octahydrate and 1,3,5-benzenetricarboxylic acid (H_3BTC).[15] MOF-808 has a $Zr_6O_4(OH)_4$ node similar to that of UiO-66, but each node has only a coordination of six to the organic linkers. The lower coordination opens the pores of MOF-808 significantly compared to those of UiO-66, with diameters of 18.4 Å and 8.7 Å, respectively, and allows for intraparticle transport of larger molecules in MOF-808.[15,16] Because of its smaller pore size, MOF UiO-66 will be characterized by transport limitations in alcohol dehydration reactions as larger alcohols like isopropanol and 2-butanol, with largest molecular dimensions of 4.3 Å and 5.6 Å, respectively, will be kinetically limited by single-file diffusion. Transport limitations will increase as the alcohol dehydrates to give sterically larger ethers in the MOF pores.

These MOFs are characterized by remarkable thermal, structural, and oxidative stability associated with the low steric strain and strong bonding energy of the Zr-O bonds that link the inorganic node to the carboxylate groups of the linkers.[9] Stability of these MOFs makes them promising candidates as catalysts. Examples of reactions catalyzed by these MOFs include hydrolysis reactions of simulants of the nerve toxin Sarin, and attempts have been made to develop gas masks that incorporate these catalysts.[17] Despite the high stability of these MOFs, as the organic linker increases in size, there is a reduction in thermal and chemical stability with the MOF becoming more susceptible to degradation by water and other nucleophilic molecules.[18] Water and simple alcohols will nucleophilically attack zirconium atoms of the MOF node, breaking node linker bonds, and will also cleave C-C bonds of the organic linker. As a result of its more open pore structure, MOF-808 degrades more rapidly than UiO-66 in alcohol dehydration reactions because diffusion of water and other nucleophilic species will not be as limited by mass transport.

Because of possible influences of transport processes on rates of catalytic reactions in these MOFs, caution is necessary in interpretation of observed reaction rates, because the rates of alcohol dehydration may be obfuscated by the transport limitations. They may also be influenced by competition with small capping molecules such as water (a product of alcohol dehydration) on active sites and by the MOF's denaturing into zirconium oxide by breaking of node-linker bonds leading to the formation of zirconium oxide. Characterization of the initial species present on the MOF active sites, transport resistance into the MOF pores, and the denaturing of the MOF will therefore be critical to accurate analysis of catalytic reaction kinetics.

Routine characterizations of the structures of these MOFs have involved x-ray diffraction and measurement of adsorption isotherms, and the data provide characterizations of the structures that do not account for variations at the atomic scale, such as structural defects where nodes or organic linkers are absent from their ideal crystallographic positions, conjoined inorganic nodes, and the chemical species capping structural defects on nodes.[19] The nature of species capping structural defects in MOFs can vary depending on the synthesis conditions, including the effects of acids and other modulators, washing procedures, and calcination steps. For example, formate caps on UiO-66 nodes, formed from synthesis matrix N,N-dimethylformamide, have been substituted with other carboxylate species and hydroxyl groups through washing and treatment.[20] Capping species influence the activity of the Lewis-acid inorganic sites in catalysis, for example, by occupying the sites and excluding reactants. [12,21] Characterizations of MOFs have begun to include analysis of the organic components on the nodes by ^{1}H NMR spectroscopy of the samples digested in solutions of D_2O and NaOH (or, better, NaOD)—to quantify and identify the organic linkers, the node-capping groups, and, consequently, the average number of missing linkers per node.[22] However, this technique can be limited by not identifying changes in crystalline phase which could result in a higher missing linker value than expected. [19]

MOFs with Zirconium containing Nodes in Alcohol Dehydration Reactions. The $Zr_6O_4(OH)_4(R\text{-}CO_2)_{12}$ node has demonstrated catalytic activity for alcohol dehydration reactions. This node contains both Lewis acid sites in the form of accessible electrophilic zirconium atoms and Brønsted acidic groups, including from the four μ_3-OH groups. The tunable porosity and high density of active sites offer catalytic environments different from those of traditional acid catalysts, zeolites and metal-oxides.

The accessibility and density of the Lewis acid sites will depend on the number of defects in the MOF structure. As the number of defects increases, more zirconium atoms become accessible to reactant alcohols upon removal of capping species. The desorption energies of capping species and number of available zirconium atoms will influence alcohol adsorption, with energetic variations becoming larger as node symmetry is destroyed. This property is also observed in bulk metal oxides, whereby the exposed crystallographic surface plane and geometric facets produce surface sites of various adsorption energies. Another consideration relevant to catalysis is that the organic linkers may be (slowly) replaced by water and alcohol as node-linker bonds are broken. This complication further changes the nature of the zirconium atoms, possibly as the MOF nodes will merge and the catalyst surface area will decrease.

The μ_3-OH groups may also play a role in alcohol dehydration catalysis. Although metal-oxide Brønsted acids are often too weak to catalyze alcohol dehydration, they may be active in MOFs. The MOF nodes will have electronic properties different from those of bulk metal-oxides because of their different electron-withdrawing/electron-donating properties and their inherent instability as small clusters. Thus, catalysis by MOFs will differ from catalysis by metal oxides and zeolites because the structures are different, the pathways for Lewis and Brønsted acid-catalyzed reactions are different, and because their susceptibilities to inhibition by water are different.

Adjacent positioning of the defect sites plays a significant role in catalysis involving the reactions of neighboring node-anchored groups in catalysis, such as in the diethyl ether formation in ethanol dehydration, and it may help to explain why MOFs have displayed higher selectivity for ether formation than traditional catalysts such as γ-Al_2O_3. Unlike metal-oxides and zeolites, described in more detail in the following sections, MOFs offer different catalytic environments with high densities of pockets of active sites confined in pores, with some in locations that include sites where linkers are missing. The small MOF pores, which are not typical of metal oxides, are not dissimilar to those of zeolites but are different in the secondary forces they may exert on reaction intermediates. Indeed, recent investigations into zeolites as catalysts have demonstrated that the sterics and secondary forces present in the pores markedly influence catalytic behavior.[23,24] Exploration of these nano-scale structural properties provides opportunities to begin to explain characterization discrepancies between macroscopically identical MOFs and to further the ability to tailor these structures for highly selective reactions.[8]

2. A GENERAL OVERVIEW OF ALCOHOL DEHYDRATION REACTIONS

Heterogenous catalytic dehydrations of alcohols are excellent probe reactions for characterization of catalytically active sites on many solids, including metal oxides, molecular sieves such as zeolites, and, more recently, MOFs.[11,12] The reaction mechanisms will be described in more detail in following sections. Here are some details of key characteristics of the reactions, justifying their usefulness in the study of MOFs:

1. Ether formation stoichiometrically requires two adjacent species from reactant alcohol in a steric conformation that facilitates a nucleophilic substitution reaction. Thus, the selectivity of the reaction between olefin and ether will provide insight about the location and distance between active sites. Additionally, as the size and branching of the reactant alcohol is increased, the steric and electronic properties of ether selectivity will change. MOFs contain a high density of active sites on the node that are not well understood, and the reactions of alcohols offer the opportunity to further investigate and understand them.
2. Alcohol dehydration can be catalyzed by Lewis and/or Brønsted acid sites, both requiring an adjacent basic site. The activity of the catalyst will depend on the type of acid site that more rapidly dehydrates the alcohol. Activities of Lewis and Brønsted acid sites differ in the extent and mechanism of inhibition by water. These differences can be observed by varying the partial pressure of water in the reactant feed to a reactor containing an alcohol dehydration catalyst. For MOFs, which contain both kinds of acidic sites, the reactions offer opportunities to distinguish between these sites and the conditions under which they activate alcohols.

3. Larger alcohols when dehydrated form multiple isomers of olefins, such as *cis*- and *trans-2*-butene from 2-butanol. The selectivity for formation of the different isomers may be controlled by steric constraints imposed by the MOF pores and structure, but one has to recognize that secondary reactions, olefin isomerizations, may play a role. These isomerizations are of interest in their own right for probing MOF catalytic sites. MOF pores can be enlarged without changing the composition of the nodes by exchanging the organic linker for longer analogous organic carboxylates, thereby changing the steric constraints imposed on the transition states and possibly stabilizing certain states over others.
4. Transport limitations in MOF pores need to be addressed. The issues are complicated because changes in the MOF particle size cannot generally be isolated from changes in the nanoscale properties of the MOF framework, because MOF synthesis is generally so complex that the microstructures (including defects) of small MOF particles made in a given synthesis may be different from those of larger particles made in that synthesis. Furthermore, the node and organic linker will be slowly changed by reaction with the reactant alcohol through nucleophilic substitution, displacing the organic linker. The rate at which the structures of these MOFs are changed by reactions with alcohols may be related to the transport limitations imposed on the alcohol.

To summarize, in MOF science there is much yet to be learned about the details of the active sites and the nature of the bonding of small molecules adsorbed on them. These nanoscale features cannot be observed in traditional MOF characterization analysis methods. Furthermore, the variations in these sites are responsible for inconsistencies in microscopic characterization, resulting in difficulties replicating surface area measurements with high precision, especially in

MOFs that have higher defect densities.[19] The alcohol dehydration reaction mechanisms involve direct interaction with the Lewis and/or Brønsted acid sites, which adsorb reactant alcohols for catalysis. The adsorption processes will be controlled by the surface species on the MOF nodes and influenced by the number and type of adjacent defect sites. Furthermore, MOFs provide a uniquely tunable porous microstructure, analogous to those of zeolites.

In 2020, reports of investigations by Hoffman et al. of zeolites demonstrated that the proximity and arrangement of active sites within the zeolite pores influence the activation energy for alcohol dehydration.[24] In related study, reported in 2020, by the group of Grounder, ethanol dehydration and kinetics studies with water inhibition were used to examine the H-bonded networks of solvated water clusters in zeolite pores.[25] Both studies demonstrate opportunities for tailoring frameworks of active sites and sterics to match geometries of reactants and transition states to manipulate reaction selectivity in alcohol dehydration. This point illustrates an advantage that MOFs have over other catalysts, and thus highlights the relevance of MOF characterization with catalytic alcohol dehydration. Details of reaction mechanisms and key investigations will be covered in following sections.

History and Industrial Importance. Explorations of alcohol dehydration reaction mechanisms on solid catalysts have been mostly performed with activated alumina[26] and molecular sieves[27,28]. Activated transition aluminas, especially γ-Al_2O_3, are an industrially important catalysts because of their high activity for acid-catalyzed dehydration, isomerization, alkylation, and other reactions.[29] Because of alumina's importance to industry, the catalytic nature of alumina has a long history of investigations through probing with alcohol dehydration catalysis, dating back to the 1950s.[11] Since then dehydration of ethanol catalyzed by alumina has continued to receive significant attention due to importance of ethylene in the petrochemical industry, the advantages of the low temperature catalysis on aluminum oxide, and the relative simplicity in mechanistic studies for elucidating the behavior of solid catalysts.

Generalized Reaction Scheme. The primary products of alcohol dehydration reactions are olefin, ether, and water. Even when limited to selectivity of ether and olefin, the alcohol dehydration mechanism are sometimes complicated by the similar energetic stability of the intermediates of both competing pathways to make ether and olefin and the possible elimination reaction of the ether to olefin at elevated temperatures.[30] Ether/olefin selectivity and reaction mechanisms are dependent on the size and structure of the alcohol, reaction temperature, and many features of the catalyst structure, which may include size exclusion by microporous catalysts, polar and nonpolar interactions within microporous walls, and the proximity and interactions between neighboring acidic sites which will be discussed in more detail in following sections. This complexity has led to several candidate reaction schemes for the ethanol dehydration reaction, generalized below (Scheme 1.1).

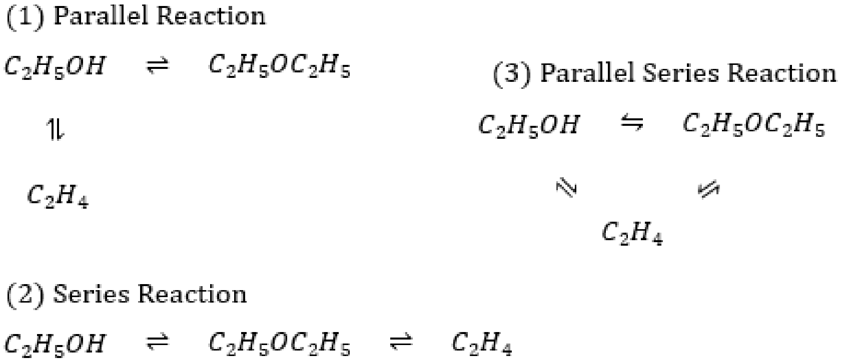

Scheme 1.1: Candidate reaction pathways for the dehydration of ethanol to ethylene. This reaction scheme can be adapted for larger alcohols that can produce ether.

Generalized Mechanism. The mechanism for heterogeneously catalyzed alcohol dehydration by metal oxides and zeolites generally includes:

1. Adsorption of reactant(s)
2. Chemical transformations on the catalyst surface
3. Desorption of the products

The surfaces of catalytically active metal oxides contain incompletely coordinated metal atoms that are stabilized by chemisorption of capping species, such as the reactant alcohol. Adsorbed alcohols can form as molecularly adsorbed alcohols, cyclic alcohol dimers, or surface alkoxides which form following the scission of the O-H alcohol bond. In all cases, the alcohol proton is stabilized by an adjacent basic site, commonly a surface oxygen atom or OH group. Alcohols that form surface alkoxides on alumina give ether as the dehydration product at low temperatures and olefin at higher temperatures.[31] In zeolites, Brønsted acids balance charge compensation of lattice defects and enable solvation of hydrogen-bonded complexes that stabilize the reactant alcohol.

For both of these classes of catalysts, olefin formation requires only a single adsorbed reactant molecule to become dehydrated. However, ether formation requires two adjacent surface species derived from alcohols. The adsorbed state of the additional alcohol is not typically fully understood. In zeolites, the additional alcohol may be captured by the solvated hydrogen-bonded complex, and the size of the complex may limit the reaction rate by imposing a transport restriction in the narrow pores. On metal oxide surfaces, the additional alcohol may find an adjacent Lewis acid site and be adsorbed as molecularly adsorbed alcohol or as an alkoxide, but in some investigations the possibility of physisorbed alcohol is also included. Following formation of the ether, the product is susceptible to re-adsorption and may provide a secondary route to olefin formation. MOFs, which share the Lewis and Brønsted acid characteristics that are common to bulk metal oxides and zeolites, and provide prospects of highly tailored and tunable adsorption sites that might provide unique opportunities for manipulating the selectivity of the alcohol dehydration reaction.

Discussed below, the chemical transformations that take place on the catalyst surfaces can often be generalized to be either E1 or E2 mechanisms for olefin formation and S_N2 mechanisms for ether formation. Although the mechanistic routes vary depending on many parameters, including the catalyst identity, the investigation by Knözinger of alcohol dehydration on alumina provides a brief description of each pathway which is often used as a starting point for computational chemistry of likely intermediates when exploring possible mechanisms on other alcohol dehydration catalysts that incorporate Lewis acid sites.[26]

Knözinger's proposed mechanism of olefin formation on alumina (based on measurements of reaction kinetics and spectroscopy) begins with the adsorbed cyclic alcohol dimer complex described above and is based on the principle of least structural change. In an E1-type mechanism, the strong polarization of the two hydrogen bonds of the adsorbed complex push the reactant oxygen to an oxonium ionic state. The charge migrates to form the more stable carbonium ion which forms the olefin following proton transfer of the alcohols' β-H to an adjacent catalyst surface oxygen atom. The resulting olefin is no longer adsorbed to the surface as the charge migration from oxonium to carbonium state results in the cleavage of the C-O bond.

In the proposed E2-type mechanism, simultaneous cleavage of the $C\text{-}H_\beta$ and C-O bonds leads to the formation of the olefin. As evidence of the E2-mechanism dominating over the E1-mechanism for the dehydration of *tert*-butyl alcohol on alumina, Knözinger demonstrated a primary isotope effect with $(CD_3)_3COD$ and no isotopic effect with $(CH_3)_3COD$, identifying the limiting step as the cleavage of the C-H bond and not the desorption of water. Therefore, an E2 type mechanism was inferred for the dehydration of *tert*-butyl alcohol. Measuring this kinetic isotopic effect was an important step in the analysis of the reaction mechanism because competition between the two pathways will vary with the size/branching of the alcohol, temperature, and the catalyst identity, which all influence the stability of the E1-ionic transition state.

Recent works include computational analysis, a powerful tool in mechanistic studies because it allows for comparison of experimental results to theoretical models. This recent work has propelled the understanding of the mechanism forward by allowing for supporting evidence of the most stable reaction intermediates and transition states. DFT analysis of the olefin formation on γ-Al_2O_3 for ethanol and isopropanol has been performed with the results pointing to the E2 mechanism being favored in all cases.[30,32]

One postulated mechanism for ether formation begins with a surface alkoxide, identifiable on surfaces under flow for all alcohols capable of producing ether. The presence of surface alkoxide allows for another analytical check for ether formation on MOFs, whereby the presence of the surface alkoxide should be spectroscopically observable. Although there is no direct evidence that surface ethoxides are the intermediates for diethyl ether formation, recent DFT analysis demonstrating their higher energetic stability compared to other forms of adsorbed alcohol and their requirement as intermediates on the catalyst surface under conditions that produce ether strongly suggest that they are involved.[30,33] In his 1968 paper, Knözinger eliminated desorption of water as the rate determining step in ether formation by observing no primary isotope effect with deuterated methanol. Therefore, it was concluded that the reaction must either involve the cleavage of the RO-Al of the alkoxide and the R-OH bond of a molecularly adsorbed alcohol, or alternatively the cleavage of the R-OAl bond of the alkoxide and the RO-H bond of the adsorbed alcohol, with the competition between the two mechanisms depending on the sterics of the catalyst surface. These pathways support the conclusion of an S_N2 type mechanism and that is supported by a recent DFT analysis.[30]

In addition to olefins and ether, water also forms as a product of the reaction, with a stoichiometry of 1:1 with olefin and 1:2 with ether formation. Compared to adsorbed ether and olefin on the catalyst surface, water has a significantly higher enthalpy of adsorption and is almost irreversibly formed from dehydrating reactants, making it difficult to remove from the surface. This water will therefore inhibit both Lewis and Brønsted acid catalysts by competing with reaction intermediates. In Lewis acids, the water remains chemisorbed to surface metal atoms and stabilizes the metal-oxide surface energy, making it difficult to remove under reaction conditions. The proton of the adsorbed water becomes activated as a weak Brønsted acid but has not been shown to have demonstrated catalytic activity for subsequent alcohol dehydration reactions. Thus, in Lewis acid catalyzed alcohol dehydration reactions on metal oxides, water monomer and dimers directly occupy active sites and inhibit catalysis.

On Brønsted acids, such as zeolites, the reaction takes place through hydrogen-bond stabilized complexes. The water, formed in the reaction, will remain in the pores and add to the total volume of the hydrogen-bonded solvated complex. As the dimensions of the complex increase, the protonating ability of the proton donor will decrease and selectivity to the ether will drop as adjacent solvated alcohols will be farther apart. This pattern makes the inhibition by water different from that in Lewis acid catalysts, as in this case water reduces the activity of a Brønsted acid site but does not directly block the site. In zeolites the size of the solvated Brønsted networks are limited by confinement of the zeolite pores. This effect on the catalyst pores can further control the displacement of the proton and the access of alcohols in bimolecular catalysis. The effects of water accumulation will be interesting to examine in MOFs because they, like acidic zeolites, will display confinement properties in their pores and may also have active Brønsted acid sites. Investigations of these effects in MOFs are lacking.

3. METHODS OF INVESTIGATING REACTION MECHANISMS AND RESEARCH OPPORTUNITIES.

Comparisons between catalytic materials can be challenging to investigate because reactions depend significantly on many parameters. Alcohol dehydration is among the simplest classes of reactions because of the limited selectivity between ether and olefin conformers, with the product pathways being different, making this class of reactions ideal for initial kinetics studies of acid catalysts. The kinetics of reactions, including the dependence of reaction rate on temperature and the contact time of the reactants with the catalyst, will be reflected in the observed conversions and selectivities. Topology of the catalyst surfaces and the nature of the acidic sites will affect the available pathways of the reaction, and even small differences that control the distance between acid sites will influence the overall rate and selectivity. The micro-porosity of many of the MOFs referred to here can complicate mechanistic examinations through transport limitations, but the pore geometries may also be used to tune the selectivity through regioselectivity and secondary forces of the pores. To help in understanding the nuances specific to each case of alcohol dehydration, there are several tools available. These include kinetic isotopic effects, kinetics studies with reactor systems designed to determine reaction rates directly (although not necessarily in the absence of transport effects), infrared spectroscopy, adsorption isotherms, and analysis with computational chemistry tools.

Historical Perspective on Advances in Characterization of Alcohol Dehydration Reactions Catalyzed by Solid Acids. Studies of alcohol dehydration on various solid catalysts are provided below. Studies beginning in the mid-20th century, were primarily concerned with identifying alcohol dehydration reaction networks and mechanisms, adsorbed complexes, types of active sites, and reaction intermediates. Characterization tools for these investigations included flow reactor experiments with infrared spectroscopy, gas adsorption/desorption isotherms, and nuclear magnetic resonance (NMR) spectroscopy. These investigations were able to answer these questions for specific combinations of reactant alcohols, catalysts, and reaction parameters. However, these investigations were unable to explain more nuanced details of the reaction mechanisms, for example, distinguishing between different Lewis acid sites on the catalyst surface or describing stabilizing influences of catalyst surfaces and pores on reaction intermediates. Recent advances in computational chemistry have allowed complementary studies of these details, through development of energetic models of the alcohol dehydration reaction mechanisms and complementary kinetics.

Adsorbed Reactant Complexes Identified on the Surface of Alumina. The nature of the adsorbed reactant alcohol (or species derived from it) serves as a starting point for most computational chemistry investigations and provides potentially important information about the reaction mechanism. For example, alcohols that form surface alkoxides on alumina give ether at low temperatures of dehydration and olefin at higher temperatures.[31] Higher-order n-homologs and more highly branched alcohols that do not form surface alkoxides and tend toward olefin formation. Early investigations of alcohol adsorption were performed by Greenler, who characterized methanol and ethanol adsorption on alumina with infrared spectroscopy and matched the vibrational modes of the adsorbates to those of analogous metal alkoxides and carboxylates.[34] The author also investigated isotopic shifts using C^{13} substitution, CD_3OH, and CH_3OD to provide further evidence of the predicted alkoxide and carboxylate structures that formed under methanol flow. In the adsorption of these alcohols, Greenler observed an easily removed coating of physisorbed alcohol as well as alkoxides and formates that were expected to form in IR experiments.

As further evidence of alcohol adsorption, NMR studies showed a direct interaction of the alcohol hydroxyl group and the alumina surface.[35] The NMR results show adsorbed alcohols formed hydrogen bonded complexes with the alumina surface. However, the NMR results are inconclusive about the geometry of the hydrogen bond angles. Infrared spectra of adsorbed ethanol reported by Knözinger et al. show an absorption profile that more closely matches that of cyclic alcohol dimers with a central absorption band at 3500 cm^{-1}.[36,37] IR spectra of the adsorption of methanol, *tert*-butyl alcohol, isobutanol, phenol, and benzyl alcohol was reported to have similar hydroxyl absorption profiles. Although individual linear hydrogen bonds are stronger than the individual angular bonds of dimer complexes, linearly bound alcohols cannot form multiple bonds with alumina surfaces and therefore have a lower total energy of formation than dimers which form multiple bonds with the surface. Additionally, sterics favor the doubly angularly bound alcohols because branches of larger alcohols (i.e. *tert*-butyl alcohol) are kept perpendicular to the surface in this conformation. Both IR and NMR spectra identify surface alkoxides, and their presence coincides with the formation of ether in the catalytic dehydration of the alcohol. However, no direct evidence has solidified alkoxides as reaction intermediates, they could be spectators. In recent DFT studies, care has been taken to examine the possibility of either molecularly adsorbed alkoxides and/or alcohol (as solitary and dimeric surface species) as starting adsorbed complexes. In these investigations, adsorbed alkoxide is universally found to be more stable than the others.[38]

Kinetics and Selectivity Experimentation for Alcohol Dehydration on Alumina. In early studies to determine the reaction scheme of ethanol dehydration on γ-Al_2O_3, Knözinger investigated the product distribution as a function of temperature (211 to 343 °C) and contact time of alcohol with the catalyst.[31] At temperatures below 240 °C, diethyl ether was the only product formed. As temperature increased from 240 °C, ethylene formation began. Formation of the olefin was characterized by a slight induction period, indicative of a consecutive reaction and the formation of olefin as a secondary product, that decreased and disappeared at 298 °C. Ether formation decreased with increasing temperatures and was eliminated entirely at 343 °C. These kinetic studies provided evidence that at low temperatures, the reaction was dominated by bimolecular ether formation. Whereas at higher temperatures, the reaction began to form olefin through primary elimination of the reactant alcohol and through a secondary mechanism by which the ether was reabsorbed and underwent elimination to olefin.

Similar kinetics investigations were also performed with larger and more highly branched alcohols, which favored the formation of the olefin over the ether.[31] For smaller alcohols, ether selectivity dominated at lower temperatures. However, alcohols larger than 2-butanol exhibited no selectivity for ether formation. Knözinger related these trends to variations in the energy barriers of the reaction for different alcohols, whereby the ether formation pathway was found to be strongly disfavored thermodynamically for the larger alcohols.

First steps in the analysis of MOFs for the alcohol dehydration reaction will ideally follow similar kinetic investigations. Recent work by Yang et al., regarding dehydration of ethanol on zirconium containing MOFs, demonstrates catalytic differences compared to γ-Al_2O_3 with MOF selectivity exclusively for diethyl ether.[39] In this work, no ethylene formation was detected in the range of 200 to 250 °C and DFT suggests that the key to this selectivity arises from the adjacent locations of active sites on the MOF node surface. With the ethanol dehydration selectivity exclusive for formation of diethyl ether, this opens questions for the branched and longer carbon chained alcohols. MOFs, which have promise as highly selective catalysts, may be capable of ether selectivity not observed on γ-Al_2O_3 or zeolites. Changes to the adsorbate stability and steric requirements of ether formation occur as the reactant alcohol varies in size. Olefin/ether selectivity of MOFs with methanol and larger alcohols has not been investigated and provides opportunities to continue to investigate the cooperative and unique nature of the MOF active sites.

Influence of Catalyst Surface on Alumina. Catalysis of a surface is strongly dependent on its structure, adsorbates, and electronic properties. The surface of alumina was investigated by Peri with infrared and gravimetric studies, which identified hydroxyl groups and oxide ions that formed from the dehydration of the (100) alumina surface.[40] He concluded that non-uniform lattice strain distribution created localized strain fields that held tightly to hydroxyls, preventing complete dehydration of the surface even under high temperature evacuation.[41] This process leaves the surface with both weak Brønsted acids, in the form of irreversibly adsorbed hydroxyls, and Lewis acids, from the condensation of two hydroxyls leaving incompletely coordinated aluminum ions. Recent high resolution electron microscopy of platelet shaped γ-Al_2O_3 nanoparticles identified both higher energy (110) and (111) surfaces, with (100) and (111) facets in the pores.[42] Closer examination of the (110) surface revealed that it was made up of nanoscale (111) facets which includes penta, tetra, and tri-coordinated aluminum atoms. This microscopy study expanded the complexity of the ethanol dehydration reaction which had been previously limited to penta-coordinated aluminum Lewis acid sites on the (100) surface. DFT found comparable energetic barriers for ethanol dehydration over the (100) and (111) surfaces.[30,43] This leaves exact nature of the aluminum active sites in γ-Al_2O_3 complicated by the surface topology and by the influence of nano-scale facets and geometries. [26,30] Slight variations in the electrophilic state of the aluminum atoms, their position relative to each other, and adsorption of small molecules (water) on neighboring sites are important components of understanding the mechanism of alcohol dehydration. These features are particularly relevant in this reaction because of the bimolecular nature of the ether formation, where DFT demonstrates that the positioning of adjacent Lewis acidic zirconium atoms play a role the exclusive selectivity of diethyl ether in MOFs.[39] It would be interesting to compare the DFT and reactor analysis of ether formation on zirconium-based MOFs with their hafnium-analogues to determine the importance of sterics in the reaction energetics.

Transport Limitations in MOFs. Zeolites and MOFs are highly porous structures with microporous environments that can control the catalytic selectivity through regiospecific constraints but may also impose intraparticle mass transport barriers. These transport barriers can disguise true kinetics of reactions and must be considered for porous catalysts. The standard test for mass transport limitations is to vary the particle size of the catalyst and corresponding changes in the reaction rate.[44] Recently, Wang et al. synthesized Pt@UiO-66 with MOF particle diameters of 30, 125, and 380 nm for the synthesis of imines from nitrobenzene, demonstrating a decrease in rate as the particle size increased.[45] In purely inorganic catalysts, the particle size can be modified in synthesis with no changes to the catalytic structures. However, in MOFs, changes to the particle size through synthesis, or those done mechanically, cannot be done without modification of the catalytic structure. The weaker organic-inorganic links are susceptible to chemical or mechanical changes which will change the amount and activity of acidic zirconium atoms when those links break. Therefore, the best solution to avoiding transport limitation is to ensure that the pore windows of the MOF are sufficiently larger, such that the rate is not limited by the diffusion of the reactants and products. Recent work by Yang et al. with catalytic alcohol dehydration of tert-butyl alcohol and ethanol on MOF-808 and UiO-66 demonstrate that the framework slowly collapses as the nucleophilic reactants and products compete with organic linkers of the MOFs.[12,46] Instances where the MOF could not easily accommodate the size of the reactant alcohol resulted in a lower initial rate and a slower degradation of the framework. It is possible that for reactions where diffusion into the pores is fully limited by size exclusion, that the reaction will only take place on the particle surface. This could offer an opportunity to both slow the collapse of the framework and to account for the diffusion limitations of the MOF with precise characterization of the MOF surface area following exposure to alcohol flow.

Regioselectivity in Zeolites. In 2011, Kwak et al. studied the dehydration of 2-butanol on alumina and H-form zeolites.[23] Variations in the olefin product for *cis* and *trans*-2-butene was investigated with catalytic reactor experiments and reinforced with computational analysis. By accounting for van der Waals interactions in the computational analysis, the authors were able to demonstrate a stabilization of the *trans*-2-butene transition state when the hydrocarbon component of the alcohol was able to interact with the secondary forces of the support. In experimental work, the *trans/cis*-2-butene ratio varied between < 1.0 and 8.5 in H-form zeolites, with small pore H-FER having the large 8.5 *trans:cis* ratio by matching the van der Waals dimensions of the butoxide species. Similar regioselective environments may be possible in MOF structures, by controlling both the length of the carbon backbone of the organic linker and the number of missing linkers in the MOF lattice.

Influence of Confining Environments. Zeolites contain Bronsted acidic hydroxyls that are associated with framework Al^{3+} and open Al^{3+} Lewis acid sites. These sites can also be modified to include Lewis acidic metals by substitution of framework Al^{3+} with Sn^{4+} and Ti^{4+}. Density of these acid sites can control the polarity of the zeolite structure, by including more polar acidic sites in the otherwise hydrophobic framework. Furthermore, synthetic conditions and structure directing agents allow fine control of the microporous structure. As a result, zeolites have been rigorously studied to find ways to control the sizes and polarities of their microporous environments. Alcohol dehydration reactions are among the most import historically for advancing the understanding zeolites as catalysts.

These investigations highlight the forefront of research of acid catalysis by zeolites, where investigations involve complementary kinetic and computational examinations of specific features of the confining environment of the zeolite pores. All these investigations point towards the control and rational development of tailored catalytic environments, encapsulated within the zeolite pores, for highly selective catalysis. It can be expected that work will continue to be published on other ways to change and characterize the zeolite pores. Highly selective catalytic environments that can be finely controlled by chemical and steric modifications to a solid porous catalyst offer opportunities for MOFs. Organic linkers of MOFs offer environmental manipulations not possible in inorganic solids, such as zeolites. However, these nuanced investigations on zeolites were only possible because of the high crystallinity, synthetic control, and deep understanding of the zeolite structure. Conclusions about the differences between confining zeolitic structural environments would not be possible if the crystal structures were not uniform.

Although MOFs have been investigated as alcohol dehydration catalysts, the catalytic detail, summarized above for zeolites, has not been obtained by the MOFs. However, preliminary investigations into the nuances of the confining structure of MOFs has begun to emerge in recent work. In recent work by Yang et al, dehydration of ethanol alcohol by UiO-66 and MOF-808 have shown a high selectivity towards ether formation compared to zeolites.[12] Computational and initial reactor experiments have demonstrated that these solid catalysts are also highly controlled by the nature of the chemistry of their pores, where polarity and defects stabilize transition states that lead to bimolecular formation. However, transport limitations and synthetic inconsistency have slowed advances into the kinetic investigations of these pores, there is good reason to suspect that the interaction between alcohol-water monomers, dimers, and clusters with the confines of the pores will lead to mechanistic insights of the reaction. In the following section, experimental investigative methods to explore this avenue of MOF research will be explained.

4. EXPERIMENTAL PLANS

MOFs comprised of the $Zr_6O_4(OH)_4(R\text{-}CO_2)_n$ (where *n* is the coordination to organic linker) node and various di- and tri-tropic carboxylate organic linkers have been well characterized at the microscopic level. These MOFs form highly crystalline compounds with large surface areas and microporous networks that can be controlled with the size of the organic linker. These MOFs also have remarkable thermal, mechanical, and chemical stability compared to other MOFs, resulting from the uniquely strong linker-node bonding energy of the zirconium atoms and carboxylate functionals. This stability commends these materials as potential catalysts.

Their tunable pores and stability make these MOFs one of the strongest candidates for studies in alcohol dehydration reactions. UiO-66 was selected for experimentation because this MOF can be easily, quickly, and safely synthesized and because it offers structures comprised of the zirconium-oxide octahedral node, with Lewis acidic active sites and a large surface area and pore size.

Investigations of these MOFs with alcohol dehydration reactions will contribute to the understanding of MOFs as solid catalysts and how they contrast to zeolites and metal-oxides. Significant work has already been accomplished on characterizing the capping species present on these MOFs. This has involved characterization of the MOF with ^{1}H NMR spectroscopy of the samples formed by digestion of the MOFs in D_2O/NaOH solutions—to quantify and identify the organic linkers, the node-capping groups, and, consequently, the average number of missing linkers per node.[22] Catalytic ethanol dehydration of MOFs UiO-66 and UiO-67 by treatment with formate, acetate, and hydroxyls was demonstrated to inhibit initial reaction rates before they were replaced by ethoxy groups following exposure to reactant ethanol.[12] Additionally, this work provided a DFT analysis on the possible mechanisms to compliment the observed 100% selectivity for diethyl ether formation from catalytic reactor data. The computational analysis proposed an S_N2 type mechanism that was facilitated by adjacent ethoxy capped surface sites. Recently, MOF-808 and UiO-66 were investigated with the dehydration of *tert*-butyl alcohol.[46] This work demonstrated clear intrapore transport limitations that inhibited the catalytic activity of UiO-66 but not MOF-808. Furthermore, computational analysis was used to propose an E1 type dehydration mechanism of *tert*-butyl alcohol to olefin.

In both studies with ethanol and tert-butyl alcohol there is evidence that the MOFs degrade from exposure to water and the reactant alcohol. The relationship of intrapore transport limitations and the degradation of the MOF structure need to be investigated further. This can be explored with conversion vs. time-on-stream experiments in flow reactors charged with UiO-66 along with alcohols of various sizes ranging from methanol to butanol. Varying the size of the reactants between methanol and isopropanol will provide a better understanding of the intrapore transport and degradation of the MOFs. Furthermore, these reactions have not yet been characterized for UiO-66 catalysis. Here it is expected that the transport will be limited when reactant alcohol matches the diameter of the pores, and consequently, the degradation rate of the MOF will be reduced. This may be related to loss of crystallinity, observable in microscopic characterization of MOFs, and offer insight on how the MOFs fall apart. Furthermore, these experiments also offer opportunities to explore the selectivity of isopropyl alcohol which has not yet been examined.

Information on the impact of the location and density of catalytically active sites will be gained from these experiments. Here it is expected to observe that MOFs continue to offer higher selectivity for ethers than that of metal-oxides because of the high availability of adjacent adsorbed alcohols.

Although, the aforementioned experiments have advanced understandings of the defect sites and possible mechanisms for alcohol dehydration reactions catalyzed by MOFs, it is notable that literature does not contain any reports of reaction kinetics. Experimental kinetic data is important in complementing the computational analysis performed, by both verifying the results and offering new perspectives.

For these MOFs, kinetic experimentation is complicated by both the initial inhibiting species that cap catalytically active sites and by the degradation of the framework, which requires a newly charged reactor for each measurement of the kinetic parameters. It is expected that the alcohol dehydration rate will be split into an initial region that is dominated by the interaction with capping species, an intermediary region where catalysis is driven by the acidic behavior of the MOF node, and a terminal region where the rate drops as the MOF denatures into zirconium-oxide. A breakdown of the rate of conversion into these three separate domains has not been performed for MOF catalysts. This offers a new methodology to examine MOFs, taking advantage of an understanding of the nuances of the MOF catalyst. All three regions offer information on the behavior of the MOF as a catalyst, but the intermediary region offers the kinetic information that will be most useful for computational analysis of the reaction mechanism. A systemic approach to the kinetic analysis should both provide reaction orders, mechanistic insights, and descriptions of the initial behavior. Additionally, these studies will identify the activity of the Lewis and Bronsted acids sites as they are inhibited by water in different ways. Here it is expected that MOFs will demonstrate predominately Lewis acid catalyst behavior, however it is possible that slight Brønsted acid activity will be present.

Studies of these MOFs as catalysts for alcohol dehydration offer opportunities to:

1. Investigate these MOFs as catalysts, under conditions that allow measurement of catalytic performance including kinetics, without rapid decomposition of the MOFs. This makes these catalysts and reactions a good fit with each other.
2. Alcohol dehydration reactions are good probes because they provide information on olefin/ether selectivity and activity and on Lewis/Bronsted acid sites
3. Explore intraparticle mass transport limitations related to MOF structure including pore size and attempt to draw conclusions about transport limitations on reaction rates.
4. Examine the degradation and deactivation of MOFs as catalysts as these phenomena may be related to reactions of the MOF nodes with alcohols and water.

In summary, this list demonstrates the potential value of investigations of alcohol dehydration reactions catalyzed by MOFS; alcohol dehydration appears to be among the most valuable in characterizing the catalytic properties of the acid sites on this family of MOFs.

Caution must be taken during the synthesis of the MOF structures to exactly replicate synthesis parameters between batches. This is because small deviations can result in changes to the defect structure of MOFs. Following synthesis, treatment steps, and catalysis steps, the MOFs will be characterized with Powder X-Ray Diffraction, BET surface area measurements, and SEM imaging. Additionally, ^{1}H NMR spectroscopy will be used to quantify the defects (capping species and organic linkers) of synthesized MOFs. The first set of flow reactor experiments will examine conversion vs. time-on-stream for MOF UiO-66 with methanol. These experiments aim to address the intrapore transport MOF degradation, and structural changes of UiO-66. Following this, a second set of experiments will examine the conversion and selectivity vs. time on stream for isopropanol. These experiments aim to continue to address the transport resistance, MOF degradation, structural changes of UiO-66, and details of the active sites that arise from the selectivity between propylene and diisopropyl ether. Both sets of experiments build upon the preliminary alcohol dehydration studies of MOFs and lead to a better understanding of how these structures function as solid acid catalysts.

REFERENCES

(1) Yaghi, O. M.; O'Keeffe, M.; Ockwig, N. W.; Chae, H. K.; Eddaoudi, M.; Kim, J. Reticular Synthesis and the Design of New Materials. *Nature* **2003**, 423 (6941), 705–714. https://doi.org/10.1038/nature01650.

(2) Shearer, G. C.; Chavan, S.; Bordiga, S.; Svelle, S.; Olsbye, U.; Lillerud, K. P. Defect Engineering: Tuning the Porosity and Composition of the Metal–Organic Framework UiO-66 via Modulated Synthesis. *Chemistry of Materials* **2016**, 28 (11), 3749–3761. https://doi.org/10.1021/acs.chemmater.6b00602.

(3) Furukawa, H.; Cordova, K. E.; O'Keeffe, M.; Yaghi, O. M. The Chemistry and Applications of Metal-Organic Frameworks. *Science* **2013**, 341 (6149), 1230444–1230444. https://doi.org/10.1126/science.1230444.

(4) Mason, J. A.; Veenstra, M.; Long, J. R. Evaluating Metal–Organic Frameworks for Natural Gas Storage. Chem. Sci. **2014**, 5 (1), 32–51. https://doi.org/10.1039/C3SC52633J.

(5) Hermes, S.; Schröter, M.-K.; Schmid, R.; Khodeir, L.; Muhler, M.; Tissler, A.; Fischer, R. W.; Fischer, R. A. Metal@MOF: Loading of Highly Porous Coordination Polymers Host Lattices by Metal Organic Chemical Vapor Deposition. *Angewandte Chemie International Edition* **2005**, 44 (38), 6237–6241. https://doi.org/10.1002/anie.200462515.

(6) Britt, D.; Tranchemontagne, D.; Yaghi, O. M. Metal-Organic Frameworks with High Capacity and Selectivity for Harmful Gases. *Proceedings of the National Academy of Sciences* **2008**, 105 (33), 11623–11627. https://doi.org/10.1073/pnas.0804900105.

(7) Kandiah, M.; Usseglio, S.; Svelle, S.; Olsbye, U.; Lillerud, K. P.; Tilset, M. Post-Synthetic Modification of the Metal–Organic Framework Compound UiO-66. *Journal of Materials Chemistry* **2010**, 20 (44), 9848. https://doi.org/10.1039/c0jm02416c.

(8) Yang, D.; Gates, B. C. Catalysis by Metal Organic Frameworks: Perspective and Suggestions for Future Research. *ACS Catalysis* **2019**, 9 (3), 1779–1798. https://doi.org/10.1021/acscatal.8b04515.

(9) Bai, Y.; Dou, Y.; Xie, L.-H.; Rutledge, W.; Li, J.-R.; Zhou, H.-C. Zr-Based Metal–Organic Frameworks: Design, Synthesis, Structure, and Applications. *Chemical Society Reviews* **2016**, 45 (8), 2327–2367. https://doi.org/10.1039/C5CS00837A.

(10) Taddei, M. When Defects Turn into Virtues: The Curious Case of Zirconium-Based Metal-Organic Frameworks. *Coordination Chemistry Reviews* **2017**, 343, 1–24. https://doi.org/10.1016/j.ccr.2017.04.010.

(11) Zhang, M.; Yu, Y. Dehydration of Ethanol to Ethylene. Industrial & Engineering *Chemistry Research* **2013**, 52 (28), 9505–9514. https://doi.org/10.1021/ie401157c.

(12) Yang, D.; Ortuño, M. A.; Bernales, V.; Cramer, C. J.; Gagliardi, L.; Gates, B. C. Structure and Dynamics of Zr 6 O 8 Metal–Organic Framework Node Surfaces Probed with Ethanol Dehydration as a Catalytic Test Reaction. *Journal of the American Chemical Society* **2018**, 140 (10), 3751–3759. https://doi.org/10.1021/jacs.7b13330.

(13) Cavka, J. H.; Jakobsen, S.; Olsbye, U.; Guillou, N.; Lamberti, C.; Bordiga, S.; Lillerud, K. P. A New Zirconium Inorganic Building Brick Forming Metal Organic Frameworks with Exceptional Stability. *Journal of the American Chemical Society* **2008**, 130 (42), 13850–13851. https://doi.org/10.1021/ja8057953.

(14) Mondloch, J. E.; Bury, W.; Fairen-Jimenez, D.; Kwon, S.; DeMarco, E. J.; Weston, M. H.; Sarjeant, A. A.; Nguyen, S. T.; Stair, P. C.; Snurr, R. Q.; Farha, O. K.; Hupp, J. T. Vapor-Phase Metalation by Atomic Layer Deposition in a Metal–Organic Framework. *Journal of the American Chemical Society* **2013**, 135 (28), 10294–10297. https://doi.org/10.1021/ja4050828.

(15) Furukawa, H.; Gándara, F.; Zhang, Y.-B.; Jiang, J.; Queen, W. L.; Hudson, M. R.; Yaghi, O. M. Water Adsorption in Porous Metal–Organic Frameworks and Related Materials. *Journal of the American Chemical Society* **2014**, 136 (11), 4369–4381. https://doi.org/10.1021/ja500330a.

(16) Katz, M. J.; Brown, Z. J.; Colón, Y. J.; Siu, P. W.; Scheidt, K. A.; Snurr, R. Q.; Hupp, J. T.; Farha, O. K. A Facile Synthesis of UiO-66, UiO-67 and Their Derivatives. *Chemical Communications* **2013**, 49 (82), 9449. https://doi.org/10.1039/c3cc46105j.

(17) Mondloch, J. E.; Katz, M. J.; Isley III, W. C.; Ghosh, P.; Liao, P.; Bury, W.; Wagner, G. W.; Hall, M. G.; DeCoste, J. B.; Peterson, G. W.; Snurr, R. Q.; Cramer, C. J.; Hupp, J. T.; Farha, O. K. Destruction of Chemical Warfare Agents Using Metal–Organic Frameworks. *Nature Materials* **2015**, 14 (5), 512–516. https://doi.org/10.1038/nmat4238.

(18) DeCoste, J. B.; Peterson, G. W.; Jasuja, H.; Glover, T. G.; Huang, Y.; Walton, K. S. Stability and Degradation Mechanisms of Metal–Organic Frameworks Containing the Zr6O4(OH)4 Secondary Building Unit. *Journal of Materials Chemistry A* **2013**, 1 (18), 5642. https://doi.org/10.1039/c3ta10662d.

(19) Cliffe, M. J.; Wan, W.; Zou, X.; Chater, P. A.; Kleppe, A. K.; Tucker, M. G.; Wilhelm, H.; Funnell, N. P.; Coudert, F.-X.; Goodwin, A. L. Correlated Defect Nanoregions in a Metal–Organic Framework. *Nature Communications* **2014**, 5 (1), 4176. https://doi.org/10.1038/ncomms5176.

(20) Deria, P.; Bury, W.; Hupp, J. T.; Farha, O. K. Versatile Functionalization of the NU-1000 Platform by Solvent-Assisted Ligand Incorporation. *Chemical Communications* **2014**, 50 (16), 1965. https://doi.org/10.1039/c3cc48562e.

(21) Wei, R.; Gaggioli, C. A.; Li, G.; Islamoglu, T.; Zhang, Z.; Yu, P.; Farha, O. K.; Cramer, C. J.; Gagliardi, L.; Yang, D.; Gates, B. C. Tuning the Properties of Zr 6 O 8 Nodes in the Metal Organic Framework UiO-66 by Selection of Node-Bound Ligands and Linkers. *Chemistry of Materials* **2019**, 31 (5), 1655–1663. https://doi.org/10.1021/acs.chemmater.8b05037.

(22) Yang, D.; Bernales, V.; Islamoglu, T.; Farha, O. K.; Hupp, J. T.; Cramer, C. J.; Gagliardi, L.; Gates, B. C. Tuning the Surface Chemistry of Metal Organic Framework Nodes: Proton Topology of the Metal-Oxide-Like Zr 6 Nodes of UiO-66 and NU-1000. *Journal of the American Chemical Society* **2016**, 138 (46), 15189–15196. https://doi.org/10.1021/jacs.6b08273.

(23) Kwak, J. H.; Rousseau, R.; Mei, D.; Peden, C. H. F.; Szanyi, J. The Origin of Regioselectivity in 2-Butanol Dehydration on Solid Acid Catalysts. *ChemCatChem* **2011**, 3 (10), 1557–1561. https://doi.org/10.1002/cctc.201100173.

(24) Hoffman, A. J.; Bates, J. S.; Di Iorio, J. R.; Nystrom, S. V.; Nimlos, C. T.; Gounder, R.; Hibbitts, D. Rigid Arrangements of Ionic Charge in Zeolite Frameworks Conferred by Specific Aluminum Distributions Preferentially Stabilize Alkanol Dehydration Transition States. *Angewandte Chemie International Edition* **2020**, anie.202007790. https://doi.org/10.1002/anie.202007790.

(25) Bates, J. S.; Bukowski, B. C.; Greeley, J.; Gounder, R. Structure and Solvation of Confined Water and Water–Ethanol Clusters within Microporous Brønsted Acids and Their Effects on Ethanol Dehydration Catalysis. *Chemical Science* **2020**, 11 (27), 7102–7122. https://doi.org/10.1039/D0SC02589E.

(26) Knözinger, H. Dehydration of Alcohols on Aluminum Oxide. *Angewandte Chemie International Edition in English* **1968**, 7 (10), 791–805. https://doi.org/10.1002/anie.196807911.

(27) Chiang, H.; Bhan, A. Catalytic Consequences of Hydroxyl Group Location on the Rate and Mechanism of Parallel Dehydration Reactions of Ethanol over Acidic Zeolites. *Journal of Catalysis* **2010**, 271 (2), 251–261. https://doi.org/10.1016/j.jcat.2010.01.021.

(28) Costa, E.; Uguina, A.; Aguado, J.; Hernandez, P. J. Ethanol to Gasoline Process: Effect of Variables, Mechanism, and Kinetics. *Industrial & Engineering Chemistry Process Design and Development **1985***, 24 (2), 239–244. https://doi.org/10.1021/i200029a003.

(29) Pines, H.; Haag, W. O. Alumina: Catalyst and Support. I. Alumina, Its Intrinsic Acidity and Catalytic Activity 1. *Journal of the American Chemical Society* **1960**, 82 (10), 2471–2483. https://doi.org/10.1021/ja01495a021.

(30) Christiansen, M. A.; Mpourmpakis, G.; Vlachos, D. G. Density Functional Theory-Computed Mechanisms of Ethylene and Diethyl Ether Formation from Ethanol on γ-Al 2 O 3 (100). *ACS Catalysis* 2013, 3 (9), **1965–1975**. https://doi.org/10.1021/cs4002833.

(31) KNOZINGER, H.; KOHNE, R. The Dehydration of Alcohols over AluminaI. The Reaction Scheme. *Journal of Catalysis* **1966**, 5 (2), 264–270. https://doi.org/10.1016/S0021-9517(66)80007-6.

(32) Larmier, K.; Chizallet, C.; Cadran, N.; Maury, S.; Abboud, J.; Lamic-Humblot, A.-F.; Marceau, E.; Lauron-Pernot, H. Mechanistic Investigation of Isopropanol Conversion on Alumina Catalysts: Location of Active Sites for Alkene/Ether Production. *ACS Catalysis* **2015**, 5 (7), 4423–4437. https://doi.org/10.1021/acscatal.5b00723.

(33) Roy, S.; Mpourmpakis, G.; Hong, D.-Y.; Vlachos, D. G.; Bhan, A.; Gorte, R. J. Mechanistic Study of Alcohol Dehydration on γ-Al 2 O 3. *ACS Catalysis* **2012**, 2 (9), 1846–1853. https://doi.org/10.1021/cs300176d.

(34) Greenler, R. G. Infrared Study of the Adsorption of Methanol and Ethanol on Aluminum Oxide. *The Journal of Chemical Physics* **1962**, 37 (9), 2094–2100. https://doi.org/10.1063/1.1733430.

(35) Geschke, D.; Pfeifer, H. Eine Methode Zur Bestimmung Der Orientierung Adsorbierter Moleküle an Festkörperoberflächen. *Zeitschrift für Physikalische Chemie* **1966**, 232O (1). https://doi.org/10.1515/zpch-1966-23211.

(36) Knözinger, H.; Ress, E.; Bühl, H. Wasserstoffbrücken Bei Der Adsorption von Alkoholen an Al2O3. *Die Naturwissenschaften* **1967**, 54 (19), 516. https://doi.org/10.1007/BF01129372.

(37) Kuhn, L. P. The Hydrogen Bond. I. Intra- and Intermolecular Hydrogen Bonds in Alcohols 1. *Journal of the American Chemical Society* **1952**, 74 (10), 2492–2499. https://doi.org/10.1021/ja01130a013.

(38) Guo, W.; Vlachos, D. G. Effect of Local Metal Microstructure on Adsorption on Bimetallic Surfaces: Atomic Nitrogen on Ni/Pt(111). *The Journal of Chemical Physics* **2013**, 138 (17), 174702. https://doi.org/10.1063/1.4803128.

(39) Yang, D.; Ortuño, M. A.; Bernales, V.; Cramer, C. J.; Gagliardi, L.; Gates, B. C. Structure and Dynamics of Zr 6 O 8 Metal–Organic Framework Node Surfaces Probed with Ethanol Dehydration as a Catalytic Test Reaction. *Journal of the American Chemical Society* **2018**, 140 (10), 3751–3759. https://doi.org/10.1021/jacs.7b13330.

(40) Peri, J. B. Infrared and Gravimetric Study of the Surface Hydration of γ-Alumina. *The Journal of Physical Chemistry* **1965**, 69 (1), 211–219. https://doi.org/10.1021/j100885a032.

(41) Peri, J. B.; Hannan, R. B. SURFACE HYDROXYL GROUPS ON γ-ALUMINA 1. *The Journal of Physical Chemistry* **1960**, 64 (10), 1526–1530. https://doi.org/10.1021/j100839a044.

(42) Kovarik, L.; Genc, A.; Wang, C.; Qiu, A.; Peden, C. H. F.; Szanyi, J.; Kwak, J. H. Tomography and High-Resolution Electron Microscopy Study of Surfaces and Porosity in a Plate-like γ-Al 2 O 3. *The Journal of Physical Chemistry C* **2013**, 117 (1), 179–186. https://doi.org/10.1021/jp306800h.

(43) Christiansen, M. A.; Mpourmpakis, G.; Vlachos, D. G. DFT-Driven Multi-Site Microkinetic Modeling of Ethanol Conversion to Ethylene and Diethyl Ether on γ-Al2O3(1 1 1). *Journal of Catalysis* **2015**, 323, 121–131. https://doi.org/10.1016/j.jcat.2014.12.024.

(44) Mears, D. E. Tests for Transport Limitations in Experimental Catalytic Reactors. *Industrial & Engineering Chemistry Process Design and Development* **1971**, 10 (4), 541–547. https://doi.org/10.1021/i260040a020.

(45) Wang, B.; Liu, W.; Zhang, W.; Liu, J. Nanoparticles@nanoscale Metal-Organic Framework Composites as Highly Efficient Heterogeneous Catalysts for Size- and Shape-Selective Reactions. *Nano Research* **2017**, 10 (11), 3826–3835. https://doi.org/10.1007/s12274-017-1595-2.

(46) Yang, D.; Gaggioli, C. A.; Ray, D.; Babucci, M.; Gagliardi, L.; Gates, B. C. Tuning Catalytic Sites on Zr 6 O 8 Metal–Organic Framework Nodes via Ligand and Defect Chemistry Probed with Tert -Butyl Alcohol Dehydration to Isobutylene. *Journal of the American Chemical Society* **2020**, 142 (17), 8044–8056. https://doi.org/10.1021/jacs.0c03175.

CHAPTER TWO

Life History of the Metal-Organic Framework UiO-66 Catalyzing Methanol Dehydration: Synthesis, Activation, Deactivation, and Demise[11]

ABSTRACT: The life cycle of a metal-organic framework (MOF) catalyst, UiO-66, which incorporates Zr_6O_8 nodes and 1,4-benzene dicarboxylate linkers and is known for its stability, was investigated with methanol dehydration as a test reaction. Catalyst performance was determined with a once-through flow reactor at atmospheric pressure and temperatures of 473–573 K. The products were analyzed by on-line gas chromatography, and catalyst samples removed from the reactor after various times on stream were characterized by X-ray diffraction crystallography, surface area measurements, scanning electron microscopy, and ^{1}H NMR spectroscopy of samples digested in NaOH. The MOF particles underwent marked changes in composition and structure during catalysis, being activated initially as node formate and acetate ligands formed in the syntheses were removed by reaction with methanol to make methyl esters that desorbed and opened catalytic sites. From the beginning, the catalyst underwent deactivation, becoming completely deactivated after times on stream of 10–20 h, depending on the initial MOF composition. The deactivation was caused by methanol reacting to form node methoxy ligands and to break node–linker bonds, unzipping the MOF and creating amorphous material preferentially near the MOF particle surfaces. As the interior particle structure became degraded

---

[1] This chapter has been accepted in *Chemistry of Materials* for publication in **2022** by E. T. Conley and B. C. Gates. The original manuscript has been reformatted to fit the requirements of the dissertation.

and inaccessible, the catalysis shut down. The tactics implemented in this work are suggested to be of value for assessing the strengths and limitations of MOFs as practical catalysts.

INTRODUCTION

The literature of metal-organic frameworks (MOFs)—porous, crystalline materials consisting of inorganic nodes and organic linkers (struts)—has evolved beyond a discovery stage emphasizing synthesis and structure determination, typically by X-ray diffraction crystallography (XRD) and surface area/pore volume measurements. Attention has turned increasingly toward potential applications,[1] with the most valuable prospects including adsorption/separation[2,3] and catalysis.[4,5] MOFs with high surface areas and large pores are appealing catalysts and catalyst supports because they offer high densities of accessible catalytic sites. Being crystalline, MOFs offer tailorable structures that may include well-defined catalytic sites for selective conversions.[6] However, with their organic linkers, MOFs lack the robustness of widely applied solid catalysts, exemplified by metal oxides and zeolites—and the MOFs cannot be regenerated by burning off of carbonaceous deposits, because the linkers burn too. The lack of stability appears to be the major roadblock to applications of MOFs as catalysts.[4]

Notwithstanding this limitation, there is a rapidly growing literature of MOF catalysts,[4,6] but hardly any that assesses stability in operation. A few reports document MOF catalyst deactivation resulting from inhibition and clogging of pores by reaction products,[7] unzipping of the structures as alcohols react to break carboxylate linker–node bonds,[8] or as catalytic metals are lost by leaching.[9] These reports include examples of organic compounds such as carboxylic acids adsorbing on catalytically active sites or damaging framework structures and causing loss of catalytic activity. These reports characterize changes to the MOF catalysts before and after deactivation, but there is a lack of data quantifying the dynamics of structural changes of MOFs as they are undergoing deactivation. Our goal was to obtain such information as part of an investigation of the operation of a MOF catalyst in a broad context—by unravelling the processes of activation, deactivation, and ultimate demise as they depend on the MOF synthesis conditions.

We chose a widely investigated, well-characterized MOF known for its robustness (UiO-66[10-13]), which incorporates Zr_6O_8 nodes that offer sites for acid-base-catalyzed reactions such as those occurring on metal oxides and zeolites.[14] The MOFs were synthesized with a modulator (acetic acid) present in various concentrations to provide a family of samples with various node ligand compositions, including acetate.[15-18] We chose methanol dehydration as the catalytic test reaction, because it has the advantages of being stoichiometrically simple and taking place under mild conditions, providing opportunities for investigation with a flow reactor fed with methanol as a vapor-phase reactant. Our tactics were to characterize MOF samples after various times on stream to assess changes in their properties occurring during operation as catalysts. The samples were characterized with XRD, Brunauer-Emmett-Teller (BET) surface area measurements, scanning electron microscopy (SEM), and ^{1}H NMR spectroscopy of digested samples that quantify the organic components. The results demonstrate how the MOF node ligands acetate and formate, which arise in the syntheses, are catalytic reaction inhibitors; how the catalyst is activated by removal of these inhibitors by reaction with methanol to form methyl esters that desorb; and how the catalyst undergoes deactivation as methanol reacts to form inhibitor methoxy ligands on the nodes and to break node–linker bonds, unzipping the crystalline structure and causing the demise of the catalyst even while the catalyst particles still seem to be largely intact.

EXPERIMENTAL METHODS

Synthesis of UiO-66 with Acetic Acid Modulator. A family of UiO-66 samples was synthesized with well-tested methods[10,15] as 0.125 g of $ZrCl_4$ (0.540 mmol, >99.9%, Sigma Aldrich) and various amounts of acetic acid (0.2, 1.0, or 3.3 mL, ACS reagent grade, Supelco) were dissolved in 15 mL of N,N-dimethylformamide (DMF, ACS reagent grade >99.8%, Sigma Aldrich) and 0.2 mL of deionized water in an 8-dram vial using ultrasound for 5 min to dissolve the components. The linker precursor benzene-1,4-dicarboxylic acid (H_2BDC, 0.095 g, 0.570 mmol, 98%, Sigma Aldrich) was then added to the solution and dissolved by application of ultrasound for 20 min. Eight such vials were then held under static conditions in a preheated oven at 393 K for 24 h. MOF precipitates formed and were isolated by centrifugation after cooling to room temperature. The solids were washed with DMF (30 mL) three times over two days to remove unreacted precursors and then with acetone (30 mL) four times over two days to remove DMF. The resultant powders were dried in air at room temperature, mixed to form a single batch, and activated at 363 K under vacuum for 2 h to gently desorb remaining trapped solvents; each sample was subsequently dried at 393 K under vacuum for 12 h. After these steps, each powder sample was transferred, under vacuum, to an argon-filled glovebox for storage until characterization or catalyst testing.

The purpose of using various amounts of acetic acid modulator was to give UiO-66 samples having various contents of acetate (from acetic acid) and formate (from decomposition of DMF) as ligands on the MOF nodes.[8,15,19] Acetic acid was chosen as a modulator because the acetic acid to $ZrCl_4$ ratio leads to quantifiable differences in the resultant MOFs,[15,20-22] including the node compositions, which we intended to vary because they influence the catalytic properties for alcohol dehydration reactions.[8,14] The samples are respectively referred to as UiO-66aa6, UiO-66aa30, and

UiO-66aa100, where the number in each name represents the molar ratio of acetic acid to $ZrCl_4$ in the syntheses.

MOF samples before and after use as catalysts were characterized by the methods described below.

Powder X-ray Diffraction (PXRD). PXRD patterns were obtained for the MOFs before and after catalyst performance testing for various times on stream in a catalytic flow reactor. Data were obtained with a D8 Eco Advance Powder Diffractometer with a Lynx-EX detector. Data were recorded in the range $5° < 2\theta < 35°$ with a 0.2° step size and a 0.2 s dwell time.

BET Surface Area Measurements. N_2 adsorption isotherms of unused and used catalyst samples were recorded with a Micromeritics Tristar II 3020 instrument with the sample held at 77 K. Each sample was heated to 393 K under high vacuum for 12 h prior to recording of the isotherms.

SEM. SEM images of the MOF samples, including fresh catalysts and those used for various times on stream, were collected with a Thermo Fisher Environmental Quattro SEM instrument. Data for each sample were collected with the same magnification, spot size, and voltage, giving evidence of how the MOF morphology, crystallinity, and particle size changed with time on stream. Images showing the particles in each sample were recorded at two separate locations at the same magnification. To demonstrate the lack of significant beam damage, an image was taken as the first and as the final image. Each particle size measurement represents at least 100 particles in a given sample, chosen at random.

Sample Digestion and Characterization by ^{1}H NMR Spectroscopy. Liquid ^{1}H NMR spectra were recorded of MOF samples that had been digested in NaOH in D_2O, as before.[8,15,19]

The procedure gives solutions with spectra providing quantitative evidence of the composition of the organic components in the MOFs. Each sample was prepared by weighing 10 mg of an activated MOF into a 1.5 mL centrifuge vial followed by the addition of 1.00 mL of 1.00-*M* NaOH (ACS Reagent Grade ≥ 97.0%, Sigma-Aldrich) in D_2O (99.9%, Cambridge Isotope Laboratories). Samples that had been used as catalysts were prepared similarly but with 100 mg of sample that included both the MOF and inert packing particles from the flow reactor (*vide infra*) and 1.00 mL of digestion solution. Each vial was capped and inverted several times before the sample was allowed to digest for 24 h. This method allowed for analysis of any organic MOF components derived from the solvent, linker precursor, modulator, and methanol used in the catalysis experiments (the inorganic, node-derived components formed precipitates). After 24 h, the clear supernatant solution was transferred to an NMR tube, and ^{1}H NMR spectra were recorded with a Bruker Avance DPX-500 NMR spectrometer (500 MHz). The relaxation delay was set to 24 s to ensure recording of reliable integrals for accurate determination of relative concentrations of the molecular organic components. The number of scans per sample was 16. The samples taken from the catalytic reactor, containing inert particles in addition to the MOF particles, incorporated less MOF than the others and gave data with larger errors.

Catalytic Reaction Experiments in a Flow Reactor. Methanol dehydration catalysis was carried out in a conventional once-through tubular plug-flow reactor with an inside diameter of 0.5 cm at atmospheric pressure and temperatures ranging from 473 to 573 K, with reactants and products entirely in the vapor phase. The reactor was mounted vertically in an electrically heated furnace; the equipment and methods are described elsewhere.[8] Catalyst beds consisted of mixtures of 25 mg of activated MOF catalyst particles mixed with 1.00 g of inert α-Al_2O_3 particles (100–200 mesh, Sigma Aldrich); the inert particles were included to facilitate radial mixing of the reactant/product stream and give nearly plug flow and nearly isothermal operation. To avoid air exposure, these mixtures were prepared in the glove box by grinding with a mortar and pestle for 60 s then loaded into the reactor, which was sealed before removal from the glovebox.

Methanol was vaporized and flowed at a constant rate into the reactor in a mixture with helium carrier gas (UHP 99.999%, Praxair) that flowed through a sparger/saturator holding liquid methanol at 303 K. Electrical heating tape on the lines downstream of the sparger kept the temperatures >318 K to prevent condensation of the methanol. Downstream of the reactor, the lines were similarly heated and held at temperatures >393 K to prevent condensation in the effluent stream. The feed partial pressures were 220 mbar of methanol (HPLC Grade 99.9%, Sigma Aldrich), determined by the vapor pressure of methanol in the temperature-controlled sparger at 303 K, and 780 mbar of helium, with the total feed flow rate being 12.5 mL (NTP)/min. The total flow rate was controlled by a mass flow controller (MFC) in the helium line upstream of the sparger. Deviations from the desired helium flow rate contributed negligibly to the errors in the catalyst performance data. Product vapors were analyzed with an online Agilent 5890 gas chromatograph (GC) equipped with a Porapak Q 80/100 2-m, 2-mm packed column and an FID detector. GC data were collected at 10-min intervals during steady-state flow of the reactant; the methanol conversions were generally <10%. Reaction experiments were run for various times on stream with each catalyst, and samples were removed from the reactor for characterization by the methods mentioned above; each run terminated as the methanol feed was stopped, followed by rapid cooling then sealing of the reactor and transfer to the glove box, where the catalyst was removed and stored.

The mass of the catalyst bed, including 25 mg of MOF, was chosen as a compromise between optimizing reaction conditions and providing sufficient sample for characterization. The rates of deactivation of the MOF catalysts under the chosen conditions allowed capture of data characterizing the full catalyst life-cycle in experiments that were not too long and carried out with single batches of each MOF. The characterization experiments, including repetitions to determine reproducibilities, consumed almost all of the samples and led to errors in the surface area and NMR data that are substantially greater than those characterizing the unused MOF samples that were not mixed with inert particles. An accounting and rationale of the allotment of recovered samples are presented in the Appendix.

RESULTS

MOFs Synthesized with Various Node Ligand Compositions. The MOF syntheses, under conditions summarized in Table 2.1, were characterized by good reproducibility, as shown by data characterizing separate batches of UiO66aa30 shown in Figure A2.1 in the Appendix. Only single batches of UiO-66aa6 and UiO-66aa100 were made because single batches gave sufficient yields for all the planned experiments.

Table 2.1. Properties of UiO-66 Catalysts Synthesized with various Acetic Acid Modulator/ZrCl$_4$ Ratios.

MOF	molar ratio of modulator/ ZrCl$_4$ in synthesis	time on stream (min)	area of prominent peak in XRD pattern (a.u.)	BET surface area (m^2/g)	average MOF particle diameter (nm)	percentage of node ligands to which formate is bonded[a,c]	percentage of node ligands to which acetate is bonded	percentage of node ligands to which linker derived from 1,4- BDC is bonded	percentage of node ligands to which methoxy is bonded
UiO-66aa6	6	0	N/A	1530 ± 1.5	130 ± 20	4 ± 1	3 ± 1	90 ± 5	0
UiO-66aa6 mixed with α-Al$_2$O$_3$ particles[b]	6	0	0.017	24 ± 1.5	140 ± 15	6 ± 1	5 ± 1	90 ± 5	0
		45	0.020	10.3 ± 1.5	115 ± 20	0	0	80 ± 15	20 ± 15
		150	0.010	12.9 ± 1.5	110 ± 15	0	0	80 ± 15	20 ± 15
		330	0.0004	9.9 ± 1.5	95 ± 13	0	0	50 ± 15	50 ± 15
		700	0		90 ± 13	0	0	80 ± 15	20 ± 15
UiO-66aa30	30	0	N/A	1382 ± 1.5	190 ± 27	4 ± 1	12 ± 1	85 ± 5	0
UiO-66aa30 mixed with α-Al$_2$O$_3$ particles	30	0	0.042	25 ± 1.5	210 ± 39	4 ± 1	11 ± 1	85 ± 5	0
		45	0.017	16.7 ± 1.5	220 ± 34	1 ± 1	0	80 ± 15	20 ± 15
		150	0.031	15.1 ± 1.5	215 ± 31	0	0	80 ± 15	20 ± 15
		330	0.0014	12.2 ± 1.5	225 ± 30	0	0	80 ± 15	20 ± 15
		1000	0	3.5 ± 1.5	190 ± 36	1 ± 1	0	60 ± 15	40 ± 15
UiO-66aa100	100	0	N/A	1629 ± 1.5	350 ± 30	3 ± 1	14 ± 1	80 ± 5	0
UiO-66aa100 mixed with α-Al$_2$O$_3$ particles	100	0	0.078	27 ± 1.5	380 ± 30	4 ± 1	13 ± 1	80 ± 5	0
		45	0.0035	12.7 ± 1.5	350 ± 33	0	0	80 ± 15	20 ± 15
		150	0.0014	14 ± 1.5	330 ± 28	0	0	80 ± 15	20 ± 15
		330	0.0003	11.6 ± 1.5	340 ± 36	0	0	80 ± 15	20 ± 15

		600	0	9.0 ± 1.5	270 ± 32	0	0	80 ± 15	20 ± 15

[a] The percentage of the node ligands to which formate was bonded was calculated by: $n_{formate}/(n_{formate} + n_{acetate} + 2 \times n_{terephthalate} + n_{methoxy})$, where n is the number of mols; a comparable statement pertains to acetate, and it was assumed that the linker 1,4-benzenedicarboxylate was a bidentate ligand. [b] MOF particles were mixed with α-Al_2O_3 particles in a mass ratio of 1:40. [c] Errors were determined from the repeat conversion vs. time on stream data and represent variations in the mass of UiO-66 from run to run and are the basis for the error bounds shown here.

The physical properties of the MOFs (Table 2.1) are compared in Table A2.1 in the Appendix with literature values for UiO-66 samples that, like ours, were synthesized with acetic acid modulator. The PXRD patterns of our three samples are characterized by prominent peaks at 2θ = 7.45° and 8.60° (Figure A2.2 in the Appendix), consistent with those reported[8,10,15-22] and indicating the [Fm-3m] space group. The BET surface areas of UiO-66 synthesized with 6, 30, and 100 mols of acetic acid per mol of $ZrCl_4$ were found to be 1530, 1382, and 1629 m^2 g^{-1}, respectively. Because our synthesis conditions differed from those reported in terms of the relative concentrations of the various synthesis reagents, these and the other properties of our samples differ from those of the reported UiO-66 samples made with acetic acid modulator; however, the trends indicated by variations in the synthesis conditions are consistent with reported values.

The ^1H NMR data collected for the as-synthesized MOFs (Table 2.1) are in line with reported results,[8,15,19] confirming that higher ratios of acetic acid to $ZrCl_4$ in the syntheses gave increased fractions of acetate ligands and decreased fractions of formate ligands on the nodes. The pattern is as expected: in the synthesis, DMF reacts to give formate and dimethylamine[8] (observed in the ^1H NMR spectra, at chemical shifts of 8.3 and 2.0 ppm, respectively). The formate and acetate compete with 1,4-benzenedicarboxylate formed from the linker precursor H_2BDC for sites on the nodes.[14] Our data indicate values of 3 ± 1, 12 ± 1, and 14 ± 1 as the respective percentages of node ligands that were acetate (Table 2.1), showing that the syntheses met the goal of providing a family of samples with a substantial range in node composition. The pattern is qualitatively in line with that reported by Wei et al.,[15] but the quantitative values differ substantially because of the different synthesis conditions, summarized in Table A2.1 in the Appendix. Other species observed in the ^1H NMR spectra were the expected 1,4-benzenedicarboxylate and dimethylamine.

The SEM images of UiO-66aa6 and UiO-66aa30 show that the particles were roughly spherical, but the images of the UiO-66aa100 particles resemble octahedra (details in Figure A2.3A–F in the Appendix), in agreement with reported observations of UiO-66 showing how increases in the ratio of modulator to $ZrCl_4$ in the synthesis resulted in more highly crystalline particles.[15,20-22] The average particle diameters of as-synthesized UiO-66, modulated with 6, 30, and 100 mols of acetic acid per mol of $ZrCl_4$ were found to be 130 ± 20, 190 ± 27, and 350 ± 30 nm, respectively. Wei et al.[15] provided images of their MOFs that are consistent with ours, finding near-spherical particles for the samples made with the lower ratios of acetic acid to $ZrCl_4$ and octahedral shapes when the ratios were higher (Table A2.1 and A2.2 in the Appendix). They did not provide particle size values, but their trend of increasing particle size with increasing acetic acid to $ZrCl_4$ ratio is consistent with ours. Schaate et al.[20] used the Scherrer equation and PXRD data to measure the sizes of particles of UiO-66 made with 0, 1, 3, 5, 10, 20, and 30 mols of acetic acid per mol of $ZrCl_4$, finding the same trend, with the particle diameters being in the range of 72–171 nm. Morris et al.[22] reported comparable data, confirming the trends in particle shape and size. Details are given in Table A2.2 in the Appendix.

Catalyst Performance Data Demonstrating the Life Cycle of UiO-66 in Methanol Dehydration. Methanol conversion was negligible in the absence of catalyst under our conditions. When MOF particles were present in the reactor, methanol dehydration took place in the absence of side reactions:

$$2\mathrm{CH_3OH} \rightarrow \mathrm{CH_3OCH_3} + \mathrm{H_2O} \tag{2.1}$$

Because an FID detector was used, water was not observed in the chromatograms. Conversions were determined from the dimethyl ether and methanol peak areas. Because the conversions were differential, as shown by the nearly linear dependence of conversion on inverse space velocity (Figure A2.4 in the Appendix), the catalyst performance data are reported as reaction rates per unit mass of catalyst. Methyl formate and methyl acetate were observed in the chromatograms, consistent with expectation[8,14,15,19] and with ^1H NMR data demonstrating the presence of acetate and formate in the as-synthesized MOFs (Figure A2.5 in the Appendix).

In other alcohol dehydration reactions[8,19] (and in methanol dehydration[14]) catalyzed by MOFs with Zr_6O_8 or other metal oxide cluster nodes,[23,24] these esters have been observed to be desorbed from the catalyst, evidently formed as the alcohol reacted with the node carboxylate ligands.

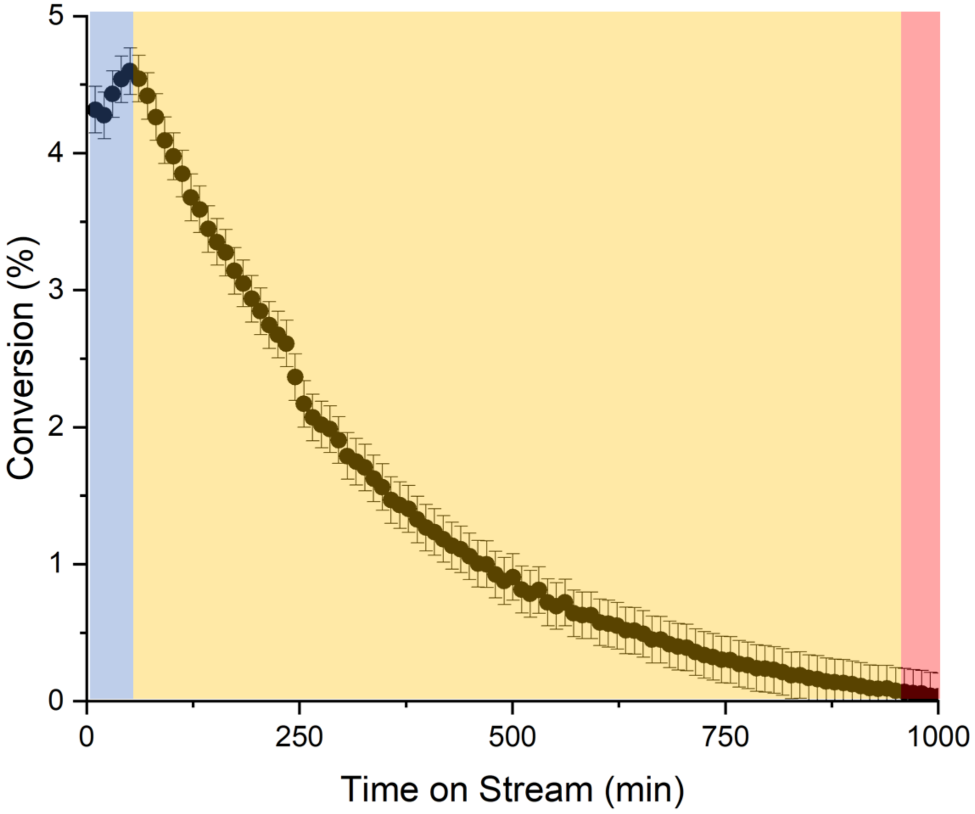

Figure 2.1. Methanol dehydration catalyzed by UiO-66aa30 in a flow reactor: evidence of stages of MOF catalyst performance. Reaction conditions: 548 K, feed partial pressure, 220 mbar of methanol and 780 mbar of helium; total feed flow rate, 12.5 mL(NTP)/min; catalyst mass, 25 mg of MOF and 1.00 g of α-Al_2O_3. The MOF catalyst life cycle includes an activation stage during which the conversion proceeds to a maximum (blue) followed by a deactivation stage (yellow-brown) that leads to the nearly complete loss of catalytic activity (red). Error bars are precisions determined in repeat experiments. Major sources of error are associated with losses in sample during preparation/handling and inconsistencies in the product analyses by GC.

Catalyst performance data demonstrating the life cycle of UiO-66 in methanol dehydration are characterized by three regions (Figure 1):

1) Activation: During typically the first 45 min on stream, the conversion of methanol increased.

2) Deactivation: Thereafter, the conversion declined. In the analysis that follows, it is shown that deactivation was taking place from time zero on stream. Initial rates of deactivation were determined by extrapolating the conversion-time on stream data following the activation stage to zero time on stream to deconvolute the data and resolve the activation and deactivation phenomena.
3) Demise: When experiments were conducted long enough, the methanol conversion approached zero.

To characterize changes in the MOF properties during these stages, samples (in separate experiments, each beginning with unused catalyst) were removed from the reactor after various times on stream: 45, 150, 330, and approximately 600 min (Figure 2.2).

Catalyst Activation by Removal of Methyl Acetate and Methyl Formate. In catalysis experiments carried out at 523 K, the MOFs underwent activation slowly enough to observe clearly (Figure 2.3), but at 548 K the activation period was too short to characterize well for UiO-66aa6(e.g., Figure A2.7 in the Appendix). GC evidence of methyl acetate and methyl formate in the product stream was obtained during the activation periods. As shown in Figure 2.4, the yields of these gas-phase products declined to almost zero at the end of the activation period. ^{1}H NMR spectra of digested samples removed from the reactor after 45 min on stream (Table 2.2) confirm that acetate and formate had been largely removed from the MOFs during catalytic operation. These results show that the formate and acetate ligands on the MOF nodes[14,15,22] were catalytic reaction inhibitors, which implies that the catalytic sites were sites on the nodes.

Loss of Accessible MOF Surface Area and Changes in MOF Composition During Catalyst Activation. BET surface area measurements show the loss of accessible surface area during the activation period (Table 2.2; the errors are precisions determined in repeat experiments)—note that the areas represent mixtures of the MOF particles with inert alumina particles present in the reactor. Complementary ^{1}H NMR spectra of these samples digested in NaOH show that there were changes in the MOF structure and ligands during the activation period, during which the acetate and formate had been almost completely removed from the MOFs (Table 2.2).

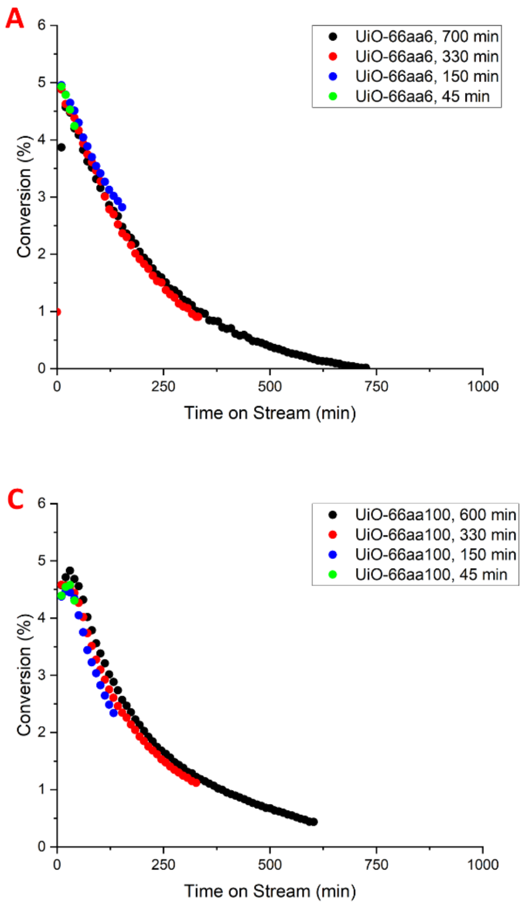

Figure 2.2. Conversion of methanol catalyzed by UiO-66aa6 (A), UiO-66aa30 (B), and UiO66aa100 (C) for 45 (green), 150 (blue), 330 (red), and at least 600 min on stream (black). Reaction conditions: 548 K, feed partial pressures: 220 mbar methanol and 780 mbar helium; total feed flow rate 12.5 mL (NTP)/min; catalyst mass, 25 mg of MOF particles mixed with 1.00 g of particles of α-Al_2O_3. Comparison with data obtained in separate experiments led to estimates of typical experimental error in conversion of 0.09, 0.17, and 0.12%.

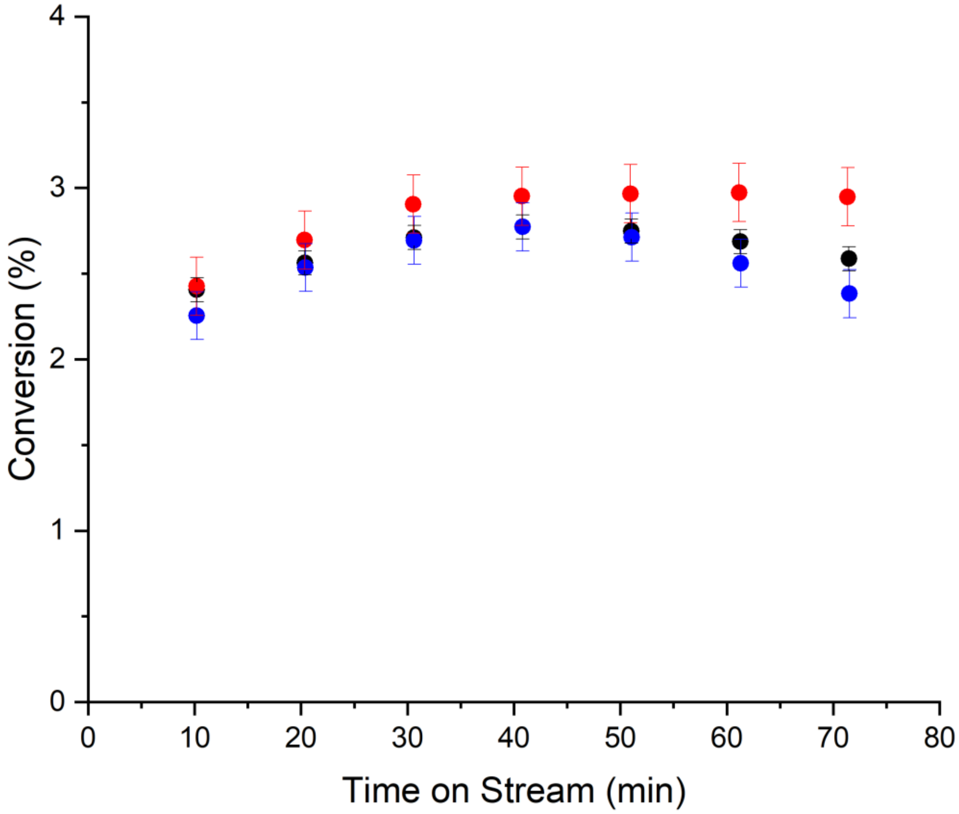

Figure 2.3. Catalyst activation shown by increasing conversion of methanol in reaction catalyzed by MOF UiO-66aa6 (black), UiO-66aa30 (red), and UiO-66aa100 (blue). Reaction conditions: temperature, 523 K; feed partial pressures, 220 mbar of methanol and 780 mbar of helium; total feed flow rate 12.5 mL (NTP)/min; catalyst mass, 25 mg of MOF particles mixed with 1.00 g of α-Al_2O_3 particles.

Loss of MOF Crystallinity During Catalyst Activation. Samples taken from the reactor after a clear activation period of 45 min during operation at 548 K were further characterized with PXRD. For proper comparisons, the diffraction patterns of the used catalyst samples were compared with diffraction patterns of the unused catalyst samples that were identically mixed with particles of α-Al_2O_3. The comparisons show that UiO-66aa100 and UiO-66aa30 lost crystallinity during the activation period, as indicated by the peaks at $2\theta = 7.45°$ and $8.60°$; a nearly complete disappearance of these peaks was observed for UiO-66aa100. In contrast, the data characterizing MOF UiO-66aa6 show that the aforementioned peaks even increased by roughly 15% after the activation period of 45 min, perhaps associated with the removal of formate and acetate. The data thus show that that changes in the MOF framework structure accompanied the reactions of methanol with the node acetate and formate ligands and that the MOF unzipping took place to various degrees that depended on the node ligand composition; broadly, the results are consistent with the inference that reactions of methanol with the MOF led to losses of crystallinity.

Table 2.2. Changes in MOF Properties during Activation Period in Methanol Dehydration Catalysis.

MOF	surface area of sample consisting of MOF mixed with inert Al_2O_3 particles (m^2/g)		percentage of node ligands to which formate bonded, determined by ^1H NMR spectroscopy		percentage of node ligands to which acetate bonded, determined by ^1H NMR spectroscopy	
	before catalysis	after activation (45 min on stream)	before catalysis	after activation (45 min on stream)	before catalysis	after activation (45 min on stream)
UiO-66aa6	24.0 ± 1.5	10.3 ± 1.5	6 ± 1	0	5 ± 1	0
UiO-66aa30	25.0 ± 1.5	16.7 ± 1.5	4 ± 1	1 ± 1	11 ± 1	0
UiO-66aa100	27.0 ± 1.5	12.7 ± 1.5	4 ± 1	0	13 ± 1	0

Consistent with this inference, the NMR data (Table 2.2) show that each of the samples UiO66aa6, UiO66aa30, and UiO66aa100 had lost node–linker bonds during the activation period, in agreement with the conclusion that MOF unzipping resulted from the reaction of methanol with the node–linker bonds to form methyl esters with the linkers. This ester formation, which has been reported for reactions of various alcohols with these and similar node–linker bonds,[8,14,19,23,24] has been shown to lead to the formation of methoxy ligands on the nodes, and our ^{1}H NMR data confirm the presence of methoxy ligands, showing that the percentage of node ligands to which methoxy was bonded after the activation period was roughly 20, 20, and 20 percent for each of the three MOFs. These data provide clear evidence of MOF disintegration during catalysis—and, we emphasize, even during the initial activation period—thus, it is clear that both activation and deactivation of the MOF catalyst were taking place during the initial stage that we refer to as the activation stage.

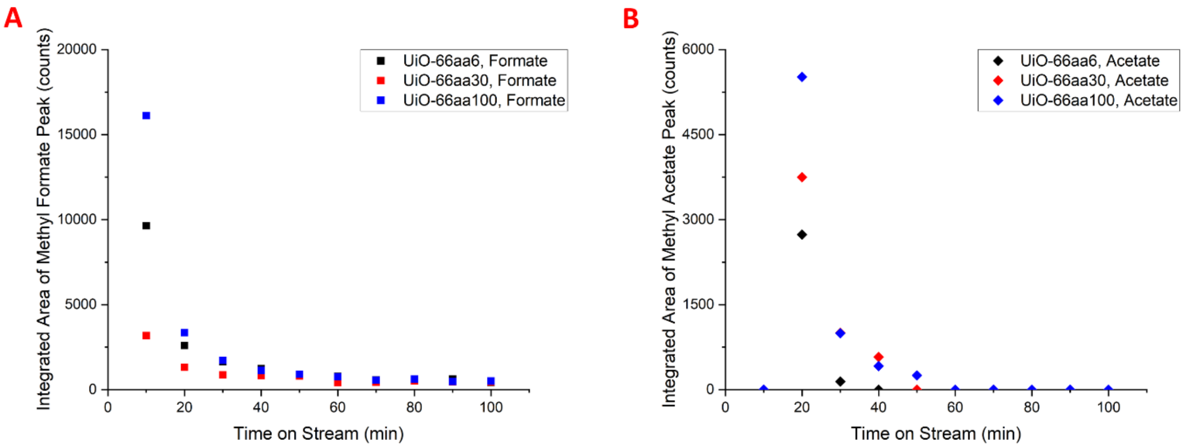

Figure 2.4. Qualitative GC evidence of desorption of methyl formate (A) and methyl acetate (B) from MOF catalysts during the first 100 min on stream. Reaction conditions: 548 K, feed partial pressures of 220 mbar methanol and 780 mbar helium; total flow rate 12.5 mL (NTP)/min; catalyst mass, 25 mg of MOF particles mixed with 1.00 g of α-Al_2O_3 particles.

MOF Catalyst Deactivation and Demise. Following the maximum conversion achieved during the activation period, the catalytic activity of each MOF decreased steadily until it was barely detectable. This stage of the catalytic life cycle is referred to as deactivation, but we reemphasize that the evidence stated above shows that deactivation was occurring even from the beginning—in competition with activation. To characterize the changes in MOF properties following the activation stage, the catalyst bed in each experiment (each of which began with an unused catalyst sample) was removed from the reactor after a period of operation 150, 330, or least 600 min, again by stopping the feed flow, cooling and sealing the reactor, and moving it to the glove box. The longest time before removal of the longest-used sample varied from catalyst to catalyst because the time to near demise varied from one to another.

At 548 K, each MOF (under the reaction conditions described above) underwent deactivation as shown by the decreases in conversion shown in Figure 2.5. The data indicate a slower deactivation of UiO-66aa30 than of UiO66aa6 and UiO66aa100.

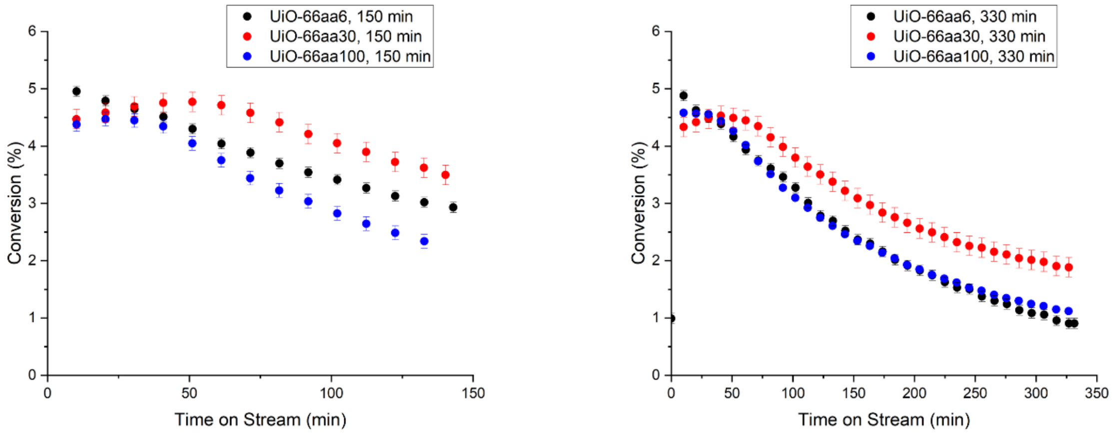

Figure 2.5. MOF catalyst deactivation illustrated for samples of acetic acid-modulated UiO-66, with 6 (black), 30 (red), and 100 (blue) mols of acetic acid per mol of $ZrCl_4$ respectively used in the synthesis, with the catalyst samples removed from the reactor after 150 (left) and 330 min (right). Reaction conditions: 548 K, feed partial pressures: methanol, 220, helium, 780 mbar; total flow rate, 12.5 mL (NTP)/min; catalyst mass, 25 mg of MOF particles mixed with 1.00 g of α-Al_2O_3 particles. Error bars represent precisions determined in four experiments.

Initial reaction rates—that is, the methanol dehydration rates characterizing the undeactivated catalysts in the absence of acetate and formate inhibitors—were estimated for each MOF by extrapolating rates determined from differential conversions observed during the deactivation stage to zero on-stream time. Data demonstrating that the conversions were low enough to be differential are shown in Figure A2.4 in the Appendix (the plot determines reaction rate directly as the slope of the fractional conversion of methanol vs inverse space velocity, which has units of (g of catalyst × min/mol of methanol fed). By this method, using single points, we estimated values for each MOF without the inhibiting ligands. The extrapolation gave estimates of rate values shown in Table 2.3. Table 2.3 also includes initial rates of catalyst activity loss, each determined as the negative of the slope of catalytic reaction rate vs. time on stream, extrapolated to zero time on stream; details are given in the Appendix.

Table 2.3. **Rates of Catalytic Reaction and of Catalyst Deactivation extrapolated to pertain to MOFs without Inhibitor Formate and Acetate Ligands**

MOF	temperature (K)	10^3 × rate of catalytic reaction ($\mathrm{mol_{methanol\ converted}\ g^{-1}_{MOF}\ min^{-1}}$)	10^7 × rate of catalyst deactivation ($\mathrm{mol_{methanol\ converted}\ g^{-1}_{MOF}\ min^{-2}}$)
UiO-66aa6	573	0.36 ± 0.01	30.0 ± 0.7
	548	0.21 ± 0.01	8.6 ± 0.1
	523	0.17 ± 0.00	5.6 ± 0.1
	510	0.11 ± 0.01	1.8 ± 0.1
UiO-66aa30	573	0.53 ± 0.01	21.2 ± 0.2
	548	0.24 ± 0.01	7.4 ± 0.1
	523	0.16 ± 0.01	3.3 ± 0.1
	498	0.05 ± 0.01	2.0 ± 0.1
UiO-66aa100	548	0.23 ± 0.01	11.2 ± 0.2
	523	0.13 ± 0.01	5.6 ± 0.1
	510	0.11 ± 0.01	3.5 ± 0.1
	498	0.07 ± 0.01	3.2 ± 0.1

Loss of MOF Crystallinity During Methanol Dehydration Catalysis. PXRD patterns of the MOFs (Figure 2.6) show that the peaks characterizing the crystalline material declined during operation. Nearly complete loss of the aforementioned peaks characteristic of UiO-66aa100 was observed even during the activation stage, and no evidence of MOF recrystallization was observed in the deactivated samples. The PXRD patterns show that after 330 min on stream, both UiO-66aa6 and UiO-66aa30 had undergone nearly complete loss of the characteristic peak at $2\theta = 7.45°$. There was essentially no change in the PXRD patterns between this state and the state at which the longest-running sample was removed from the reactor.

Although these samples after 330 min of operation as catalysts had lost essentially all of their crystallinity, as indicated by the XRD data, the material remained catalytically active. The result implies that the material formed during the degradation, even with node–linker bonds broken and the interior MOF structure markedly changed, was still catalytically active, suggesting that some node surfaces were still accessible and/or that material such as zirconium oxide or zirconium hydroxide had formed. Characterization of these ill-defined materials was beyond the scope of this work.

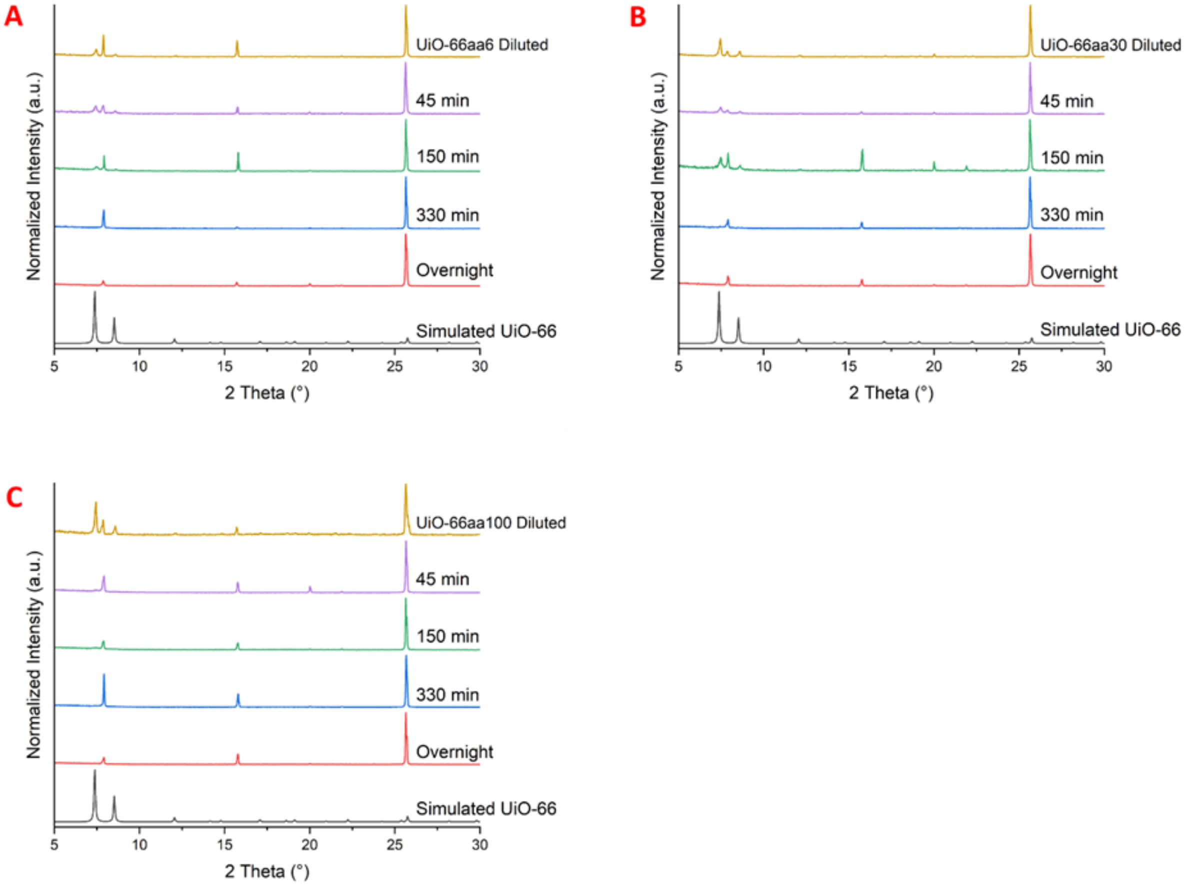

Figure 2.6. Loss of crystallinity of MOF UiO-66aa6 (A), UiO-66aa30 (B), and UiO-66aa100 (C) under catalytic reaction conditions. All PXRD patterns were normalized to the maximum peak of the inert α-Al_2O_3. After the final two stages, lasting 330 min and overnight, no evidence of crystalline UiO-66 was observed.

Loss of MOF Surface Area During Catalyst Deactivation. Data characterizing the loss in surface area of the MOFs during catalytic operation are shown in Figure 2.7. Recall that the MOF particles were mixed with inert alumina particles, so that surface areas reported in this figure are per unit mass of the mixtures of MOFs and inert particles. The initial surface areas of the samples UiO-66aa6, UiO-66aa30, and UiO-66aa100 were 24.0, 25.0, and 27.0 (each ± 1.5 m^2/g), respectively. These surface areas are less than those expected from the 1:40 dilutions in α-Al_2O_3 which would have been between 35 and 42 m^2 g^{-1}. The differences imply that some mechanical degradation of the MOFs occurred during the grinding/mixing with α-Al_2O_3, consistent with results presented by Su et al.,[25] who showed that applying compressive pressure with a hydraulic piston pelletizer to UiO-66 nanocrystals caused significant decreases in the MOF surface area, with >90% reduction in surface area after compression at 1.9 GPa and >20% reduction in surface area after compression of 0.4 GPa. Complementary infrared spectra of these samples showed that node–linker bonds were broken, causing irreversible amorphization as pores collapsed. The initial surface areas decreased respectively by about 14, 8, and 14 m^2 g^{-1} during the activation periods as formate and acetate were removed from the nodes. Afterwards, the surface areas continued to decline, but more slowly, an additional 0.4, 4.5, and 1.1 m^2 g^{-1} respectively after 330 min on stream. In view of the estimated error of ± 1.5 m^2 g^{-1} in the surface area data, we infer that, among these MOFs, only UiO66aa30 underwent a significant decrease in surface area. In contrast, UiO-66aa6 and UiO-66aa100 had larger final surface areas of 9.9 and 9.0 m^2/g when the MOF was fully deactivated, possibly indicating the effects of the compositional changes that resulted from reaction with methanol. Samples characterizing the fully deactivated UiO-66aa30 and UiO-66aa100 had surface areas of 3.5 ± 1.5 and 9.0 ± 1.5 m^2 g^{-1}, indicating that the sites resulting from the removal of the ligands differed from one MOF to another. UiO-66aa30 was exposed to the reaction conditions for 400 min longer than UiO-66aa100, contributing to its lower surface area (recall that the objective of the final measurements was to characterize the almost fully deactivated catalysts). These changes are complex and not resolved by the data.

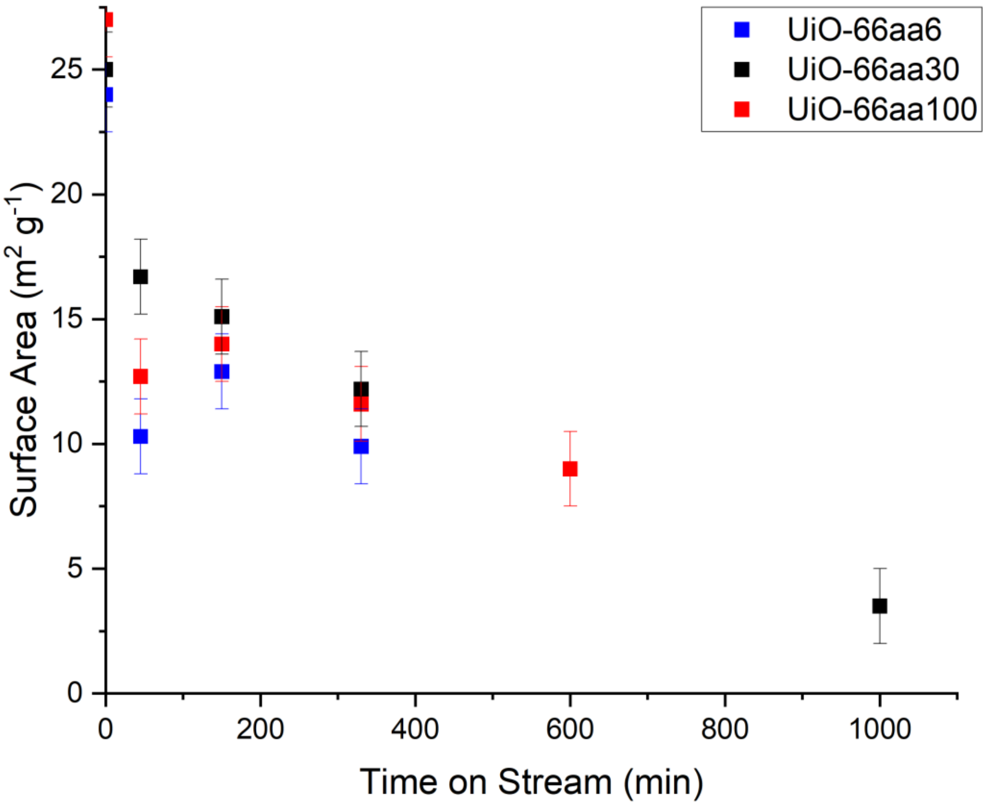

Figure 2.7. Loss of surface area during operation of the MOFs as catalysts. The MOF particles were mixed in a mass ratio of 1:40 with α-Al_2O_3 particles in the reactor, and the data represent areas of the mixtures.

NMR Evidence of Changes in MOF Node Ligand Environments During Catalyst Operation. To determine changes in the MOF compositions during catalysis, samples in separate experiments were removed from the flow reactor after times on stream of 150, 330, and at least 600 min, and then digested in NaOH in D_2O, followed by analysis of the liquid by ^{1}H NMR spectroscopy. No changes in acetate or formate content were observed after the activation period, consistent with the above-stated conclusion that these inhibitors were largely removed during that period. Nonetheless, the NMR data show that a few percent of the formate and acetate that were present initially remained in the MOFs after the activation stage, evidently on sites that were not catalytic sites.

During the activation period, methyl acetate was removed faster than methyl formate, with the rough average removal rates respectively being 17 $\mu mol_{acetate}$ min^{-1} g^{-1} and 5 $\mu mol_{formate}$ min^{-1} g^{-1}. Details of the estimates are given in the Appendix. The results of Table 2.1 are consistent with Yang's inference that catalysts lose activity as node catalytic sites are blocked by methoxy groups formed from methanol and bonded to the metal oxide cluster nodes.[14] However, the methoxy groups do not account for all the observed loss of catalytic activity, as shown by the data in Table 2.1 for the three catalysts after they had reached their demise at the longest times on stream—substantial fractions (typically more than half) of the node bonding sites were then occupied by ligands other than methoxy.

SEM Characterization of Catalysts After Various Times on Stream. SEM images of samples that had been used as catalysts for 150, 330, and at least 600 min show that the particle sizes decreased during operation, but not drastically; example data are shown in Figure 2.8. The particles remained intact, although the internal compositions and structures changed markedly, as shown by the NMR data (Table 2.1). These results, taken together, show that as the MOFs were unzipping and the internal structure and composition were changing in complex ways, the particle morphologies viewed by SEM remained largely unchanged over the course of our experiments.

The changes in particle diameters of MOFs UiO66aa6, UiO66aa30, and UiO66aa100 were found to be from 130 ± 20 to 90 ± 13; from 190 ± 27 to 190 ± 36; and from 350 ± 30 to 270 ± 32 nm, respectively. The data demonstrate a trend of decreasing particle size with increasing time on stream—with the possible exception of UiO-66aa30, for which the error bounds in diameter are so high that there is a lack of evidence of the change; correspondingly, this MOF also took a longer time to deactivate almost fully than the others (approximately 5 h more than the times characterizing the others).

The images are consistent with the suggestion of amorphization of the crystals near their surfaces and with the inference that the unzipping proceeded predominantly from the outer surfaces, but the NMR data of Table 2.1 make it clear that the unzipping extended into the full interior spaces of the MOF particles. These observations raise questions about mass transfer limitations, which are addressed in the Discussion.

The images of the used catalyst particles are not as sharp as those of the unused particles, as illustrated clearly in the images of UiO-66aa100 (Figure 2.8), which show that the edges of the particles became blurred after catalysis. This observation bolsters the inference stated above that MOF degradation proceeded predominantly from the outside surfaces toward the particle interiors.

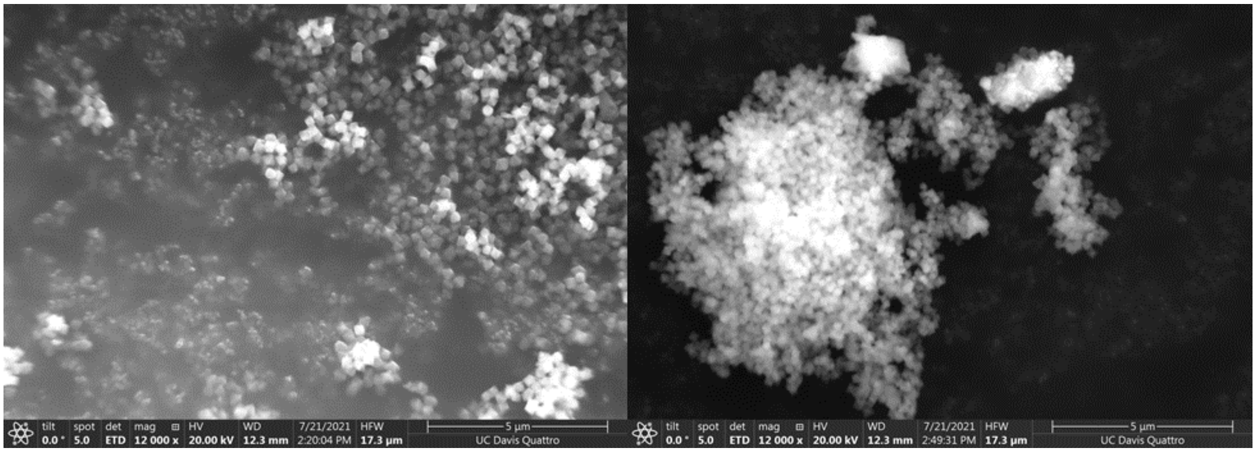

Figure 2.8. Comparison of UiO-66aa100 before (left) and after (right) use as a catalyst for 600 min on stream. Images were taken with the same magnification and instrument settings. A loss of features of the particles during catalysis is shown, with edges of the particles sharply defined prior to reaction and not visible following deactivation. Images are of MOF particles that were located between the much larger α-Al_2O_3 particles. Images showing the MOF particles with α-Al_2O_3 particles are provided in Figure A2.8 in the Appendix.

Initial Catalytic Reaction Rates and Apparent Activation Energies of the Deactivation. For analysis of the kinetics of the catalytic reaction and the catalyst deactivation, the data were extrapolated to zero time on stream. The extrapolations, illustrated in Figure A2.9 in the Appendix, were done only with data following the activation stage, because data recorded during that early stage represent the catalyst that was inhibited by the formate and acetate ligands that were present initially. Data for the extrapolations were recorded for UiO-66aa6, UiO-66aa30, and UiO-66aa100 at temperatures ranging from 498 to 573 K. Reaction conditions were as follows: feed partial pressures: 220 mbar of methanol and 780 mbar of helium; total feed flow rate, 12.5 mL (NTP)/min; catalyst mass, 25 mg of MOF (mixed with 1.00 g of α-Al_2O_3 particles). For analysis of initial rates of catalyst deactivation, the same extrapolation was done, again with exclusion of data determined during the activation stage, and the slopes of the curves fitting the conversion data as a function of time on stream were evaluated at zero time on stream. These analyses reflect the uncertainty in the demarcation between the stages referred to as activation and deactivation; the maximum conversion was chosen as the transition between the stages. Errors in the initial rates were determined by propagation of the errors in the conversions, estimated from repeat experiments. Apparent activation energies for the reaction and catalyst deactivation (Table 2.4) were determined from the estimates of the initial catalytic reaction rates and illustrated by the Arrhenius plots of Figures A2.10-11 in the Appendix. We emphasize that the activation energies are apparent, showing temperature dependence of reaction rates and not rate constants. The value characterizing methanol dehydration is complicated by mass transport limitations (*vide infra*), which shows that the rates are not intrinsic. The same caveats apply to the apparent activation energies characterizing the deactivation of the MOF catalysts.

Table 2.4. **Apparent Activation Energies characterizing the Catalytic Reaction and Catalyst Deactivation processes. Values were calculated by Extrapolation and Fitting of the Conversion vs Time on Stream Data, with the Conversions being Differential and Determining Catalytic Reaction Rates Directly.**

MOF	apparent activation energy (kJ/mol)	
	methanol dehydration reaction	catalyst deactivation
UiO-66aa6	42 ± 8	112 ± 18
UiO-66aa30	70 ± 10	100 ± 11
UiO-66aa100	51 ± 3	64 ± 5

DISCUSSION

Elucidation of the MOF Catalyst Life Cycle. Yang et al.[19] investigated UiO-66 and MOF-808 as catalysts for the *t*-butyl alcohol dehydration reaction, characterizing the samples at various times on stream with PXRD, BET surface areas, and ^{1}H NMR spectra of samples digested in NaOH. Their data demonstrate changes in the MOF as it reacted with the alcohol; Yang's group also reported comparable data for ethanol dehydration catalyzed by the MOFs UiO-66 and UiO-67.[8] These results demonstrated the MOF unzipping referred to above. The results presented here show that this process of catalyst degradation has some generality—occurring when a reactant (or product) can react with the MOF to break node–linker bonds.

The results reported here include characterization data providing quantitative evidence of catalyst activation, consistent with Yang's observations that inhibitor formate and acetate ligands are removed as methanol reacts with them to make esters that leave the catalyst and leave alkoxy ligands in their place on the MOF nodes.[8,19] Taken together, the data show that major compositional and structural changes took place within the UiO-66 particles during the life cycle. The data show how the activation and deactivation processes depend on the initial MOF node ligand composition. It is evident from the SEM images of the deactivated catalysts (Figure 2.8) that the catalysts lose almost all of their activity without major changes in particle shape and size, which implies that the major changes were internal to the particles. The lack of a simple pattern in the compositional data determined by NMR spectroscopy as the catalysts changed in operation (Table 2.1) shows that the phenomena are complex. They involve chemical change—including inhibition of node catalytic sites by methoxy groups formed from methanol and unzipping of the MOF—combined with physical changes affecting the accessibility of the catalytic sites in the particle interior spaces. We return to this latter point below.

The results reported here are unique in presenting an integrated, quantitative summary of these changes. They demonstrate an apparently irreversible set of changes leading to the demise of these MOFs as catalysts and show multiple vulnerabilities of MOFs as catalysts. The changes in catalytic activity of the MOF samples are correlated with each of the changing physical and chemical properties of the MOFs during the life cycle, as shown in Figure 2.9 and Table 2.3. Details follow.

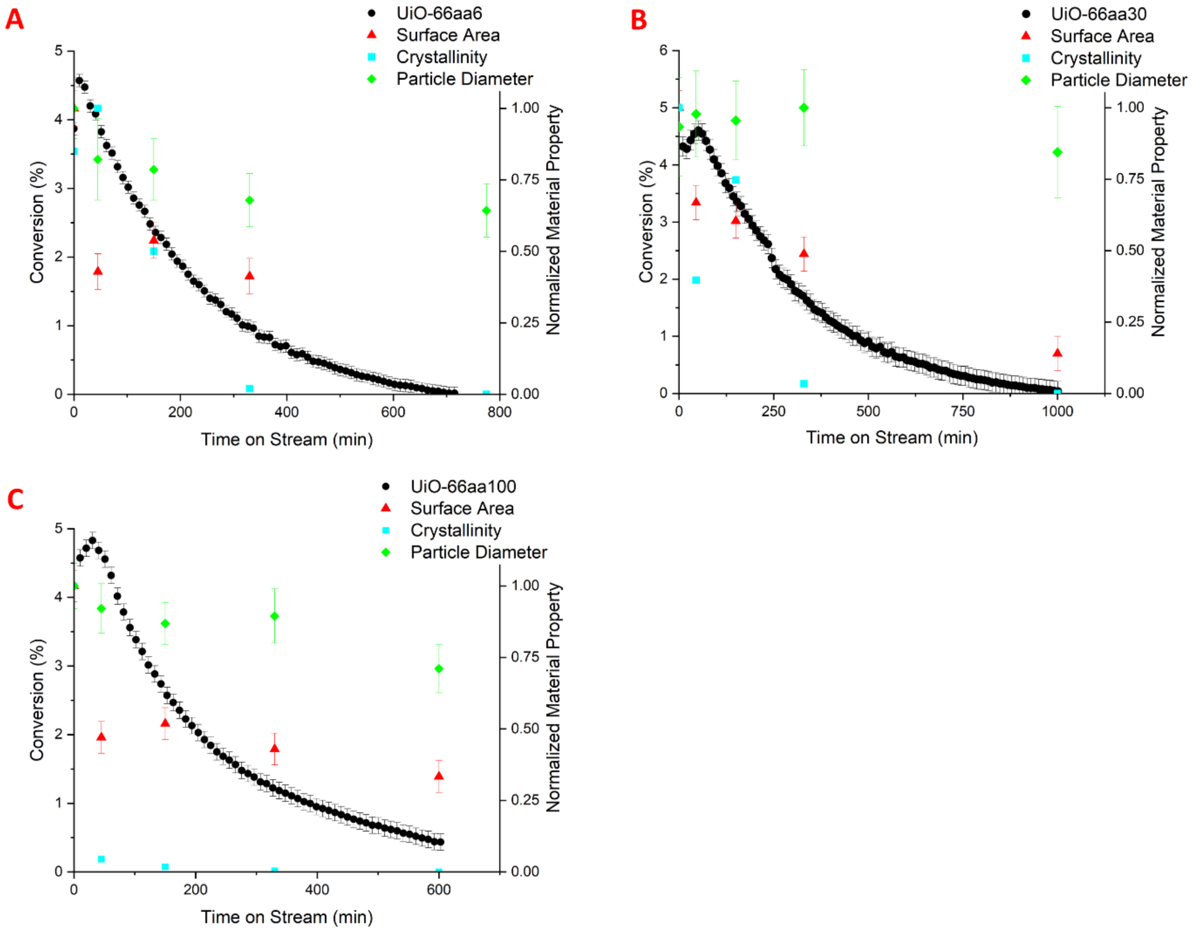

Figure 2.9. Life cycles of UiO-66aa6 (A), UiO-66aa30 (B), and UiO-66aa100; the data show how the physical properties of the MOFs changed as the catalyst is activated and then deactivated in operation in a flow reactor. Reaction conditions: 548 K, feed partial pressures of 220 mbar of methanol and 780 mbar of helium; total flow rate 12.5 mL (NTP)/min; catalyst was 25 mg of MOF particles mixed with 1.00 g of α-Al_2O_3 particles. The surface area (red), crystallinity (cyan), and particle diameter (green) data are normalized to their maximum values as shown on the right vertical axes. Further details are shown in Figures A2.12–14 in the Appendix.

Influence of the Initial MOF Composition on Catalyst Performance and Accompanying Structural Changes. The data show that changes in the MOFs with differing initial compositions determined by the modulator-to-$ZrCl_4$ ratios in the synthesis were substantially different from MOF to MOF in terms of the rates of the competing processes (Figure 2.9 and Figures A2.12–14 in the Appendix). The three samples differed in their initial node inhibitor contents; they lost these inhibitors by reaction with methanol within the first approximately 45 min of catalytic operation, but at different rates; thus, UiO-66aa30, the MOF made with the intermediate acetic acid to $ZrCl_4$ ratio in the synthesis, continued to undergo activation at times on stream when the other two MOFs had already entered the deactivation stage. The lack of a simple relationship between this ratio and the time required for activation indicates a trade-off that suggests an influence of the MOF structure. The data show that, consistent with earlier reports,[15,20-22] the MOF crystallinity increased with increasing modulator to $ZrCl_4$ ratios, which favored the nucleation and MOF self-assembly processes. Increased crystallinity might be beneficial in alcohol dehydration catalysis because of the cooperation of node Lewis acid and terminal OH sites.[14] Consistent with this suggestion, the different structures evidently were characterized by different rates of removal of the formate and acetate inhibitors by reaction with methanol, and the GC traces show that the desorption of methyl acetate was faster than that of methyl formate. The data are not sufficient to resolve these matters, and we posit that they are convoluted with mass transport limitations, as discussed in the next paragraphs.

Transport Limitations and the Locations of Reactions in the MOF Particles. Rates of reaction in porous catalyst particles such as MOFs may be influenced not just by the intrinsic rates of the reactions but also by the rates of transport of reactants and products into and out of the pores. Transport limitations in our catalysis are expected, because the window diameter of the smallest pores is estimated to be 6 Å for ideal crystalline UiO-66 and is close to the critical diameters of methanol and of dimethyl ether.[10] Transport resistance is commonly assessed by varying the transport distance (particle diameter) while keeping the particle composition and pore structure the same. But such experiments are lacking for MOFs, because synthesis of particles of varying sizes typically results in particles of various structures and compositions,[4] as has been shown here as well. Thus, there is a lack of data determining effectiveness factors of any MOF catalyst particles.[4]

The data reported here provide some insight into the transport effects and locations of reactions in the MOF particles, although they do not fully resolve matters. For example, the data characterizing the three MOFs show that after the longest observed time on stream, a substantial amount of 1,4-benzenedicarboxylate had been removed and replaced by methoxy. When taken with the complementary information provided by the SEM data showing that the particle sizes did not decrease much, the data lead to the conclusion that most of the particle interior had been accessed by methanol.

Further insights about the transport limitations are suggested by the changes in the MOF particle sizes during operation (Figure 2.9). The decrease in the particle sizes during operation, combined with the SEM evidence indicating amorphization of the MOF particles near their exterior surfaces, suggests that the breaking of node–linker bonds was more rapid near these exterior surfaces than near the particle centers, consistent with significant transport limitations within the porous structure. These limitations might have become more pronounced as the structure collapsed and as pore mouth blocking might have ensued. Such a collapse could be a major cause of catalyst deactivation by increasingly restricting access of methanol to the particle interiors with increasing time on stream. Thus, a plausible postulate is that the demise of the catalyst was largely caused by pore blocking by amorphous material forming a shell around the interior which still had largely intact pores—suggested by the almost unchanged morphologies of the particle interiors shown by the SEM images. However, the loss of peaks in the XRD patterns of the UiO-66 (e.g., after 330 min time on stream, Table 2.1) provides evidence that the interior structures of the MOF particles had become amorphous, weighing against complete blocking of the pore mouths. Thus, we hypothesize that as the catalytic reaction proceeded, the exterior regions of the particles became increasingly amorphized, limiting access of methanol to the MOF interior, but not shutting it off completely, so that node–linker bond breaking continued there. And recall that some deactivation could have resulted from blocking of node catalytic sites by methoxy ligands.

Further work is required to understand how these and other MOFs catalysts reach their demise. The processes are complex, and it is a MOF synthesis challenge to prepare samples with systematically varied structures and compositions to allow resolution of the competing effects.

Implications of this Work for Practical Catalysis by MOFs. It is evident from the results presented here that the life history of UiO-66 and, by inference, other MOFs as catalysts is markedly different from the life histories of common inorganic solid catalysts such as metal oxides and zeolites. The organic constituents of the MOFs render them susceptible to deactivation processes that are unique and complex, some associated with node–linker bonds. The processes include breaking of these bonds by both physical processes (such as grinding and sample handling causing abrasion) and by chemical processes such as the alcohol-induced unzipping and inhibition by reaction products. Numerous reactants in addition to alcohols that react with node–linker bonds are also expected to cause such unzipping.

There is still a lack of practical applications of MOFs as catalysts, and the stability limitations likely account for this lack. We emphasize that temperatures of roughly 550 K may represent the upper stability limit of MOFs such as those in the UiO family (which are among the most robust known) and that this limit depends on the reactive environment. We might speculate that MOFs will find specialty applications as catalysts when tailoring of the catalytic sites is crucial (perhaps for high selectivity); when long catalyst lifetimes and regenerability are not essential; and when reactants and products do not react with the MOFs to unravel them.

The tactics implemented in this work may be of some general value in guiding the assessment of MOFs and their strengths and limitations as practical catalysts. We suggest that future assessments of the best methods for evaluating reticular materials such as MOFs may go beyond recent assessments[26] and include methods such as those reported here for evaluating stabilities in potential long-term applications.

CONCLUSIONS

The results presented here provide a picture of how particles of a MOF (UiO-66) with Zr_6O_8 nodes underwent marked changes in composition and structure as it functioned as a methanol dehydration catalyst in a flow reactor. The catalyst was activated as adventitious formate and acetate ligands on the nodes (formed in the syntheses) were removed by reaction with methanol, freeing catalytic sites. Simultaneously, the catalyst was deactivated, ultimately reaching its demise, as methanol reacted with node–linker bonds to unzip the MOF structure, creating ill-defined amorphous material, especially near the outer particle surfaces, and somehow shutting down catalysis, possibly by limiting access of the methanol to the interior particle space.

REFERENCES

(1) Furukawa, H.; Cordova, K. E.; O'Keefe, M.; Yaghi, O. M. The Chemistry and Applications of Metal-Organic Frameworks. *Science* **2013**, 341, 123044.

(2) Choi, S.; Drese, J. H.; Jones, C. W. Adsorbent Materials for Carbon Dioxide Capture from Large Anthropogenic Point Sources. *ChemSusChem*: Chemistry & Sustainability Energy & Materials **2009**, 2, 796–854.

(3) Chavan, S.; Vitillo, J. G.; Gianolio, D.; Zavorotynska, O.; Civalleri, B.; Jakobsen, S.; Nilsen, M. H.; Valenzano, L.; Lamberti, C.; Lillerud, K. P.; Bordiga, S. H2 Storage in Isostructural UiO-67 and UiO-66 MOFs. *Phys. Chem. Chem. Phys*. **2012**, 14, 1614–1626.

(4) Yang, D.; Gates, B. C. Catalysis by Metal Organic Frameworks: Perspective and Suggestions for Future Research. *ACS Catal.* **2019**, 9, 1779–1798.

(5) Lee, J.; Farha, O. K.; Roberts, J.; Scheidt, K. A.; Nguyen, S. T.; Hupp, J. T. Metal–Organic Framework Materials as Catalysts. *Chem. Soc. Rev.* **2009**, 38, 1450–1459.

(6) Guo, J.; Qin, Y.; Zhu, Y.; Zhang, X.; Long, C.; Zhao, M. Metal–organic frameworks as catalytic selectivity regulators for organic transformations. *Chem. Soc. Rev.* **2021**, 50, 5366–5396.

(7) Opanasenko, M.; Dhakshinamoorthy, A.; Čejka, J.; Garcia, H. Deactivation Pathways of the Catalytic Activity of Metal-Organic Frameworks in Condensation Reactions. *ChemCatChem* **2013**, 5, 1553–1561.

(8) Yang, D.; Ortuño, M. A.; Bernales, V.; Cramer, C. J.; Gagliardi, L.; Gates, B. C. Structure and Dynamics of Zr 6 O 8 Metal–Organic Framework Node Surfaces Probed with Ethanol Dehydration as a Catalytic Test Reaction. *J. Am. Chem. Soc.* **2018**, 140, 3751–3759.

(9) Yang, R. A.; Sarazen, M. L. Reaction Pathways and Deactivation Mechanisms of Isostructural Cr and Fe MIL-101 during Liquid-Phase Styrene Oxidation by Hydrogen Peroxide. *Catal. Sci. Technol.* **2021**, 11, 5282–5296.

(10) Cavka, J. H.; Jakobsen, S.; Olsbye, U.; Guillou, N.; Lamberti, C.; Bordiga, S.; Lillerud, K. P. A New Zirconium Inorganic Building Brick Forming Metal Organic Frameworks with Exceptional Stability. *J. Am. Chem. Soc.* **2008**, 130, 13850–13851.

(11) Kandiah, M.; Nilsen, M. H.; Usseglio, S.; Jakobsen, S.; Olsbye, U.; Tilset, M.; Larabi, C.; Quadrelli, E. A.; Bonino, F.; Lillerud, K. P. Synthesis and Stability of Tagged UiO-66 Zr-MOFs. *Chem. Mater.* **2010**, 22, 6632–6640.

(12) Valenzano, L.; Civalleri, B.; Chavan, S.; Bordiga, S.; Nilsen, M. H.; Jakobsen, S.; Lillerud, K. P.; Lamberti, C. Disclosing the Complex Structure of UiO-66 Metal Organic Framework: A Synergic Combination of Experiment and Theory. *Chem. Mater.* **2011**, 23, 1700–1718.

(13) Howarth, A. J.; Liu, Y.; Li, P.; Li, Z.; Wang, T. C.; Hupp, J. T.; Farha, O. K. Chemical, Thermal and Mechanical Stabilities of Metal–Organic Frameworks. *Nat. Rev. Mater.* **2016**, 1, 15018.

(14) Yang, D.; Gates, B. C. Elucidating and Tuning Catalytic Sites on Zirconium- and Aluminum-Containing Nodes of Stable Metal–Organic Frameworks. *Acc. Chem. Res.* **2021**, 54, 1982–1991.

(15) Wei, R.; Gaggioli, C. A.; Li, G.; Islamoglu, T.; Zhang, Z.; Yu, P.; Farha, O. K.; Cramer, C. J.; Gagliardi, L.; Yang, D.; Gates, B. C. Tuning the Properties of Zr6O8 Nodes in the Metal-Organic Framework UiO-66 by Selection of Node-Bound Ligands and Linkers. *Chem. Mater.* **2019**, 31, 1655–1663.

(16) Shearer, G. C.; Chavan, S.; Bordiga, S.; Svelle, S.; Olsbye, U.; Lillerud, K. P. Defect Engineering: Tuning the Porosity and Composition of the Metal–Organic Framework UiO-66 via Modulated Synthesis. *Chem. Mater.* **2016**, 28, 3749–3761.

(17) Atzori, C.; Shearer, G. C.; Maschio, L.; Civalleri, B.; Bonino, F.; Lamberti, C.; Svelle, S.; Lillerud, K. P.; Bordiga, S. Effect of Benzoic Acid as a Modulator in the Structure of UiO-66: An Experimental and Computational Study. *J. Phys. Chem.* **2017**, 121, 9312–9324.

(18) Katz, M. J.; Brown, Z. J.; Colón, Y. J.; Siu, P. W.; Scheidt, K. A.; Snurr, R. Q.; Hupp, J. T.; Farha, O. K. A Facile Synthesis of UiO-66, UiO-67 and Their Derivatives. *Chem. Comm.* **2013**, 49, 9449–9451.

(19) Yang, D.; Gaggioli, C. A.; Ray, D.; Babucci, M.; Gagliardi, L.; Gates, B. C. Tuning Catalytic Sites on Zr6O8 Metal–Organic Framework Nodes via Ligand and Defect Chemistry Probed with tert-Butyl Alcohol Dehydration to Isobutylene. *J. Am. Chem. Soc.* **2020**, 142, 8044–8056.

(20) Schaate, A.; Roy, P.; Godt, A.; Lippke, J.; Waltz, F.; Wiebcke, M.; Behrens, P. Modulated Synthesis of Zr-Based Metal-Organic Frameworks: From Nano to Single Crystals. *Chem. Eur. J.* **2011**, 17, 6643–6651.

(21) Liu, N.; Shi, L.; Meng, X. Tuning the Adsorption Properties of UiO-66 via Acetic Acid Modulation. *J. Chem. Sci.* **2019**, 131, 50.

(22) Morris, W.; Wang, S.; Cho, D.; Auyeung, E.; Li, P.; Farha, O. K.; Mirkin, C. A. Role of Modulators in Controlling the Colloidal Stability and Polydispersity of the UiO-66 Metal–Organic Framework. *ACS Appl. Mater. Interf.* **2017**, 9, 33413–33418.

(23) Wang, Z.; Babucci, M.; Zhang, Y.; Wen, Y.; Peng, L.; Yang, B.; Gates, B. C.; Yang, D. Dialing in Catalytic Sites on Metal Organic Framework Nodes: MIL-53(Al) and MIL-68(Al) Probed with Methanol Dehydration Catalysis. *ACS Appl. Mater. Interf.* **2020**, 12, 53537–53546.

(24) Zhuang, S.; Huang, H.; Xiao, Y.; Zhang, Z.; Tang, J.; Gates, B. C.; Yang, D. Pair Sites on Al3O Nodes of the Metal-Organic Framework MIL-100: Cooperative Roles of Defect and Structural Vacancy Sites in Methanol Dehydration *Catalysis. J. Catal.* **2021**, 404, 128–138.

(25) Su, Z.; Miao, Y.-R.; Zhang, G.; Miller, J. T.; Suslick, K. S. Bond Breakage under Pressure in a Metal Organic Framework. *Chem. Sci.* **2017**, 8, 8004–8011.

(26) Gropp, C.; Canossa, S.; Wuttke, S.; Gándara, F.; Li, Q.; Gagliardi, L.; Yaghi, O. M. Standard Practices of Reticular Chemistry. *ACS Cent. Sci.* **2020**, 6, 1255–1273.

CHAPTER THREE

Characterization of the MOF UiO-66 under conditions of catalysis of isopropanol dehydration.

ABSTRACT: The life cycle of a metal-organic framework (MOF) catalyst, UiO-66, which incorporates Zr_6O_8 nodes and 1,4-benzene dicarboxylate linkers and is known for its stability, was investigated with isopropanol dehydration as a test reaction. Selectivity of isopropanol dehydration reactions are excellent probes of the catalytic sites as the two products, diisopropyl ether and propylene, depend on the type and distribution of active sites. Catalyst performance was determined with a once-through flow reactor at atmospheric pressure and temperatures of 510–548 K. The products were analyzed by on-line gas chromatography, and catalyst samples removed from the reactor after various times on stream were characterized by X-ray diffraction crystallography, surface area measurements, scanning electron microscopy, and ^{1}H NMR spectroscopy of samples digested in NaOH characterizing the collapse of the MOF structure and deactivation of the catalyst, reaching steady state at low conversions, < 1.5 %, after times on stream of 3–5 h, depending on the initial MOF composition. Increases in the amount of acetic acid modulator in the initial MOF compositions were found cause increases in the selectivity of diisopropyl ether. Furthermore, exposure to reaction conditions led to loss in diisopropyl ether selectivity and is correlated with the amorphization of the outer shell of the MOF structure. The pathway by which the selectivity changed with deactivation of the catalyst was shown to be complex and to differ between the initial compositions of the MOF. The tactics implemented in this work are suggested to be of value for assessing the strengths and limitations of MOFs as practical catalysts.

INTRODUCTION

The literature of metal-organic frameworks (MOFs)—porous, crystalline materials consisting of inorganic nodes and organic linkers (struts)—has evolved beyond a discovery stage emphasizing synthesis and structure determination, typically by X-ray diffraction crystallography (XRD) and surface area/pore volume measurements.

Applications[1–6] and motivations[7–9] for the investigation of UiO-66 stated in Chapter 2 pertain as well to this chapter, Chapter 3, with the work summarized in this chapter having been done with the same methods reported in Chapter 2. This chapter is focused on an investigation of the MOF catalyst performance, including evidence of the selectivity of the catalyst for propylene vs diisopropyl ether, the two products of the dehydration of isopropanol. The focus on catalytic selectivity in MOFs has been primarily on the regioselectivity, chemistry of the confining pores, and modification by exchanging the metal atoms of the MOF nodes to change Lewis acid properties.[6] However there has been an absence of investigations reporting how MOFs change in selectivity with exposure to reaction conditions as they begin to unravel.

Again, we chose the widely investigated, well-characterized MOF known for its robustness (UiO-66)[10–13], which incorporates Zr_6O_8 nodes that offer sites for acid-base-catalyzed reactions such as those occurring on metal oxides and zeolites.[14] The MOFs were synthesized with a modulator (acetic acid) present in various concentrations to provide a family of samples with various node ligand compositions, including acetate and foramte.[15–18] Ligand removal from MOF nodes has been documented and characterized with ^{1}H NMR spectroscopy that records the loss of organic ligands after exposure to alcohol dehydration reaction conditions. Infrared spectroscopy has provided complementary information showing the loss of these ligands and adsorption of alcohol dehydration reaction intermediates.[19] However, the interactions of ligand removal from active sites has only been investigated with a few alcohols, and preliminary evidence suggests that these sites are readily replaced by reactant species and inhibitors.

We chose isopropanol dehydration as the catalytic test reaction because it has the advantages of being stoichiometrically simple and taking place under mild conditions, providing opportunities for investigation with a flow reactor fed with isopropanol as a vapor-phase reactant and for determining how the selectivity depends on catalyst structure and composition. The selectivity for alcohol dehydration on UiO-66, and similar MOFs, has been investigated with computational chemistry and infrared spectroscopy, leading to postulates of energetically likely mechanisms.[8,20] However, acquisition of further evidence of these suggested mechanisms, analogous to those inferred for zeolites[21,22] and bulk metal oxides[23], has been complicated by the lack of resolution of the mass transfer limitations and chemical instability of the MOFs. Thus, an understanding of catalyst selectivity in alcohol dehydration reactions catalyzed by MOFs is lacking. Conclusions drawn from data characterizing other catalysts, such as zeolites and alumina, do not pertain to MOFs. The mechanisms of isopropanol dehydration catalyzed by MOFs may also be further complicated by the product water, which is expected to inhibit catalysis by bonding to active sites and possibly by changing the MOF structure under reaction conditions.

Thus, an investigation of isopropanol dehydration is a good opportunity for understanding the nature of defect sites of the UiO-66 family nodes. The initial selectivity, its relationship to the amount of acid modulation in synthesis, and the changes in selectivity over time following exposure to reaction conditions will contribute to the understanding of the mechanism for alcohol dehydration of these MOFs.

Our tactics were to characterize MOF samples after various times on stream to assess changes in their properties occurring during operation as catalysts and to relate these changes to changes in catalyst performance. The samples were characterized with PXRD, Brunauer-Emmett-Teller (BET) surface area measurements, scanning electron microscopy (SEM), and ^{1}H NMR spectroscopy of digested samples that quantify the organic components. The results demonstrate how the MOF node ligands acetate and formate, which arise in the syntheses, are catalytic reaction inhibitors; how the catalyst is activated by removal of these inhibitors by reaction with isopropanol to form isopropyl formate and isopropyl acetate that desorb; and how the catalyst undergoes deactivation and changes in selectivity as isopropanol reacts to form inhibitor isopropoxy ligands on the nodes and to break node–linker bonds, unzipping the crystalline structure and causing the demise of the catalyst even while the catalyst particles still seem to be largely intact.

EXPERIMENTAL METHODS

The experimental methods were mostly identical to those reported in Chapter 2, with the same syntheses of UiO-66aa6, UiO-66aa30, and UiO-66aa100 and characterization with PXRD, SEM, BET, ^{1}H NMR spectroscopy, and catalytic reaction experiments in flow reactors. The notable difference was in the catalytic reactor experiments with a sparger used to control the composition of the reactor feed containing isopropanol. The feed partial pressures were 80 mbar of isopropanol (HPLC Grade 99.9%, Sigma Aldrich), determined by the vapor pressure of isopropanol in the temperature-controlled sparger at 303 K, and 920 mbar of helium, with the total feed flow rate being 12.5 mL (NTP)/min. The other notable difference was that all experiments were completed with a single batch of MOF synthesis in this work.

RESULTS

MOFs Synthesized with Various Node Ligand Compositions. The MOF syntheses, under conditions summarized in Table 3.1, were characterized by good reproducibility. Only single batches of the MOFs were made because single batches gave sufficient yields for all the planned experiments. A comparison to literature values and an explanation of the characterization of the initial UiO-66 MOFs are provided in Chapter 2 (see Table A2.1 and A2.2 in the Appendix for literature comparison of the as-synthesized MOFs).

Table 3.2. Properties of UiO-66 Catalysts Synthesized with various Acetic Acid Modulator/$ZrCl_4$ Ratios.

MOF	molar ratio of modulator/ $ZrCl_4$ in synthesis	time on stream (min)	area of prominent peak in XRD pattern (a.u.)	BET surface area (m^2/g)	average MOF particle diameter (nm)	percentage of node ligands to which formate is bonded[a,c]	percentage of node ligands to which acetate is bonded	percentage of node ligands to which linker derived from 1,4-BDC is bonded	percentage of node ligands to which propoxy is bonded
UiO-66aa6	6	0	N/A	1530 ± 1.5	130 ± 20	4 ± 1	3 ± 1	90 ± 5	0
UiO-66aa6 mixed with α-Al_2O_3 particles[b]	6	0	0.017	24 ± 1.5	140 ± 15	6 ± 1	5 ± 1	90 ± 5	0
		45	0.011	19 ± 1.5	150 ± 15	0	0	80 ± 10	20 ± 10
		150	0.0056	-	130 ± 15	0	0	80 ± 10	20 ± 10
		330	0	10 ± 1.5	120 ± 15	0	0	70 ± 10	30 ± 10
		1000	0	6 ± 1.5	100 ± 10	0	0	60 ± 10	40 ± 10
UiO-66aa30	30	0	N/A	1382 ± 1.5	190 ± 27	4 ± 1	12 ± 1	85 ± 5	0
UiO-66aa30 mixed with α-Al_2O_3 particles	30	0	0.042	25 ± 1.5	210 ± 39	4 ± 1	11 ± 1	85 ± 5	0
		45	0.021	12 ± 1.5	170 ± 25	0	0.5	90 ± 10	10 ± 10
		150	0.0035	13 ± 1.5	155 ± 20	0	0.3	70 ± 10	30 ± 10
		330	0.00086	6 ± 1.5	130 ± 15			50 ± 10	50 ± 10
		1000	0.00040	5 ± 1.5	120 ± 15			50 ± 10	50 ± 10
UiO-66aa100	100	0	N/A	1629 ± 1.5	350 ± 30	3 ± 1	14 ± 1	80 ± 5	0
UiO-66aa100 mixed with α-Al_2O_3 particles	100	0	0.078	27 ± 1.5	380 ± 30	4 ± 1	13 ± 1	80 ± 5	0
		45	0.0056	16 ± 1.5	290 ± 30	0	0	70 ± 10	30 ± 10

		150	0.0097	10 ± 1.5	280 ± 40	0	0	70 ± 10	30 ± 10
		330	0	6 ± 1.5	240 ± 25	0	0	70 ± 10	30 ± 10
		1000	0		210 ± 30	0	0	60 ± 10	40 ± 10

[a] The percentage of the node ligands to which formate was bonded was calculated by: $n_{\text{formate}}/(n_{\text{formate}} + n_{\text{acetate}} + 2 \times n_{\text{terephthalate}} + n_{\text{isopropoxy}})$, where n is the number of mols; a comparable statement pertains to acetate, and it was assumed that the linker 1,4-benzenedicarboxylate was a bidentate ligand. [b] MOF particles were mixed with α-Al_2O_3 particles in a mass ratio of 1:40. [c] Errors were determined from the repeat conversion vs. time on stream data and represent variations in the mass of UiO-66 from run to run and are the basis for the error bounds shown here.

Catalyst Performance Data Demonstrating the Life Cycle of UiO-66 in Isopropanol Dehydration Reactions. Isopropanol conversion was negligible in the absence of catalyst under our conditions. When MOF particles were present in the reactor, the main reaction of isopropanol dehydration to give propylene took place along with the dehydration to give diisopropyl ether:

$$C_3H_7OH \rightarrow C_6H_6 + H_2O \tag{3.1}$$

$$2C_3H_7OH \rightarrow C_6H_{14}O + H_2O \tag{3.2}$$

Because an FID detector was used, water was not observed in the chromatograms. Conversions and selectivities were determined from the propylene, diisopropyl ether, and isopropanol peak areas. Because the conversions were differential, with conversions typically < 10 %, the catalyst performance data are reported as reaction rates per unit mass of catalyst. Isopropyl formate and isopropyl acetate were observed in the chromatograms, consistent with expectation[8,14,15,20] and with ^{1}H NMR data demonstrating the presence of acetate and formate in the as-synthesized MOFs (Figure A3.1 and A3.2 in the Appendix). However, quantification of the isopropyl acetate was not possible with the column conditions as the retention time of this compound was the same as that of diisopropyl ether (these compounds have similar structures and molar masses of 102.18 and 102.13 g mol^{-1}). Peaks of isopropanol, diisopropyl ether, isopropyl formate, and isopropyl acetate were confirmed with stock solutions flowing to the gas chromatograph under conditions controlled with the sparger temperature (Figures A3.1 and A3.2 in the Appendix).

In other alcohol dehydration reactions[8,14,20] catalyzed by MOFs with Zr_6O_8 or other metal oxide cluster nodes,[24,25] analogous esters have been observed to be desorbed from the catalyst, evidently formed as the alcohol reacted with the node carboxylate ligands and are accompanied by complementary evidence of the loss of the inhibiting ligands in ^{1}H NMR data, as observed this work.

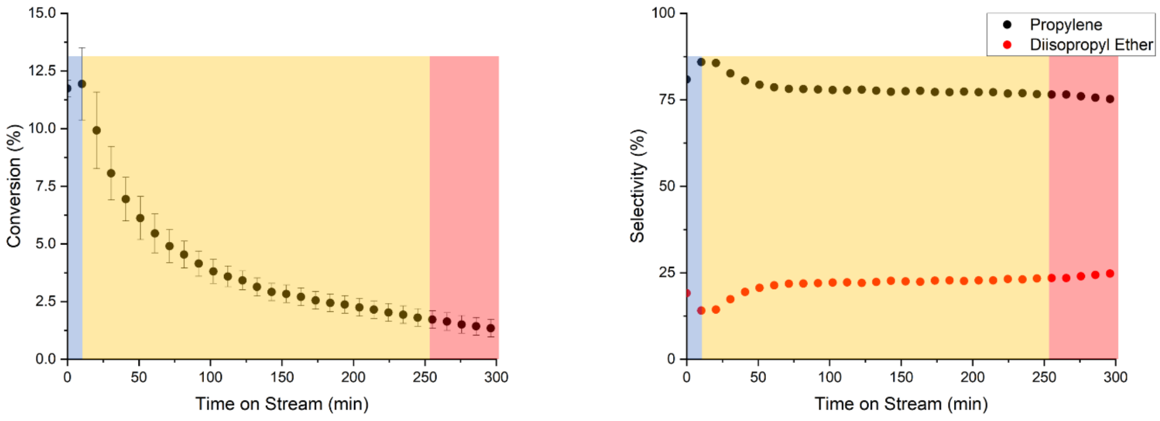

Figure 3.1. Isopropanol dehydration catalyzed by UiO-66aa30 in a flow reactor: evidence of stages of MOF catalyst performance, left. Selectivity for propylene (black) and diisopropyl ether (red) with the three stages represented, right. Reaction conditions: 548 K, feed partial pressure, 80 mbar of isopropanol and 920 mbar of helium; total feed flow rate, 12.5 mL(NTP)/min; catalyst mass, 25 mg of MOF and 1.00 g of α-Al_2O_3. The MOF catalyst life cycle includes an activation stage during which the conversion proceeds to a maximum (blue) followed by a deactivation stage (yellow-brown) that leads to the nearly complete loss of catalytic activity (red). Error bars are precisions determined in repeat experiments. The most significant sources of error are associated with losses in sample during preparation/handling and inconsistencies in the product analyses by GC.

Catalyst performance data demonstrating the life cycle of UiO-66 in isopropanol dehydration are characterized by three regions (Figure 3.1):

1) Activation: During typically the first 15 min on stream, the conversion of isopropanol increased along with changes in selectivity that are more clearly observable at lower temperatures.
2) Deactivation: Thereafter, the conversion declined along with slower changes in propylene selectivity compared to the activation stage. In the analysis that follows, it is shown that

deactivation was taking place from time zero on stream. Initial rates of deactivation were determined by extrapolating the conversion-time on stream data following the activation stage to zero time on stream to deconvolute the data and resolve the activation and deactivation phenomena.

3) Demise: When experiments were conducted long enough, the isopropanol conversion approaches steady state at low conversions (< 1.5%). The conversion stayed at ~1% conversion even after several days (Figure A3.3)

To characterize changes in the MOF properties during these stages, samples (in separate experiments, each beginning with unused catalyst) were removed from the reactor after various times on stream: 45, 150, 330, and approximately 1000 min (Figure 3.2).

Catalyst Activation by Removal of Isopropyl Acetate and Isopropyl Formate. In catalysis experiments carried out at 510 K, UiO-66aa6 and UiO-66aa30 underwent activation slowly enough to observe clearly (Figure 3.3A), but under some conditions the activation period was too short to characterize well (e.g., Figure A3.4 in the Appendix). GC evidence of isopropyl formate in the product stream was obtained during the activation periods. As shown in Figure 3.5, the yields of this gas-phase product declined to almost zero by the end of the activation period. ^{1}H NMR spectra of digested samples removed from the reactor after 45 min on stream (Table 3.2) confirm that acetate and formate had been largely removed from the MOFs during catalytic operation. These results show that the formate and acetate ligands on the MOF nodes[14,15,26] were catalytic reaction inhibitors, which implies that the catalytic sites were sites on the nodes.

Catalyst Selectivity for Isopropanol Dehydration During Catalyst Activation. In the catalysis experiments carried out at 510 K, the MOFs underwent a transition in selectivity from 52, 31, and 6.0 % propylene to 85, 80, and 76 % propylene during the first 45 min on stream that characterized the activation period for UiO-66aa6, UiO-66aa30, and UiO-66aa100 respectively (Figure 3.3B). A trend is displayed at 510 K toward higher diisopropyl ether selectivity with MOFs made with a higher acetic acid to zirconium chloride ratio in the synthesis solution.

In catalysis experiments at temperatures higher than 510 K, trends in selectivity with time on stream become less obvious (Figure 3.4). The initial selectivity of UiO-66aa100 shows a trend of increasing initial propylene selectivity with increasing temperature. A similar trend was observed for UiO-66aa30 from temperatures of 510 to 536 K, however between 536 and 548 K the initial propylene selectivity decreased from 87 to 82 %. Initial propylene selectivity for UiO-66aa6 at temperatures above 510 K remained mostly unchanged with the initial and final propylene selectivities of the activation stage being consistently higher than 80 %.

Across all experiments, the final propylene selectivity reached or remained above 75 % by the end of the activation period. The initial selectivity for propylene decreased with increased molar ratio of acetic acid to zirconium chloride used in the synthesis. Additionally, some trends were observed of propylene selectivity increasing with temperature. The influence of temperature and of the acid modulation will be elaborated on in the Discussion.

^{1}H NMR spectra of digested samples removed from the reactor after 45 min on stream (Table 3.2) confirm that acetate and formate had been largely removed from the MOFs during catalytic operation. These results show that removal of the formate and acetate ligands on the MOF nodes[14,15,26] exposed or created sites that were capable of propylene and diisopropyl ether formation. During the first 45 min of reaction, the selectivity of these active sites for propylene reached at least 75%, but the data are complex; see summary above and Figures 3.3 and 3.4. During the operation of the catalysts, substantial changes to the crystallinity, surface area and particle size of the MOFs took place, as characterized with PXRD, BET, and SEM data, shown in the following sections. These structural and chemical changes to the MOFs may be related to the changes in selectivity observed and will be elaborated on in the Discussion.

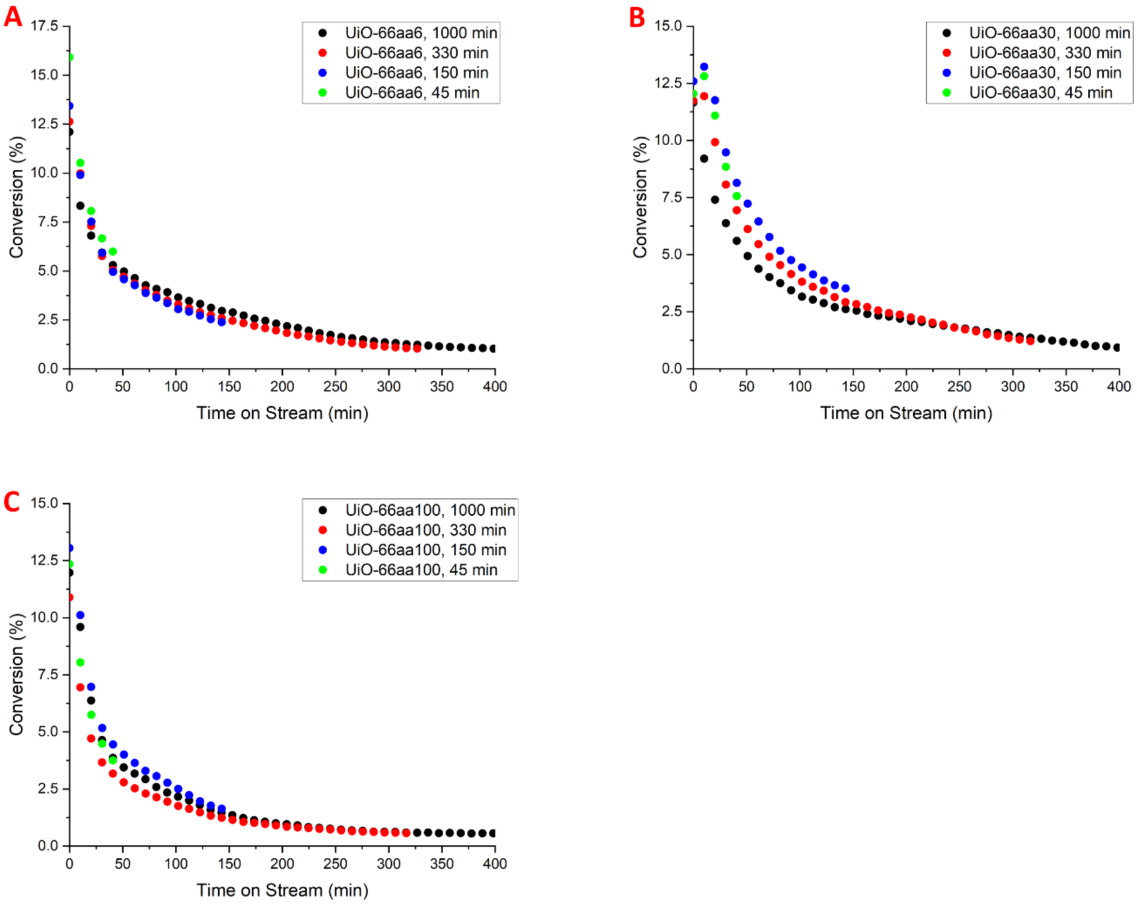

Figure 3.2. Conversion of isopropanol catalyzed by UiO-66aa6 (A), UiO-66aa30 (B), and UiO66aa100 (C) for 45 (green), 150 (blue), 330 (red), and at least 600 min on stream (black). Reaction conditions: 548 K, feed partial pressures: 80 mbar isopropanol and 920 mbar helium; total feed flow rate 12.5 mL (NTP)/min; catalyst mass, 25 mg of MOF particles mixed with 1.00 g of particles of α-Al_2O_3. Comparison with data obtained in separate experiments led to estimates of typical experimental error in conversion.

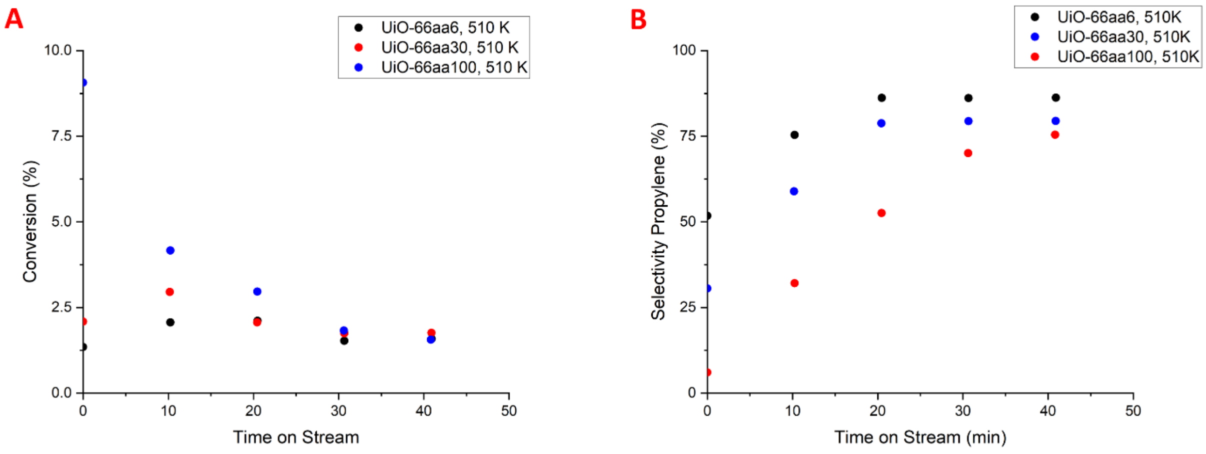

Figure 3.3: Catalyst activation (left) shown by increasing conversion of isopropanol in reaction catalyzed by MOF UiO-66aa6 (black), UiO-66aa30 (red), and UiO-66aa100 (blue). Selectivity for dehydration to propylene over diisopropyl ether (right) for the three MOFs respectively. Reaction conditions: temperature, 510 K; feed partial pressures, 80 mbar of isopropanol and 920 mbar of helium; total feed flow rate 12.5 mL (NTP)/min; catalyst mass, 25 mg of MOF particles mixed with 1.00 g of α-Al_2O_3 particles.

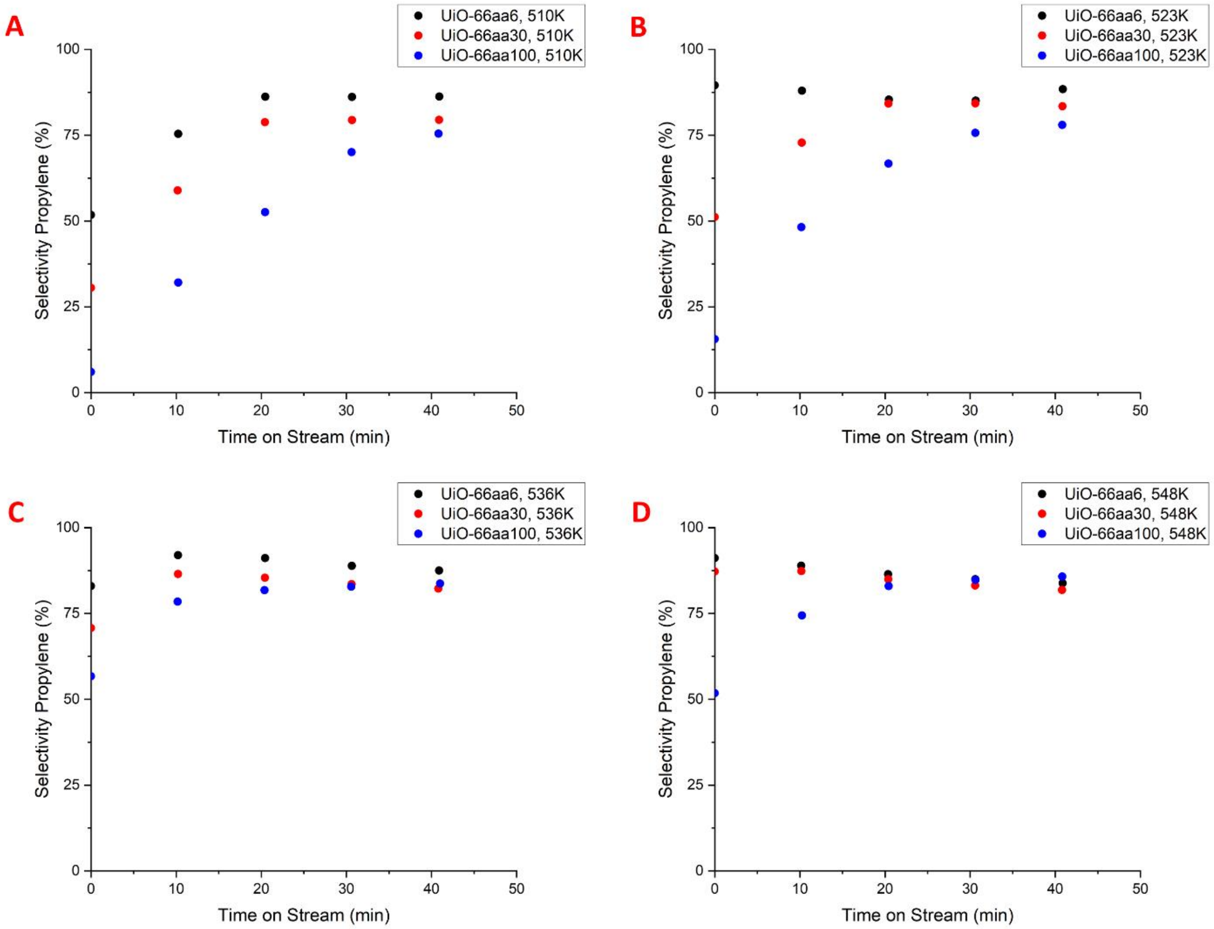

Figure 3.4. Changes in propylene selectivity for UiO-66aa6 (black), UiO-66aa30 (red), and UiO-66aa100 (blue) ranging from 510 (A), 523 (B), 536 (C), and 548 K (D) during the first 45 min on stream. Dehydration of isopropanol catalyzed by UiO-66 gave two dehydration products, propylene and diisopropyl ether, and thus these plots also characterize the changes in diisopropyl ether selectivity. Reaction conditions: temperature, 510 K; feed partial pressures, 80 mbar of isopropanol and 920 mbar of helium; total feed flow rate 12.5 mL (NTP)/min; catalyst mass, 25 mg of MOF particles mixed with 1.00 g of α-Al_2O_3 particles.

Loss of Accessible MOF Surface Area and Changes in MOF Composition During Catalyst Activation. BET surface area measurements show the loss of accessible surface area during the activation period (Table 3.2; the errors are precisions determined in repeat experiments)—note that the areas represent mixtures of the MOF particles with inert alumina particles present in the reactor. Complementary ^{1}H NMR spectra of these samples digested in NaOH show that there were changes in the MOF structure and ligands during the activation period, during which the acetate and formate had been almost completely removed from the MOFs (Table 3.2).

Loss of MOF Crystallinity During Catalyst Activation. Samples taken from the reactor after a clear activation period of 45 min during operation at 548 K were further characterized with PXRD. For proper comparisons, the diffraction patterns of the used catalyst samples were compared with diffraction patters of the unused catalyst samples that were identically mixed with particles of α-Al_2O_3. The comparisons show that the three MOFs lost crystallinity during the activation period, as indicated by the peaks at 2θ = 7.45° and 8.60°; a nearly complete disappearance of these peaks was observed for UiO-66aa100. The data thus show that that changes in the MOF framework structure accompanied the reactions of isopropanol with the node acetate and formate ligands and that the MOF unzipping took place to various degrees that depended on the node ligand composition; broadly, the results are consistent with the inference that reactions of isopropanol with the MOF led to losses of crystallinity.

Table 3.2. Changes in MOF Properties during Activation Period in Isopropanol Dehydration Catalysis.

MOF	surface area of sample consisting of MOF mixed with inert Al_2O_3 particles (m^2/g)		percentage of node ligands to which formate bonded, determined by ^1H NMR spectroscopy		percentage of node ligands to which acetate bonded, determined by ^1H NMR spectroscopy	
	before catalysis	after activation (45 min on stream)	before catalysis	after activation (45 min on stream)	before catalysis	after activation (45 min on stream)
UiO-66aa6	24.0 ± 1.5	19 ± 1.5	6 ± 1	0	5 ± 1	0
UiO-66aa30	25.0 ± 1.5	12 ± 1.5	4 ± 1	0	11 ± 1	0
UiO-66aa100	27.0 ± 1.5	16 ± 1.5	4 ± 1	0	13 ± 1	0

Consistent with this inference, the NMR data (Table 3.1) show that each of the samples UiO66aa6, UiO66aa30, and UiO66aa100 had lost node–linker bonds during the activation period, in agreement with the conclusion that MOF unzipping resulted from the reaction of isopropanol with the node–linker bonds to form isopropyl acetate and isopropyl formate with the linkers. This ester formation, which has been reported for reactions of various alcohols with these and similar node–linker bonds,[8,14,20,24,25] has been shown to lead to the formation of alkoxy ligands on the nodes, and our ^{1}H NMR data confirm the presence of propoxy ligands, showing that the percentage of node ligands to which isopropoxy was bonded after the activation period was approximately 20, 10, and 30 percent, respectively. These data provide clear evidence of MOF disintegration during catalysis—and, we emphasize, even during the initial activation period—thus, it is clear that both activation and deactivation of the MOF catalyst were taking place during the initial stage that we refer to as the activation stage.

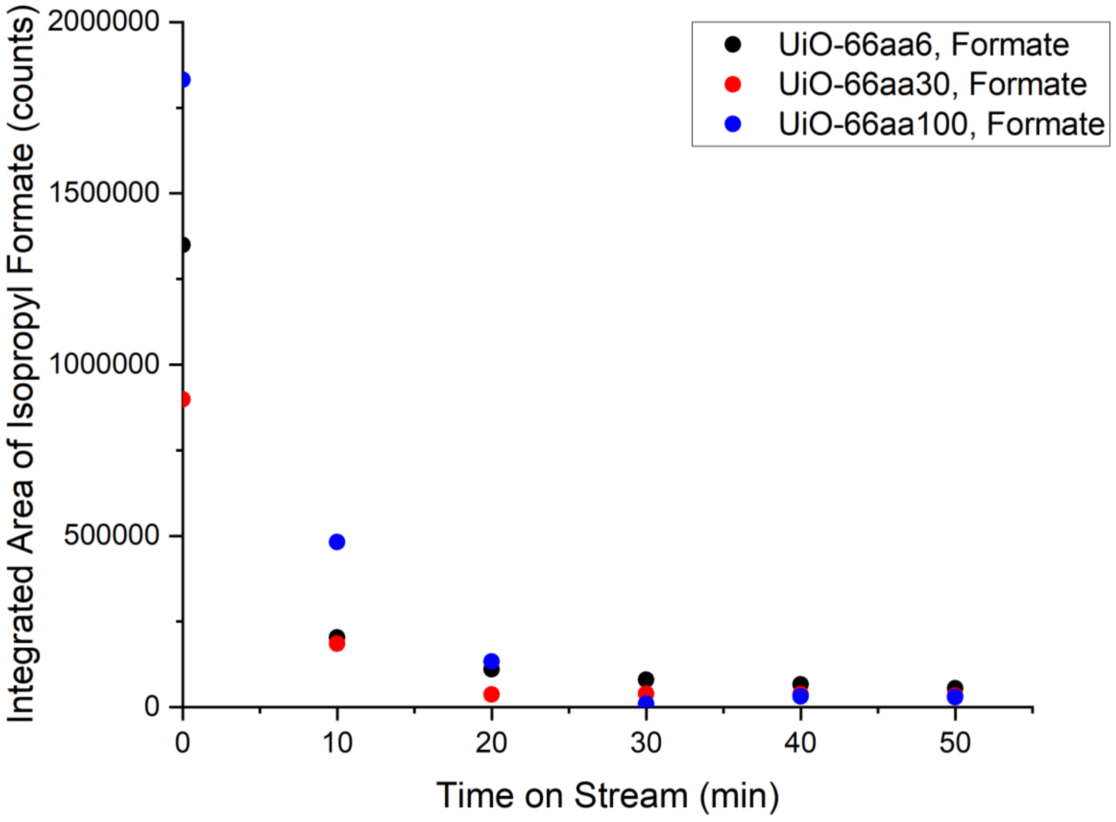

Figure 3.5. Quantitative GC evidence of desorption of isopropyl formate from MOF catalysts during the first 50 min on stream. Reaction conditions: 510 K, feed partial pressures of 80 mbar isopropanol and 920 mbar helium; total flow rate 12.5 mL (NTP)/min; catalyst mass, 25 mg of MOF particles mixed with 1.00 g of α-Al_2O_3 particles.

MOF Catalyst Deactivation and Demise. Following the maximum conversion achieved during the activation period or in cases where no activation of conversion was observed, the catalytic activity of each MOF decreased steadily until it reached < 1.5 % conversion. This stage of the catalytic life cycle is referred to as deactivation, but we reemphasize that the evidence stated above shows that deactivation was occurring even from the beginning—in competition with activation. To characterize the changes in MOF properties following the activation stage, each catalyst in experiments (each of which began with an unused catalyst sample) was removed from the reactor after a period of operation 150, 330, or 1000 min, again by stopping the feed flow, cooling and sealing the reactor, and moving it to the glove box.

At 510 K, each MOF (under the reaction conditions described above) underwent deactivation as shown by the decreases in conversion shown in Figure 3.6.

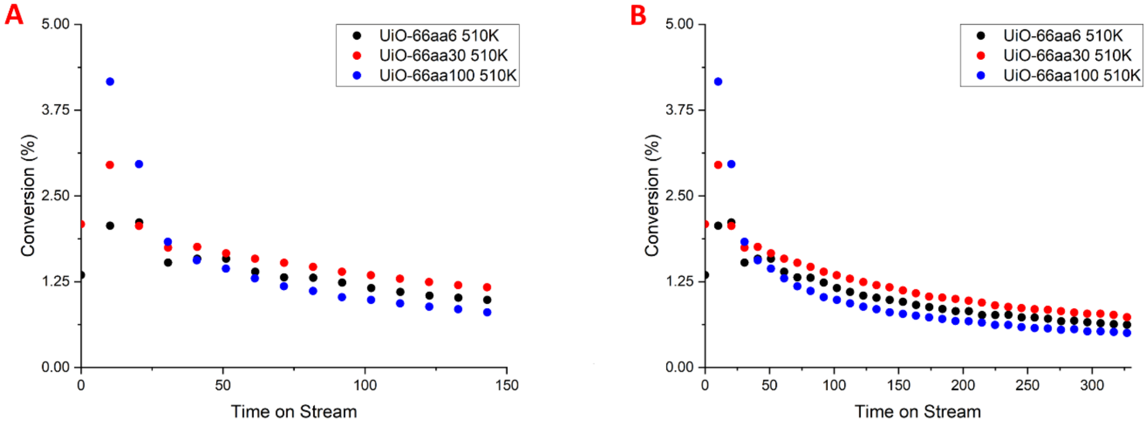

Figure 3.6. MOF catalyst deactivation illustrated for samples of acetic acid-modulated UiO-66, with 6 (black), 30 (red), and 100 (blue) mols of acetic acid per mol of $ZrCl_4$ respectively used in the synthesis, with the catalyst samples removed from the reactor after 150 (left) and 330 min (right). Reaction conditions: 510 K, feed partial pressures: isopropanol, 80, helium, 920 mbar; total flow rate, 12.5 mL (NTP)/min; catalyst mass, 25 mg of MOF particles mixed with 1.00 g of α-Al_2O_3 particles.

Initial reaction rates—that is, the isopropanol dehydration rates characterizing the undeactivated catalysts in the absence of acetate and formate inhibitors—were estimated for each MOF by extrapolating rates determined from differential conversions, of the combined isopropanol dehydration to propylene and diisopropyl ether accounting for the total amount of isopropanol converted, observed during the deactivation stage to zero on-stream time. By this method, using single points, we estimated values for each MOF without the inhibiting ligands. The extrapolation gave estimates of rate values shown in Table 3.3. Table 3.3 also includes initial rates of catalyst activity loss, each determined as the negative of the slope of catalytic reaction rate vs. time on stream, extrapolated to zero time on stream.

Table 3.3. **Rates of Catalytic Reaction and of Catalyst Deactivation extrapolated to pertain to MOFs without Inhibitor Formate and Acetate Ligands**

MOF	temperature (K)	10^4 × rate of catalytic reaction ($mol_{isopropanol\ converted}\ g^{-1}_{MOF}\ min^{-1}$)	10^7 × rate of catalyst deactivation ($mol_{isopropanol\ converted}\ g^{-1}_{MOF}\ min^{-2}$)
UiO-66aa6	548	1.02 ± 0.02	2.2 ± 0.1
	536	0.75 ± 0.01	1.3 ± 0.1
	523	0.57 ± 0.02	0.9 ± 0.1
	510	0.33 ± 0.01	0.51 ± 0.03
UiO-66aa30	548	1.61 ± 0.03	24 ± 1
	536	1.09 ± 0.03	16 ± 1
	523	0.86 ± 0.02	10 ± 1
	510	0.47 ± 0.02	6 ± 1
UiO-66aa100	548	1.91 ± 0.05	56 ± 4
	523	1.27 ± 0.05	27 ± 2
	510	0.71 ± 0.04	14 ± 2

Propylene/Diisopropyl Ether Selectivity: Dependence on Temperature During Catalyst Deactivation and Demise. After the initial increases in propylene selectivity during the activation stage, or lack thereof for UiO-66aa6 and at higher temperatures for UiO-66aa30, the selectivity trends differed between UiO-66aa100 and the other two MOFs (Figure 3.7).

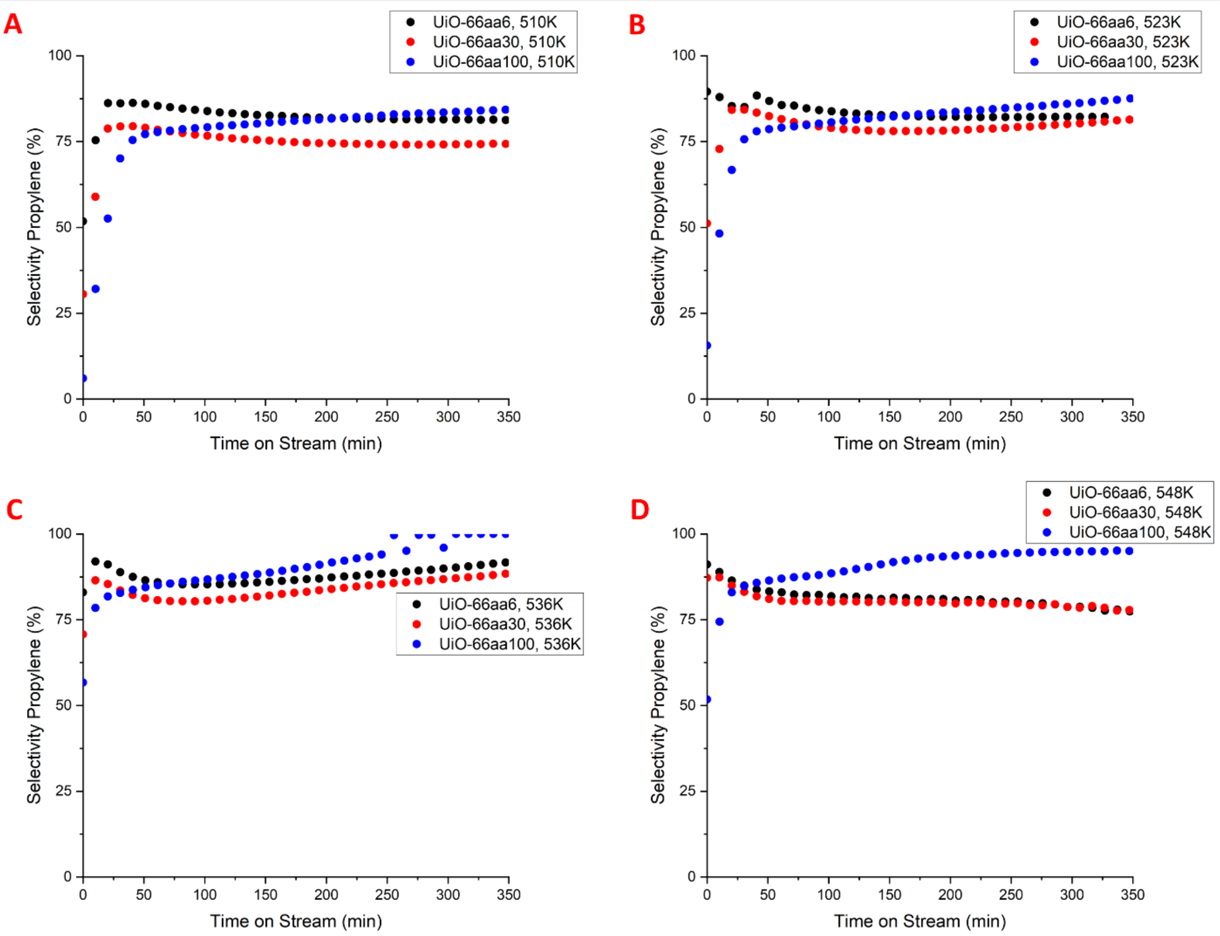

Figure 3.7: The increase in selectivity of propylene for UiO-66aa6 (black), UiO-66aa30 (red), and UiO-66aa100 (blue) ranging from 510 (A), 523 (B), 536 (C), and 548 K (D) during the deactivation of the UiO-66 MOFs. Dehydration of isopropanol over UiO-66 has two products, propylene and diisopropyl ether, and thus these plots also characterize changes in diisopropyl ether selectivity. At 536 K, UiO-66aa100 approaches the detection limit for the GC at higher values of time on stream and results scatter between < 0.5 and 0 % diisopropyl ether selectivity observed at 250 min. Reaction conditions: temperature, 510-548 K; feed partial pressures, 80 mbar of isopropanol and 920 mbar of helium; total feed flow rate 12.5 mL (NTP)/min; catalyst mass, 25 mg of MOF particles mixed with 1.00 g of α-Al_2O_3 particles.

After UiO-66aa100 reaches 75-85% propylene selectivity, characterizing the end of the period of increasing propylene selectivity, a nearly linear increase in propylene selectivity with time on stream toward unity was observed. The selectivity vs. conversion plots show that these trends continue toward a propylene selectivity of 100% at the longest times on stream (Figure 3.8).

At all temperatures investigated, an acceleration of the propylene selectivity is observed at low conversions of UiO-66aa100.

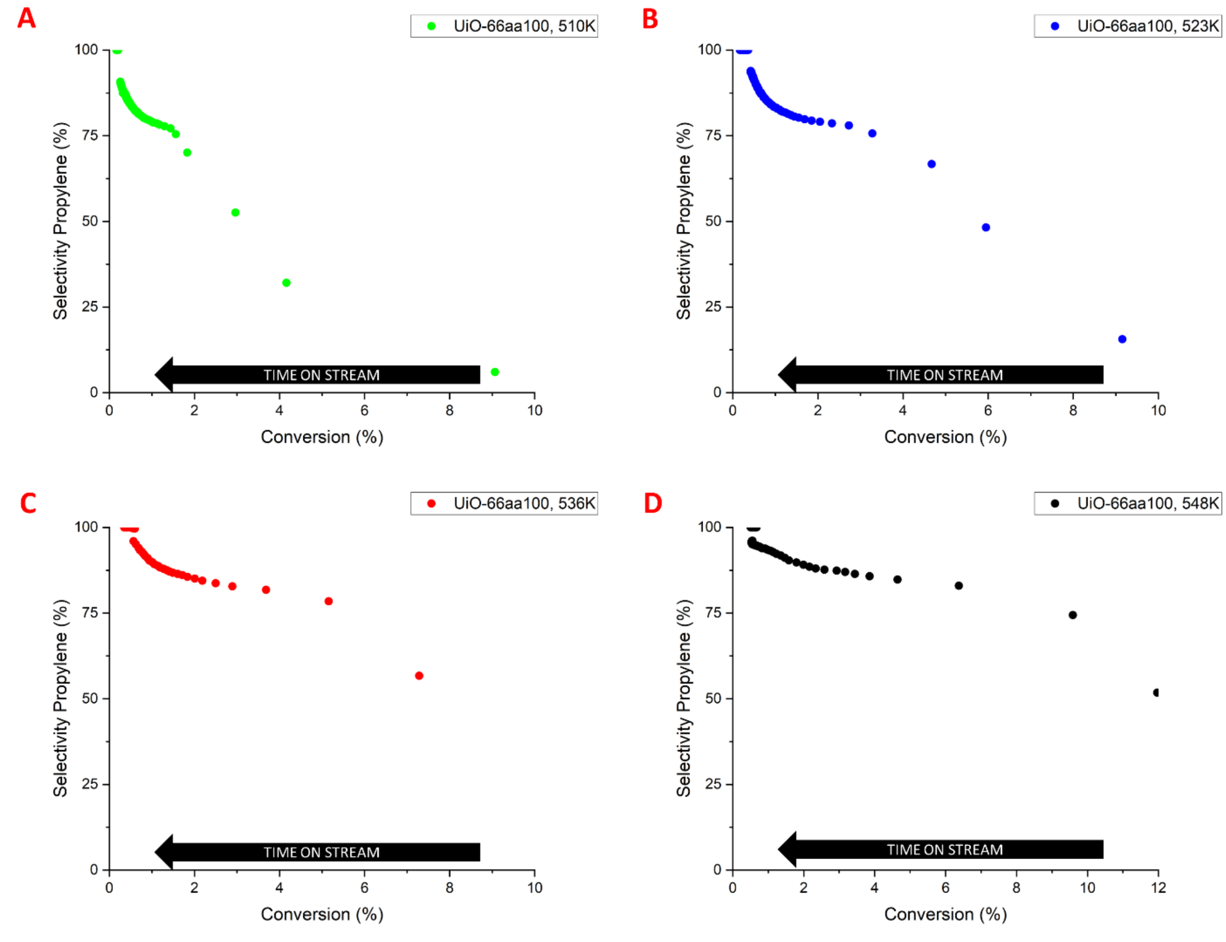

Figure 3.8. Selectivity for propylene formation from isopropanol approaching unity as the conversion approached zero for reaction catalyzed by UiO-66aa100 at 510 (A), 523 (B), 536 (C), and 548 K (D). The arrow at the bottom of each axis shows the direction of time on stream and catalyst deactivation. Abrupt jumps in selectivity at low conversion indicate a limitation of the analysis—there was a loss of signal for the diisopropyl ether peak in the chromatograms because the conversion became too low. Reaction conditions: 510, 523, 536, and 548 K, feed partial pressure of 80 mbar of isopropanol and 920 mbar of helium; total flow rate 12.5 mL (NTP)/ min; catalyst mass, 25 mg of MOF and 1.00 g of α-Al_2O_3 particles mixed with mortar and pestle for 60 s.

Conversely, UiO-66aa6 and UiO-66aa30 are shown to initially decrease in propylene selectivity with time on stream (Figure 3.7, 3.9, and 3.10). Minimum values of propylene selectivity of 81, 82, 85, and 76 % at 350, 180, 100, and 450 min for temperatures of 510, 523, 536, and 548 K are shown for UiO-66aa6. The results are similar to those observed for UiO-66aa30 with minima of propylene selectivity of 74, 78, 80, and 68% at 280, 160, 90, and 680 min for temperatures of 510, 523, 536, and 548 K. Following this minimum, the selectivity for propylene increased toward unity, as was observed with UiO-66aa100. Note that this pattern was not observed in the data for UiO-66aa6 at 510 and 523 K, or for the data characterizing UiO-66aa30 at 548 K because the reaction was not allowed to run long enough. Only the experiments done at 548 K were allowed the full 1000 min of time on stream, as this was the temperature chosen for the structural characterization experiments. Data characterizing UiO-66aa6 at 548 K were obtained for > 3000 min, capturing evidence of the propylene selectivity reaching unity. Although some of the experiments were not run long enough to show the propylene selectivity reaching unity, the data show that the selectivity began to increase as the time on stream increased and the conversion values became lower.

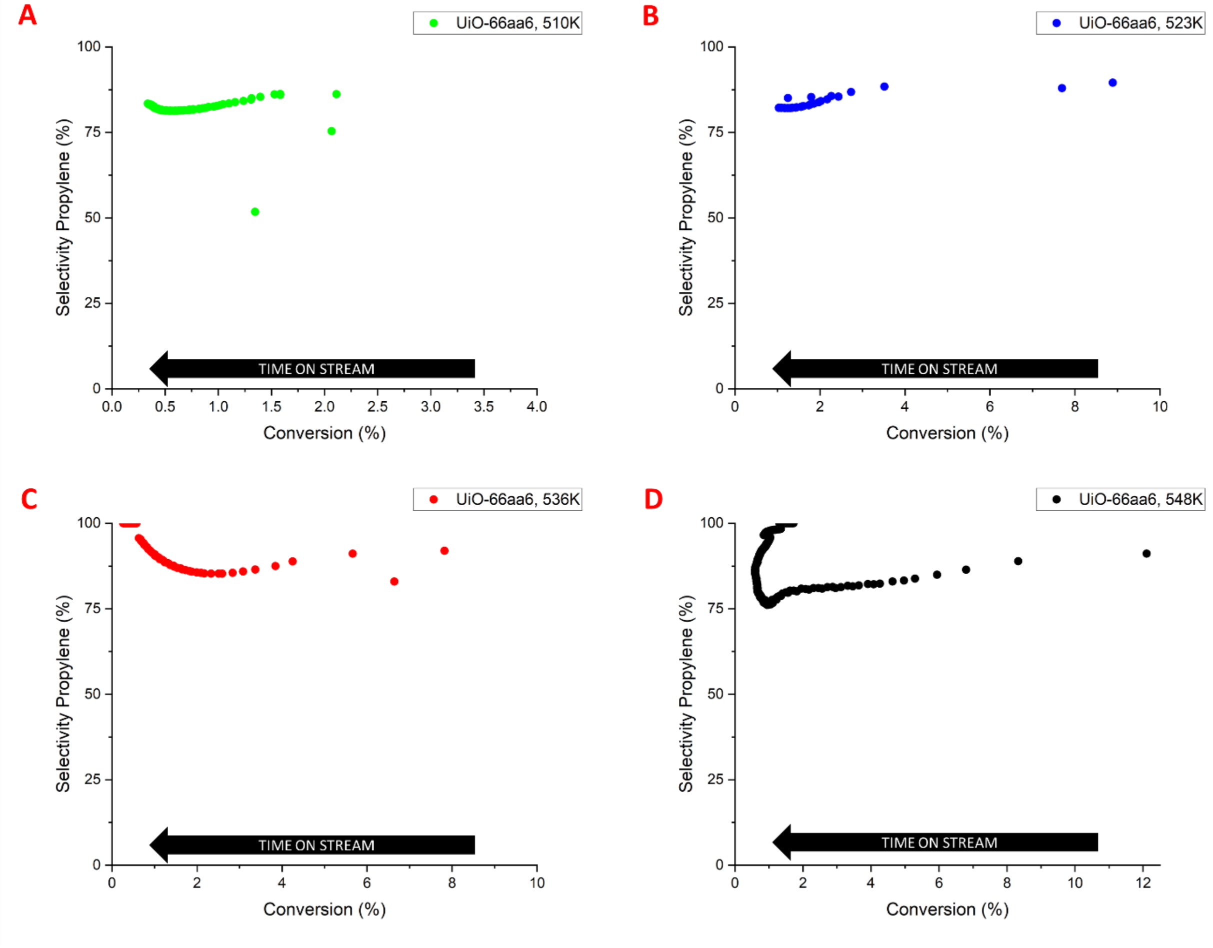

Figure 3.9. Selectivity for propylene approaching unity as the isopropanol conversion approached zero with increasing time on stream observed for UiO-66aa6 at 510 (A), 523 (B), 536 (C), and 548 K (D). Behavior observed at low conversions at 548 K indicates limitations in the GC analyses at the lowest conversions. The arrow at the bottom of each axis shows the direction of time on stream and catalyst deactivation. Abrupt jumps in selectivity at low conversion indicate a limitation of the analysis—there was a loss of signal for the diisopropyl ether peak in the chromatograms because the conversion became too low. Reaction conditions: 510, 523, 536, and 548 K, feed partial pressure of 80 mbar of isopropanol and 920 mbar of helium; total flow rate 12.5 mL (NTP)/ min; catalyst mass, 25 mg of MOF and 1.00 g of α-Al_2O_3 particles mixed with mortar and pestle for 60 s

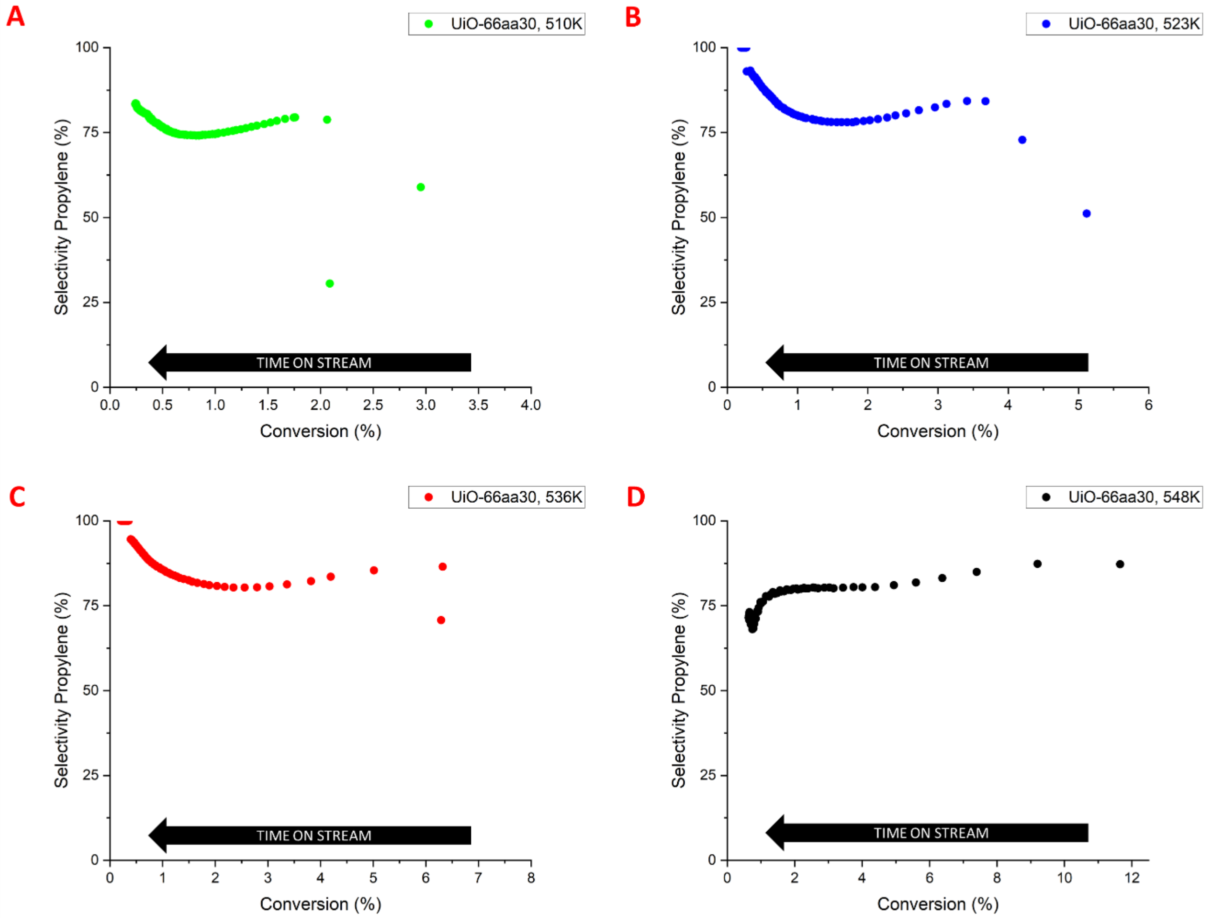

Figure 3.10. Selectivity for propylene approaching unity as the isopropanol conversion approached zero with increasing time on stream observed for UiO-66aa30 at 510 (A), 523 (B), 536 (C), and 548 K (D). The arrow at the bottom of each axis shows the direction of time on stream and catalyst deactivation. Abrupt jumps in selectivity at low conversion indicate a limitation of the analysis—there was a loss of signal for the diisopropyl ether peak in the chromatograms because the conversion became too low. Reaction conditions: 510, 523, 536, and 548 K, feed partial pressure of 80 mbar of isopropanol and 920 mbar of helium; total flow rate 12.5 mL (NTP)/ min; catalyst mass, 25 mg of MOF and 1.00 g of α-Al_2O_3 particles mixed with mortar and pestle for 60 s.

These results indicate that after the activation stage, some sites remained active for the dehydration of isopropanol to diisopropyl ether during the deactivation of the catalysts and approached 100 % propylene selectivity as the conversion approached steady state at < 1 % conversion. Minima of propylene selectivity were observed for UiO-66aa6 and UiO-66aa30, with these minima at longer times on stream and with lower propylene selectivities for UiO-66aa30.

An abrupt change in the trend of the selectivity minima with decreasing time on stream was observed for both of these MOFs at 548 K. The data characterizing UiO-66aa100 had no minima in propylene selectivity. As is shown in the following sections, these changes in selectivity and conversion were accompanied by a significant destruction of the MOF structure. These results are interpreted in the Discussion.

Loss of MOF Crystallinity During Isopropanol Dehydration Catalysis. PXRD patterns of the MOFs (Figure 3.11) show that the peaks characterizing the crystalline material declined during operation. Nearly complete loss of the aforementioned peaks characteristic of UiO-66aa100 was observed even during the activation stage, and no evidence of MOF recrystallization was observed in the deactivated samples. The PXRD patterns show that after 330 min on stream, both UiO-66aa6 and UiO-66aa30 had undergone complete loss of the characteristic peak at $2\theta = 7.45°$. There was essentially no change in the PXRD patterns between this state and the state at which the longest-running sample was removed from the reactor.

Although these samples after 330 min of operation as catalysts had lost essentially all of their crystallinity, as indicated by the PXRD data, the material remained catalytically active. The result implies that the material formed during the degradation, even with node–linker bonds broken and the interior MOF structure markedly changed, was still catalytically active, suggesting that some node surfaces were still accessible and/or that material such as zirconium oxide or zirconium hydroxide had formed. Characterization of these ill-defined materials was beyond the scope of this work.

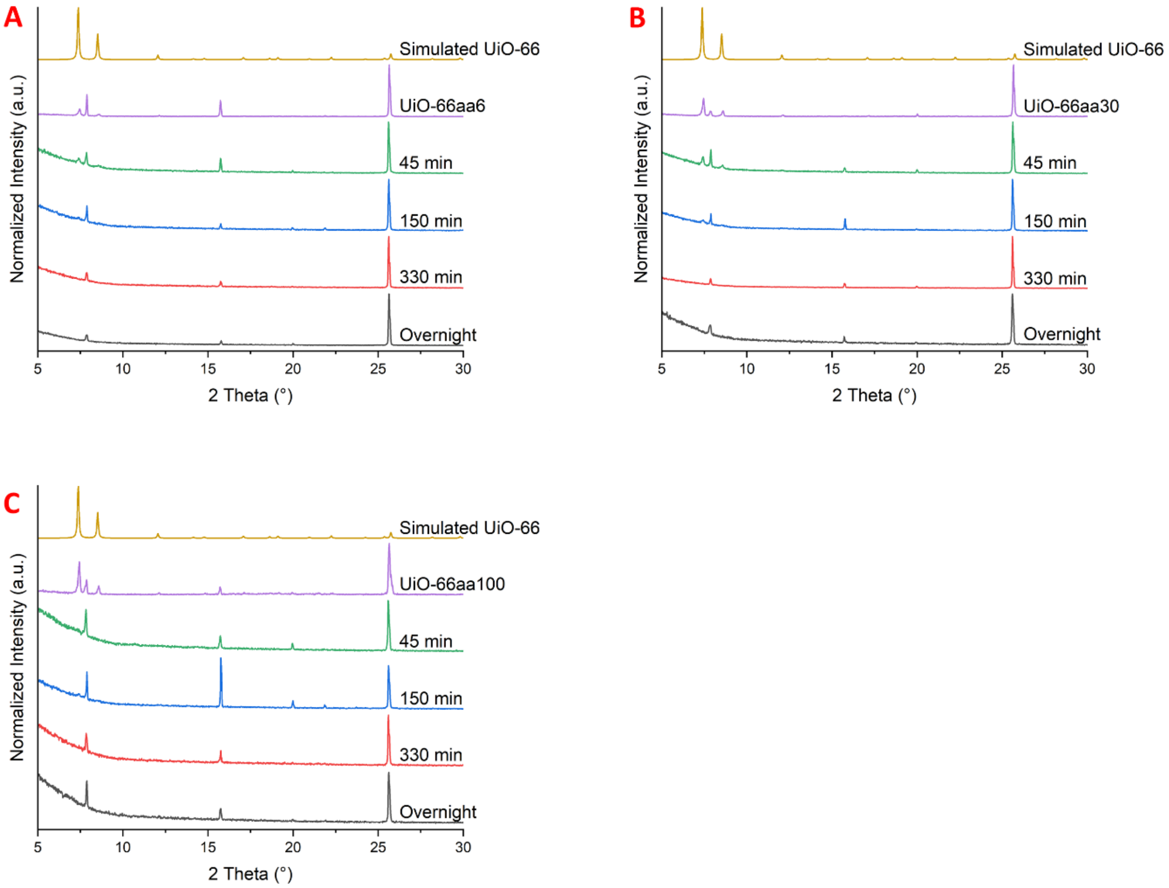

Figure 3.11. Loss of crystallinity of MOF UiO-66aa6 (A), UiO-66aa30 (B), and UiO-66aa100 (C) under catalytic reaction conditions. All PXRD patterns were normalized to the maximum peak of the inert α-Al_2O_3. After the final two stages, lasting 330 min and overnight, no evidence of crystalline UiO-66 was observed.

Loss of MOF Surface Area During Catalyst Deactivation. Data characterizing the loss in surface area of the MOFs during catalytic operation are shown in Figure 3.12. Recall that the MOF particles were mixed with inert alumina particles, so that surface areas reported in this figure are per unit mass of the mixtures of MOFs and inert particles. The initial surface areas of the samples UiO-66aa6, UiO-66aa30, and UiO-66aa100 were 24.0, 25.0, and 27.0 (each ± 1.5 m^2/g), respectively. These surface areas are less than those expected from the 1:40 dilutions in α-Al_2O_3 which would have been between 35 and 42 m^2 g^{-1}. The differences imply that some mechanical degradation of the MOFs occurred during the grinding/mixing with α-Al_2O_3, consistent with results presented by Su et al.,[27] who showed that applying compressive pressure with a hydraulic piston pelletizer to UiO-66 nanocrystals caused significant decreases in the MOF surface area, with >90% reduction in surface area after compression at 1.9 GPa and >20% reduction in surface area after compression of 0.4 GPa. Complementary infrared spectra of these samples showed that node–linker bonds were broken, causing irreversible amorphization as pores collapsed. The initial surface areas decreased respectively to 19, 12, and 16 m^2 g^{-1} during the activation periods as formate and acetate were removed from the nodes. Afterwards, the surface areas continued to decline, but more slowly, an additional 9, 6, and 10 m^2 g^{-1} respectively after 330 min on stream. In view of the estimated error of ± 1.5 m^2 g^{-1} in the surface area data, we infer that these MOFs underwent a significant decrease in surface area during the deactivation of the catalyst. Samples characterizing the fully deactivated UiO-66aa6 and UiO-66aa30 had surface areas of 6 ± 1.5 and 5 ± 1.5 m^2 g^{-1}. These changes are complex and not resolved by the data.

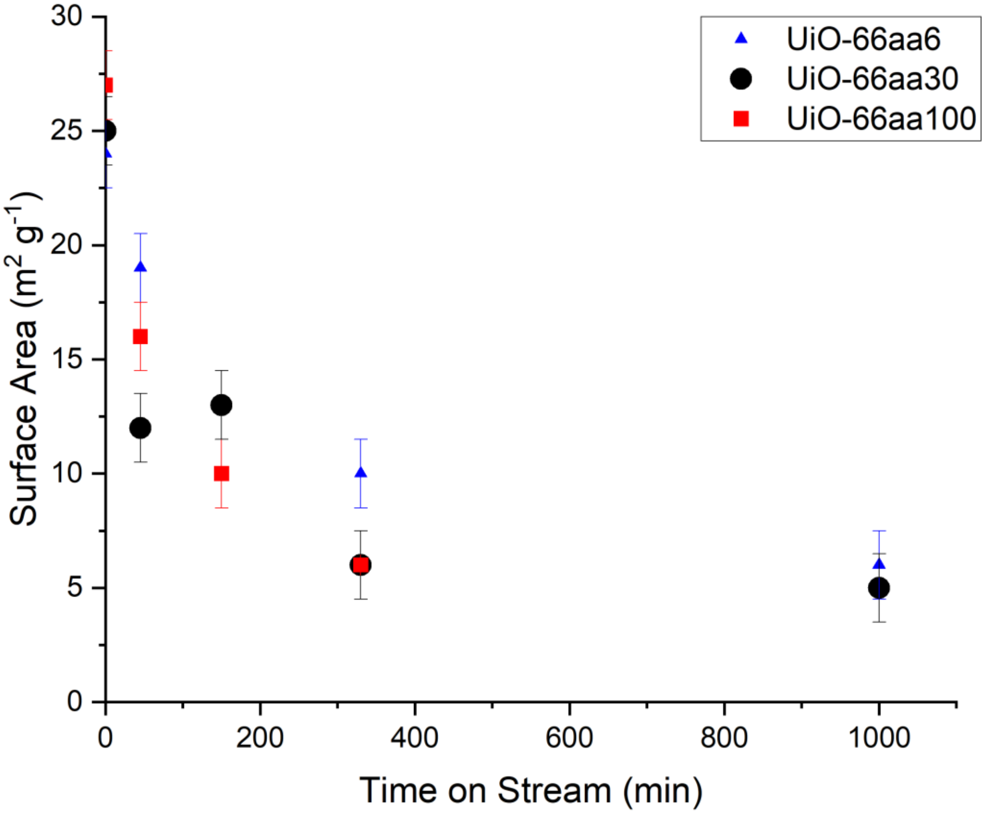

Figure 3.12. Loss of surface area during operation of the MOFs as catalysts. The MOF particles were mixed in a mass ratio of 1:40 with α-Al_2O_3 particles in the reactor, and the data represent areas of the mixtures.

NMR Evidence of Changes in MOF Node Ligand Environments During Catalyst Operation. To determine changes in the MOF compositions during catalysis, samples in separate experiments were removed from the flow reactor after times on stream of 150, 330, and 1000 min, and then digested in NaOH in D_2O, followed by analysis of the liquid by ^{1}H NMR spectroscopy (Table 3.4). No changes in acetate or formate content were observed after the activation period, consistent with the above-stated conclusion that these inhibitors were largely removed during that period.

During the activation period, isopropyl formate was removed with the rough average removal rate respectively being 12 $\mu mol_{formate}$ min^{-1} g^{-1}. Removal of isopropyl acetate could not be quantified because of convolution of the peaks of diisopropyl ether and isopropyl formate (See Appendix 3.2) Details of the estimates are given in the Appendix 2.

Table 3.4. Loss of Node–Linker Bonds and corresponding Increases in Numbers of Isopropoxy Ligands on Nodes during Catalyst Operation following the Activation Stage as determined by ^{1}H NMR Spectroscopy of Samples Digested in NaOH in D_2O.[a]

MOF	percentage of node ligands to which 1,4-benzenedicarboxylate was bonded			percentage of node ligands to which isopropoxy was bonded		
	after 150 min on stream	after 330 min on stream	after longest time on stream	after 150 min on stream	after 330 min on stream	after longest time on stream
UiO-66aa6	80 ± 10	70 ± 10	60 ± 10	20 ± 10	30 ± 10	40 ± 10
UiO-66aa30	70 ± 10	50 ± 10	50 ± 10	30 ± 10	50 ± 10	50 ± 10
UiO-66aa100	70 ± 10	70 ± 10	60 ± 10	30 ± 10	30 ± 10	40 ± 10

[a] Small amounts of formate and acetate ligands remained on the nodes and are not represented in this table; see statement in text.

The percentage of node ligands to which the linker 1,4-benzenedicarboxylate was bonded decreased with time on stream for each of the three MOFs (Table 3.4). These changes resulted in a drop of percentage of node ligands to which 1,4-bezenedicarboxylate was bonded to by at least 40 ± 10 % for all three MOFs. A corresponding increase in the percentage of node ligands to which isopropoxy was bonded increased, balancing out the loss of the organic linker. The data thus show that nearly one isopropoxy was added for each broken strut-node linkage. These results show that when the struts were unlinked from the nodes by reaction with isopropanol, they were replaced by isopropoxy ligands, demonstrating the one-to-one stoichiometry of the MOF unzipping as one kind of ligand (the linker) is replaced by another (isopropoxy). The results confirm the conclusions of the group of Yang for MOFs with metal oxide cluster nodes,[14] and they are consistent with Yang's inference that catalysts lose activity as node catalytic sites are blocked by isopropoxy groups formed from isopropanol and bonded to the metal oxide cluster nodes.[14] However, the isopropoxy groups do not account for all the observed loss of catalytic activity, as shown by the data in Table 3.1 for the three catalysts after they had reached conversions < 1.2 % at the longest times on stream— substantial fractions (typically more than half) of the node bonding sites were then occupied by ligands other than isopropoxy.

SEM Characterization of Catalysts After Various Times on Stream. SEM images of samples that had been used as catalysts for 150, 330, and at 1000 min show that the particle sizes decreased during operation; example data are shown in Figure 3.13. The particles remained intact, although the internal compositions and structures changed markedly, as shown by the NMR data (Table 3.1 and 3.4). These results, taken together, show that as the MOFs were unzipping and the internal structure and composition were changing in complex ways, the particle morphologies viewed by SEM remained largely unchanged over the course of our experiments.

The changes in particle diameters of MOFs UiO66aa6, UiO66aa30, and UiO66aa100 were found to be from 130 ± 20 to 100 ± 10; from 190 ± 27 to 120 ± 15; and from 350 ± 30 to 210 ± 30 nm, respectively. The data demonstrate a trend of decreasing particle size with increasing time on stream.

The images are consistent with the suggestion of digestion of the crystals near their surfaces and with the inference that the unzipping proceeded predominantly from the outer surfaces, but the NMR data of Table 3.1 make it clear that the unzipping extended into the full interior spaces of the MOF particles. These observations raise questions about mass transfer limitations, which are addressed in the Discussion.

The images of the used catalyst particles are as sharp as those of the unused particles, as illustrated clearly in the images of UiO-66aa100 (Figure 3.13), which show that the edges of the particles remain opaque after catalysis.

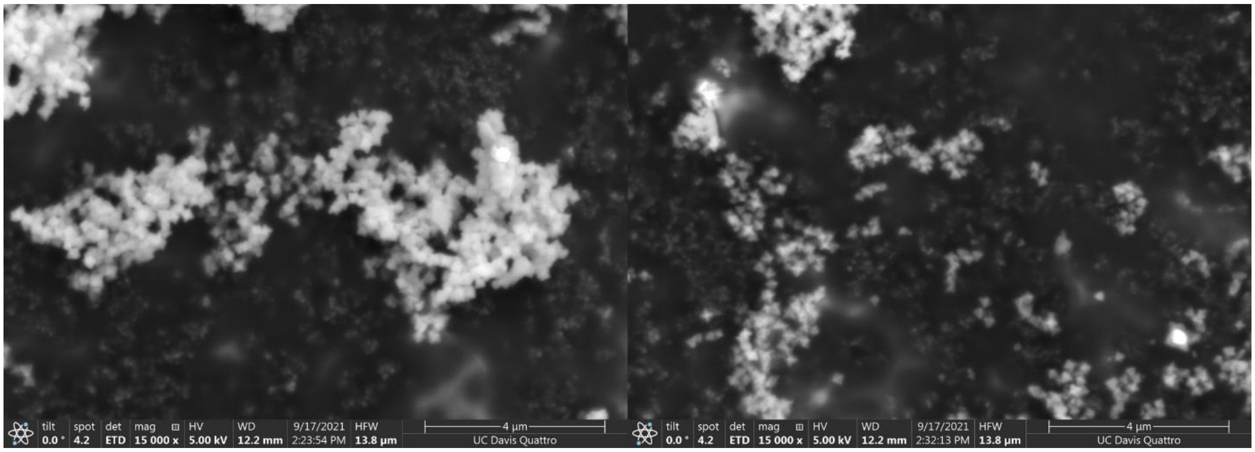

Figure 3.13. Comparison of UiO-66aa100 after use as a catalyst for 45 min (left)and 1000 (right) 1000 min on stream. Images were taken with the same magnification and instrument settings. A distinct loss of particle size during catalysis is evident, with edges of the particles still sharply defined after reaction. Images are of MOF particles that were located between the much larger α-Al_2O_3 particles. Images showing the MOF particles with α-Al_2O_3 particles are provided in Figure A2.8 in the Appendix.

Initial Catalytic Reaction Rates and Apparent Activation Energies of the Deactivation. For analysis of the kinetics of the catalytic reaction and the catalyst deactivation, the data were extrapolated to zero time on stream. The extrapolations, illustrated in Figure A3.5 in the Appendix, were done only with data following the activation stage, because data recorded during that early stage represent the catalyst that was inhibited by the formate and acetate ligands that were present initially. Data for the extrapolations were recorded for UiO-66aa6, UiO-66aa30, and UiO-66aa100 at temperatures ranging from 510 to 548 K. Reaction conditions were as follows: feed partial pressures: 80 mbar of isopropanol and 920 mbar of helium; total feed flow rate, 12.5 mL (NTP)/min; catalyst mass, 25 mg of MOF (mixed with 1.00 g of α-Al_2O_3 particles).

For analysis of initial rates of catalyst deactivation, the same extrapolation was done, again with exclusion of data determined during the activation stage, and the slope of the curves fitting the conversion data as a function of time on stream were evaluated at zero time on stream. These analyses reflect the uncertainty in the demarcation between the stages referred to as activation and deactivation; the maximum conversion was chosen as the transition between the stages. Errors in the initial rates were determined by propagation of the errors in the conversions, estimated from repeat experiments. Apparent activation energies for the reaction and catalyst deactivation (Table 3.5) were determined from the estimates of the initial catalytic reaction rates and illustrated by the Arrhenius plots of Figures A3.5 and A3.6 in the Appendix. We emphasize that the activation energies are apparent, showing temperature dependence of reaction rates and not rate constants. The value characterizing isopropanol dehydration is complicated by mass transport limitations (*vide infra*), which shows that the rates are not intrinsic. The same caveats apply to the apparent activation energies characterizing the deactivation of the MOF catalysts.

Table 3.5. Apparent Activation Energies characterizing the Catalytic Reaction and Catalyst Deactivation processes. Values were calculated by Extrapolation and Fitting of the Conversion vs Time on Stream Data, with the Conversions being Differential and Determining Catalytic Reaction Rates Directly.

MOF	apparent activation energy (kJ/mol)	
	isopropanol dehydration reaction to give propylene and diisopropyl ether	catalyst deactivation
UiO-66aa6	63 ± 5	94 ± 7
UiO-66aa30	69 ± 7	83 ± 3
UiO-66aa100	52 ± 13	78 ± 8

DISCUSSION

As much of the characterization work gave results quite similar to those reported in Chapter 2 for the methanol dehydration reaction, some of the discussion points are the same as the ones stated there. Therefore, to avoid repetition, sections on Elucidation of the MOF Catalyst Life Cycle and Implications of this Work for Practical Applications of MOFs are omitted here.

Influence of the Initial MOF Composition on Catalyst Performance and Accompanying Structural Changes. The data show that changes in the MOFs made with various initial compositions determined by the modulator to $ZrCl_4$ ratios in the synthesis were substantially different from MOF to MOF in terms of the rates of the competing processes. The three samples differed in their initial node inhibitor contents; each of the MOFs lost these inhibitors by reaction with isopropanol within the first approximately 45 min of catalytic operation, but at different rates; thus, UiO-66aa30, the MOF made with the intermediate acetic acid to $ZrCl_4$ ratio in the synthesis, continued to undergo activation at times on stream when the other two MOFs had already entered the deactivation stage. The lack of a simple relationship between this ratio and the time required for activation indicates a trade-off that suggests an influence of the MOF structure on catalyst performance. Furthermore, removal of the inhibiting ligands exposed sites for alcohol dehydration that the data show had various selectivities for propylene and diisopropyl ether. Differences in the initial selectivity for diisopropyl ether formation indicate that changes in the initial ratio of acetic acid modulator to $ZrCl_4$ imply that the several samples had different types and/or placements of catalytically active sites.

The data show that, consistent with earlier reports,[15,26,28,29] the MOF crystallinity increased with increasing modulator to $ZrCl_4$ ratios, which favored the nucleation and MOF self-assembly processes. Thus, the MOF crystallinity might be suggested to influence the numbers and ratios of node Lewis acid and terminal OH sites and thereby influence the catalyst selectivity.[14] This point is considered further below.

Details of Alcohol Dehydration Catalysis Selectivity from Literature and Comparisons to this Work. Identification of the primary products of a catalytic reaction may provide a helpful starting point for understanding the mechanism of a catalytic reaction. Yang et al.[19] characterized the surface species on UiO-66 under conditions of methanol dehydration catalysis and ethanol dehydration catalysis using infrared (IR) spectroscopy and density functional theory (DFT). Their results showed that inhibiting ligands were removed from the nodes under these conditions and that the most thermodynamically stable species of each vacancy formed by removal of a carboxylate ligand facilitated adsorption of only a single methoxy species, which was initially inferred on the basis of reports of methanol reacting with the surface hydroxyl groups of bulk zirconia powder to form in a reaction accompanied by the release of water.[9,30-31] The inference of the methoxy-terminated surface was supported by IR evidence as Yang et al. observed analogous IR bands for Zr-OCH_3 at 2932 and 2828 cm^{-1}, compared to 2923 and 2817 cm^{-1} for methoxy ligands on bulk zirconia;[30] they confirmed this assignment with methanol-D_4 substitution.[19] Recall that adsorbed formate and acetate each coordinate to two zirconium atoms on a node through their carboxylate groups and that removal of these organic ligands breaks O–Zr bonds at two adjacent zirconium atoms and that these are replaced by other oxygen-containing species in the reaction environment in experiments such as Yang's. These results are consistent with results of this work and specifically with ^{1}H NMR data characterizing digested samples taken from the catalytic reactor after 45 min under reaction conditions—these data show that isopropoxy had replaced inhibiting formate and acetate. After the initial activation of the MOFs in which these alcohol-derived alkoxy groups replace the inhibiting formate and acetate, the reactant alcohol continues to react with the MOF, replacing the organic linker. This process is analogous to the replacement of acetate and formate ligands and is slower than the removal of acetate and formate ligands, perhaps because the organic linker is ditopic and harder to remove from the MOF structure that the acetate and formate. In work by Yang et al.,[8] ^{1}H NMR analysis of digested MOFs following 20 h of ethanol dehydration catalysis in a flow reactor at 423 K showed 1.22 ethoxy ligands per node (with the only other ^{1}H NMR peak in the spectrum being that characterizing the organic linker) compared to the initial 1.07 vacancies per node, and the authors inferred that only a single ethoxy ligand was bonded to each vacancy on the basis of earlier IR and DFT results.[19] The 14% increase in vacancy density was attributed to ethanol displacing the organic linker, a process that was slower than that observed in this work, likely because of the lower temperature of the experiments in Yang's work. Thus, the data reported here verify the trend in Yang's work of a single alkoxy species replacing each vacancy exposed by the loss of the organic linker.

Yang et al.[8] sought to elucidate the mechanism of ethanol dehydration catalysis on the nodes of UiO-66 on the basis of a DFT computational analysis. The analysis resulted in two initial models which differed in involving either a single node vacancy (A) or two adjacent node vacancies (B), with each vacancy comprising two zirconium atoms, with one coordinated to a single ethoxy group and the other to molecularly adsorbed ethanol. The results of experiments reported in this work are not inconsistent with either of these models, as removal of the acetate and formate ligands exposed vacancies that became occupied by isopropoxy ligands, as shown by the ^{1}H NMR data characterizing digested samples after they had been exposed to catalytic reaction conditions for 45 min. Furthermore, differences in the initial conversion and selectivity in the catalytic reaction were observed distinguishing MOFs synthesized with different ratios of acid modulator to $ZrCl_4$ and thus having different distributions of vacancies exposed upon removal of the inhibiting formate and acetate ligands.

Yang's DFT calculations of the Gibbs free energies of the postulated transition states formed on the MOF UiO-66in the ethanol dehydration reaction to form ethylene and diethyl ether were done for E2 and S_N2 mechanisms, and in broad terms were consistent with reported mechanisms for olefin (E2) and ether (S_N2) formation on metal oxide catalysts,[23] respectively. As stated above, mechanisms of reactions on metal oxides are not expected to be the same as those on MOF nodes, but they may serve as useful starting points to begin to examine plausible mechanisms on MOF nodes. In the single-defect model (A), both the E2 mechanism for forming ethylene and the S_N2 mechanism for forming diethyl ether were found by DFT calculations to have energy barriers that lead to sluggish reactivity at 473 K, and the E2 mechanism for ethylene formation was slightly energetically favored over the S_N2 mechanism for diethyl ether formation, leading to ethylene selectivity for the single-defect models. The observation of diethyl ether and not ethylene as the dehydration product thus suggested a two-defect model. The two-defect model (B), was found to be characterized by an S_N2 mechanism for diethyl ether formation by which an ethoxy nucleophile attacks a free ethanol while the hydroxo that is forming simultaneously takes the proton of the adjacent bound ethanol to form water. This S_N2 mechanism for diethyl ether formation was favored over the other mechanisms for diethyl ether formation and ethylene formation characterizing a set of models (B) and was energetically more favorable than any of the single-defect models (A). In conclusion, the proposed mechanism for formation of diethyl ether was inferred to be favored on UiO-66 nodes where two adjacent defects exist, and the mechanism of formation of ethylene was inferred to be the favored pathway when only lone defects existed. The observation of the ether and not olefin product thus suggested that pairs of defect sites were the predominant catalytic sites.

Although Yang et al.[8] did not observe olefin formation from ethanol, their operating temperature, 473 K, was lower than those in this work, which ranged from 510 to 548 K. We suggest that at these elevated temperatures the secondary alcohol isopropanol, used in our work, likely underwent reaction via both E2 and S_N2 mechanisms inasmuch as the energy barrier calculated by Yang et al. for ethylene formation is only 3.5 kcal mol^{-1} higher than that for diethyl ether formation. This suggestion is speculative, but, consistent with this reasoning, higher selectivity for diisopropyl ether formation was observed in our work at lower temperatures for all the MOFs investigated, with the initial ether selectivity of UiO-66aa100 being > 90%.

Another investigation by Yang's group[20] dealt with the dehydration of *tert*-butyl alcohol catalyzed by UiO-66. The only dehydration product was the olefin isobutylene. Again, using DFT, the authors found the lowest-energy mechanism to be an E1 mechanism that was facilitated by adjacent alkoxy and terminal hydroxyls bonded to a single defect site; it was characterized by an activation energy of 34.7 kcal mol^{-1}.[20] This E1 mechanism for formation of isobutylene is 4.0 kcal/mol lower in energy than the S_N2 mechanism like the one described above for the formation of diethyl ether and in agreement with the higher observed TOF for *tert*-butyl alcohol dehydration.[8,20] The difference in the activation energy barriers of the models results from the hydroxyl group coordinated to the neighboring zirconium site that is within close proximity to the hydrogen of the tertiary carbon of *tert*-butyl alcohol that stabilizes the formation of an intermediate carbocation. An analogous stabilization is not possible for an E1 mechanism for dehydration of alcohols that have only primary carbon atoms, such as ethanol. Isopropanol, a secondary alcohol, might be expected to undergo reaction to form propylene by a mechanism different from those described above, but there is not yet enough information available to allow generalizations about how the mechanisms depend on alcohol structure.

Thus, the results of this work, although not inconsistent with Yang's alcohol dehydration mechanisms, are not sufficient to determine the nature of the reaction mechanism or the catalytic sites for isopropanol dehydration. Thus, although he stoichiometries of the two isopropanol dehydration reactions might seem to suggest that isopropyl alcohol reacted on single node sites to give propylene and on adjacent sites in a bimolecular process to give diisopropyl ether. This suggestion is untested but leads to the speculation that, inasmuch as propylene formation dominated over ether formation at longer times on stream in our experiments, it might be suggested that sites for the bimolecular reaction decreased in proportion to those for the single-site E1 mechanism as the MOF catalyst underwent deactivation.

It is emphasized that these suggestions are speculative, and complementary DFT analysis of isopropanol dehydration with complementary spectroscopy and catalytic reaction experiments carried out at lower temperatures would be necessary to help resolve matters.

Transport Limitations and the Locations of Reactions in the MOF Particles. Rates of reaction in porous catalyst particles such as MOFs may be influenced not just by the intrinsic rates of the reactions but also by the rates of transport of reactants and products into and out of the pores. Transport limitations in our catalysis are expected, because the window diameter of the smallest pores is estimated to be 6 Å for ideal crystalline UiO-66 and is smaller than the critical diameters of diisopropyl ether and close to the critical diameter of isopropanol and propylene.[10] Transport resistance is commonly assessed by varying the transport distance (particle diameter) while keeping the particle composition and pore structure the same. But such experiments are lacking for MOFs, because synthesis of particles of varying sizes typically results in particles of various structures and compositions,[4] as has been shown here as well. Thus, there is a lack of data determining effectiveness factors of any MOF catalyst particles.[4]

The data reported here provide some insight into the transport effects and locations of reactions in the MOF particles, although they do not fully resolve matters. For example, the data characterizing the three MOFs show that after the longest observed time on stream, a substantial amount of 1,4-benzenedicarboxylate had been removed and replaced by isopropoxy. When taken with the complementary information provided by the SEM data showing that the particle sizes deceased more significantly than the particles in Chapter 2 investigated with methanol, it is likely that isopropanol was not as rapidly transported through the MOF pores as methanol.

Further insights about the transport limitations are suggested by the changes in the MOF particle sizes during operation (Figure 9). The decrease in the particle sizes during operation and comparison of the SEM images of these MOFs shows less amorphization of the MOF particles than observed in Chapter 2 with methanol. This is consistent with the expectation that methanol would experience less transport resistance than isopropanol and result in less amorphization of the MOF particles near their exterior surfaces. For both alcohols, the data suggest that the breaking of node–linker bonds was more rapid near these exterior surfaces than near the particle centers, consistent with significant transport limitations within the porous structure. These limitations might have become more pronounced for methanol as the structure collapsed and as pore mouth blocking might have ensued. Such a collapse could be a major cause of catalyst deactivation by increasingly restricting access of methanol to the particle interiors with increasing time on stream. Thus, a plausible postulate is that the total demise of the catalyst for methanol was largely caused by pore blocking by amorphous material forming a shell around the interior which still had largely intact pores—suggested by the almost unchanged morphologies of the particle interiors shown by the SEM images. However, the loss of peaks in the XRD patterns of the UiO-66 (e.g., after 330 min time on stream, Table 2.1) provides evidence that the interior structures of the MOF particles had become amorphous, weighing against complete blocking of the pore mouths. Thus, we hypothesize that as the methanol catalytic reaction proceeded, the exterior regions of the particles became increasingly amorphized, limiting access of methanol to the MOF interior, but not shutting it off completely, so that node–linker bond breaking continued there. And recall that some deactivation could have resulted from blocking of node catalytic sites by methoxy ligands.

In contrast, the demise of the catalyst for isopropanol dehydration maintained steady state conversion at ~1.0% conversion, which indicates that the reaction was not terminated by inaccessibility to the MOF interior and that the particle continued to be slowly digested, potentially revealing new active sites. Another possibility is that bonded isopropoxy was more easily removed from catalytic sites than methoxy, as an elimination pathway would be more favored if the energetic barrier is the desorption of alkoxy from active sites. Furthermore, cycles of adsorption and desorption of alkoxy may have facilitated the digestion of the MOF by providing more opportunities for the collapse of the node structure when unsaturated zirconium atoms were exposed.

Further work is required to understand how these and other MOF catalysts reach their demise. The processes are complex, and it is a MOF synthesis challenge to prepare samples with systematically varied structures and compositions to allow resolution of the competing effects.

CONCLUSIONS

The results presented here provide a picture of how particles of a MOF (UiO-66) with Zr_6O_8 nodes underwent marked changes in composition and structure as it functioned as an isopropanol dehydration catalyst in a flow reactor. The catalyst was activated as adventitious formate and acetate ligands on the nodes (formed in the syntheses) were removed by reaction with isopropanol, freeing catalytic sites. The revealed sites were shown to have different with selectivities for propylene and diisopropyl ether formation and different evolutions of the selectivity with catalyst deactivation. The results of the selectivity differences match expectations from literature that suggest E2 type mechanisms on single sites for olefin formation and S_N2 type mechanisms on adjacent vacant sites for diisopropyl ether formation. Simultaneously, the catalyst was deactivated, ultimately reaching its demise, as isopropanol reacted with node–linker bonds to unzip the MOF structure, creating ill-defined amorphous material, especially near the outer particle surfaces, and reaching steady state at low conversions, <1 %.

REFERENCES

(1) Furukawa, H.; Cordova, K. E.; O'Keeffe, M.; Yaghi, O. M. The Chemistry and Applications of Metal-Organic Frameworks. *Science* **2013**, 341 (6149), 1230444–1230444. https://doi.org/10.1126/science.1230444.

(2) Choi, S.; Drese, J. H.; Jones, C. W. Adsorbent Materials for Carbon Dioxide Capture from Large Anthropogenic Point Sources. *ChemSusChem* **2009**, 2 (9), 796–854. https://doi.org/10.1002/cssc.200900036.

(3) Chavan, S.; Vitillo, J. G.; Gianolio, D.; Zavorotynska, O.; Civalleri, B.; Jakobsen, S.; Nilsen, M. H.; Valenzano, L.; Lamberti, C.; Lillerud, K. P.; Bordiga, S. H 2 Storage in Isostructural UiO-67 and UiO-66 MOFs. *Phys. Chem. Chem. Phys.* **2012**, 14 (5), 1614–1626. https://doi.org/10.1039/C1CP23434J.

(4) Yang, D.; Gates, B. C. Catalysis by Metal Organic Frameworks: Perspective and Suggestions for Future Research. *ACS Catalysis* **2019**, 9 (3), 1779–1798. https://doi.org/10.1021/acscatal.8b04515.

(5) Lee, J.; Farha, O. K.; Roberts, J.; Scheidt, K. A.; Nguyen, S. T.; Hupp, J. T. Metal–Organic Framework Materials as Catalysts. *Chemical Society Reviews* **2009**, 38 (5), 1450. https://doi.org/10.1039/b807080f.

(6) Guo, J.; Qin, Y.; Zhu, Y.; Zhang, X.; Long, C.; Zhao, M.; Tang, Z. Metal–Organic Frameworks as Catalytic Selectivity Regulators for Organic Transformations. *Chemical Society Reviews* **2021**, 50 (9), 5366–5396. https://doi.org/10.1039/D0CS01538E.

(7) Opanasenko, M.; Dhakshinamoorthy, A.; Čejka, J.; Garcia, H. Deactivation Pathways of the Catalytic Activity of Metal-Organic Frameworks in Condensation Reactions. *ChemCatChem* **2013**, 5 (6), 1553–1561. https://doi.org/10.1002/cctc.201200643.

(8) Yang, D.; Ortuño, M. A.; Bernales, V.; Cramer, C. J.; Gagliardi, L.; Gates, B. C. Structure and Dynamics of Zr 6 O 8 Metal–Organic Framework Node Surfaces Probed with Ethanol Dehydration as a Catalytic Test Reaction. *Journal of the American Chemical Society* **2018**, 140 (10), 3751–3759. https://doi.org/10.1021/jacs.7b13330.

(9) Yang, R. A.; Sarazen, M. L. Reaction Pathways and Deactivation Mechanisms of Isostructural Cr and Fe MIL-101 during Liquid-Phase Styrene Oxidation by Hydrogen Peroxide. *Catalysis Science & Technology* **2021**, 11 (15), 5282–5296. https://doi.org/10.1039/D1CY00567G.

(10) Cavka, J. H.; Jakobsen, S.; Olsbye, U.; Guillou, N.; Lamberti, C.; Bordiga, S.; Lillerud, K. P. A New Zirconium Inorganic Building Brick Forming Metal Organic Frameworks with Exceptional Stability. *Journal of the American Chemical Society* **2008**, 130 (42), 13850–13851. https://doi.org/10.1021/ja8057953.

(11) Kandiah, M.; Nilsen, M. H.; Usseglio, S.; Jakobsen, S.; Olsbye, U.; Tilset, M.; Larabi, C.; Quadrelli, E. A.; Bonino, F.; Lillerud, K. P. Synthesis and Stability of Tagged UiO-66 Zr-MOFs. *Chemistry of Materials* **2010**, 22 (24), 6632–6640. https://doi.org/10.1021/cm102601v.

(12) Valenzano, L.; Civalleri, B.; Chavan, S.; Bordiga, S.; Nilsen, M. H.; Jakobsen, S.; Lillerud, K. P.; Lamberti, C. Disclosing the Complex Structure of UiO-66 Metal Organic Framework: A Synergic Combination of Experiment and Theory. *Chemistry of Materials* **2011**, 23 (7), 1700–1718. https://doi.org/10.1021/cm1022882.

(13) Howarth, A. J.; Liu, Y.; Li, P.; Li, Z.; Wang, T. C.; Hupp, J. T.; Farha, O. K. Chemical, Thermal and Mechanical Stabilities of Metal–Organic Frameworks. *Nature Reviews Materials* **2016**, 1 (3), 15018. https://doi.org/10.1038/natrevmats.2015.18.

(14) Yang, D.; Gates, B. C. Elucidating and Tuning Catalytic Sites on Zirconium- and Aluminum-Containing Nodes of Stable Metal–Organic Frameworks. *Accounts of Chemical Research* **2021**, 54 (8), 1982–1991. https://doi.org/10.1021/acs.accounts.1c00029.

(15) Wei, R.; Gaggioli, C. A.; Li, G.; Islamoglu, T.; Zhang, Z.; Yu, P.; Farha, O. K.; Cramer, C. J.; Gagliardi, L.; Yang, D.; Gates, B. C. Tuning the Properties of Zr 6 O 8 Nodes in the Metal Organic Framework UiO-66 by Selection of Node-Bound Ligands and Linkers. *Chemistry of Materials* **2019**, 31 (5), 1655–1663. https://doi.org/10.1021/acs.chemmater.8b05037.

(16) Shearer, G. C.; Chavan, S.; Bordiga, S.; Svelle, S.; Olsbye, U.; Lillerud, K. P. Defect Engineering: Tuning the Porosity and Composition of the Metal–Organic Framework UiO-66 via Modulated Synthesis. *Chemistry of Materials* **2016**, 28 (11), 3749–3761. https://doi.org/10.1021/acs.chemmater.6b00602.

(17) Atzori, C.; Shearer, G. C.; Maschio, L.; Civalleri, B.; Bonino, F.; Lamberti, C.; Svelle, S.; Lillerud, K. P.; Bordiga, S. Effect of Benzoic Acid as a Modulator in the Structure of UiO-66: An Experimental and Computational Study. *The Journal of Physical Chemistry C* **2017**, 121 (17), 9312–9324. https://doi.org/10.1021/acs.jpcc.7b00483.

(18) Katz, M. J.; Brown, Z. J.; Colón, Y. J.; Siu, P. W.; Scheidt, K. A.; Snurr, R. Q.; Hupp, J. T.; Farha, O. K. A Facile Synthesis of UiO-66, UiO-67 and Their Derivatives. *Chemical Communications* **2013**, 49 (82), 9449. https://doi.org/10.1039/c3cc46105j.

(19) Yang, D.; Bernales, V.; Islamoglu, T.; Farha, O. K.; Hupp, J. T.; Cramer, C. J.; Gagliardi, L.; Gates, B. C. Tuning the Surface Chemistry of Metal Organic Framework Nodes: Proton Topology of the Metal-Oxide-Like Zr 6 Nodes of UiO-66 and NU-1000. *Journal of the American Chemical Society* **2016**, 138 (46), 15189–15196. https://doi.org/10.1021/jacs.6b08273.

(20) Yang, D.; Gaggioli, C. A.; Ray, D.; Babucci, M.; Gagliardi, L.; Gates, B. C. Tuning Catalytic Sites on Zr 6 O 8 Metal–Organic Framework Nodes via Ligand and Defect Chemistry Probed with Tert -Butyl Alcohol Dehydration to Isobutylene. *Journal of the American Chemical Society* **2020**, 142 (17), 8044–8056. https://doi.org/10.1021/jacs.0c03175.

(21) Chiang, H.; Bhan, A. Catalytic Consequences of Hydroxyl Group Location on the Rate and Mechanism of Parallel Dehydration Reactions of Ethanol over Acidic Zeolites. *Journal of Catalysis* **2010**, 271 (2), 251–261. https://doi.org/10.1016/j.jcat.2010.01.021.

(22) Costa, E.; Uguina, A.; Aguado, J.; Hernandez, P. J. Ethanol to Gasoline Process: Effect of Variables, Mechanism, and Kinetics. *Industrial & Engineering Chemistry Process Design and Development* **1985**, 24 (2), 239–244. https://doi.org/10.1021/i200029a003.

(23) Christiansen, M. A.; Mpourmpakis, G.; Vlachos, D. G. Density Functional Theory-Computed Mechanisms of Ethylene and Diethyl Ether Formation from Ethanol on γ-Al 2 O 3 (100). *ACS Catalysis* **2013**, 3 (9), 1965–1975. https://doi.org/10.1021/cs4002833.

(24) Zhuang, S.; Huang, H.; Xiao, Y.; Zhang, Z.; Tang, J.; Gates, B. C.; Yang, D. Pair Sites on Al3O Nodes of the Metal-Organic Framework MIL-100: Cooperative Roles of Defect and Structural Vacancy Sites in Methanol Dehydration Catalysis. *Journal of Catalysis* **2021**, 404, 128–138. https://doi.org/10.1016/j.jcat.2021.09.006.

(25) Wang, Z.; Babucci, M.; Zhang, Y.; Wen, Y.; Peng, L.; Yang, B.; Gates, B. C.; Yang, D. Dialing in Catalytic Sites on Metal Organic Framework Nodes: MIL-53(Al) and MIL-68(Al) Probed with Methanol Dehydration Catalysis. *ACS Applied Materials & Interfaces* **2020**, 12 (47), 53537–53546. https://doi.org/10.1021/acsami.0c16559.

(26) Morris, W.; Wang, S.; Cho, D.; Auyeung, E.; Li, P.; Farha, O. K.; Mirkin, C. A. Role of Modulators in Controlling the Colloidal Stability and Polydispersity of the UiO-66 Metal–Organic Framework. *ACS Applied Materials & Interfaces* **2017**, 9 (39), 33413–33418. https://doi.org/10.1021/acsami.7b01040.

(27) Su, Z.; Miao, Y.-R.; Zhang, G.; Miller, J. T.; Suslick, K. S. Bond Breakage under Pressure in a Metal Organic Framework. *Chemical Science* **2017**, 8 (12), 8004–8011. https://doi.org/10.1039/C7SC03786D.

(28) Schaate, A.; Roy, P.; Godt, A.; Lippke, J.; Waltz, F.; Wiebcke, M.; Behrens, P. Modulated Synthesis of Zr-Based Metal-Organic Frameworks: From Nano to Single Crystals. *Chemistry - A European Journal* **2011**, 17 (24), 6643–6651. https://doi.org/10.1002/chem.201003211.

(29) Liu, N.; Shi, L.; Meng, X. Tuning the Adsorption Properties of UiO-66 via Acetic Acid Modulation. *Journal of Chemical Sciences* **2019**, 131 (6), 50. https://doi.org/10.1007/s12039-019-1628-3.

(30) Jung, K. T.; Bell, A. T. An in Situ Infrared Study of Dimethyl Carbonate Synthesis from Carbon Dioxide and Methanol over Zirconia. *Journal of Catalysis* **2001**, 204 (2), 339–347. https://doi.org/10.1006/jcat.2001.3411.

(31) Ouyang, F.; Kondo, J. N.; Maruya, K.; Domen, K. Site Conversion of Methoxy Species on ZrO 2. *The Journal of Physical Chemistry B* **1997**, 101 (25), 4867–4869. https://doi.org/10.1021/jp971048a.

CHAPTER FOUR

Conclusions and Suggested Future Work following the Investigations of the Methanol and Isopropanol Dehydration Reactions Catalyzed on UiO-66

CONCLUSIONS

The Catalytic Life-Cycle of UiO-66 with Methanol and Isopropanol Dehydration Reactions. Modulation of the MOF synthesis with various numbers of mols of acetic acid per mol of $ZrCl_4$ resulted in changes in the initial compositions of the UiO-66 nodes and specifically with initial node inhibitor ligand contents. These were removed by methanol and by isopropanol during the activation stages of the catalytic reactions. These results are consistent with the literature showing that these node ligands are removed via reaction with reactant alcohols, eluting as their respective esters.[1–4] Characterization of the initial UiO-66 structures also revealed increases in particle size and crystallinity with increasing modulator to $ZrCl_4$ ratios, again consistent with literature.[4–7]

Combining catalyst performance data with complementary data characterizing the MOFs defined several stages of the life cycles of the MOFs as catalysts, showing that the changes in acid modulation changed the rates at which UiO-66 lost catalytic activity and underwent changes in structural properties. These results show how UiO-66aa30, the MOF made with the intermediate ratio of acetic acid to $ZrCl_4$ continued to undergo activation in methanol and isopropanol dehydration reactions at times on stream when the other two MOFs had entered the deactivation stage. In the isopropanol dehydration reaction experiments, it was the most highly modulated MOF UiO-66aa100 that demonstrated the highest initial selectivity for diisopropyl ether, and this MOF underwent a different pattern of deactivation and changes of the selectivity compared to the other two MOFs, with no clear trend showing how the selectivity changes during deactivation depend on the MOF properties. The isopropanol dehydration reaction is a selective and stoichiometrically simple reaction compared to highly selective reactions desired for MOF catalysts, however characterization of the complex changes in MOF selectivity and structure during deactivation, even with this alcohol, show the complexity of the processes causing catalyst deactivation. Such issues cannot be ignored in practical development of catalysts.

The methodology of these experiments, which combines standard, well-documented characterization techniques in a novel way, will be useful in assessing the MOFs' practicality in applications, including gas adsorption/purification and selective catalysis. The inherent instability of the organic linker-node bonds and questions relating to the integrity of MOF structures at elevated temperatures and in reactive environments can be addressed with these complementary techniques. As shown in this work and in the literature,[4–7] control of the acid modulation provides opportunities to manipulate MOF chemistry, structure, and resulting mechanisms of deactivation. Thus, this methodology will also be important in the optimization of MOF syntheses by providing metrics to measure application performance between MOFs.

Olefin and Ether Selectivity in Methanol and Isopropanol Dehydration Reactions. The terminal stages of the two reactions differ, as methanol dehydration catalysts had stopped working entirely at times on stream greater than 1000 min whereas isopropanol conversion approached steady state at conversions around 1% at the longest times on stream recorded, even though the MOFs were apparently fully degraded. Whatever was left in the materials after isopropanol catalysis was evidently catalytically active for propylene formation (but not diisopropyl ether formation). Therefore, in both alcohol dehydration reactions, the ether formation had been deactivated by the terminal stage of catalyst operation. This result might suggest that there is a similar deactivation mechanism of the sites active for ether formation in both reactions on UiO-66, but this suggestion remains unresolved by the data. This result is consistent with the complementary DFT and IR studies of alcohol dehydration mechanisms on UiO-66 which suggest that olefin formation is energetically favored on single sites, requiring less ordered-structures than two-site mechanisms for ether formation.[1,2] Thus, we could speculate that the degraded catalysts had single sites for olefin formation but lacked paired sites for ether formation. This suggestion is worthy of further investigation.

Transport Limitations. The narrow pores of ideal crystalline UiO-66 have a diameter of about 6 Å**,** and these are small enough to limit the transport of the reactants and products of both reactions in the MOF pores. In the methanol dehydration experiments, particle diameters did not decrease much over the course of the reaction despite replacement of a large fraction of the organic linkers with methoxy. This result would suggest that methanol, while reacting primarily near the exterior of MOF particle surfaces, was transported substantially into interiors of the MOF particles. Characterization data show the collapse of the MOF structure, and it is likely that pores collapsed and limited methanol access as the reaction progressed, eventually resulting in deactivation of the MOF.

Particle diameters decreased much more substantially in the isopropanol dehydration reactions, and it is likely that isopropanol was not as rapidly transported through the MOF pores as methanol. Additionally, SEM images show less amorphization of the MOF particles near their exterior surface when the reactant was isopropanol than when it was methanol, which also suggests that the reaction proceeded near the MOF particle surfaces. However, the issues are complex, and further work would be needed to clarify how transport effects in UiO-66 and other MOFs affect reactivity. The reactivity issues could be important in applications beyond catalysis. It is a MOF synthesis challenge to prepare samples with systematically varied structures and compositions to allow resolution of the competing effects—and to prepare them uniformly.

SUGGESTED FUTURE RESEARCH

Transport Limitations. The impacts of transport limitations on the catalytic life-cycle have not been quantified by the work of this dissertation (or in other work); however, their significance in the destruction of the MOF is clear from the data. In other materials, such as metal oxides, transport limitations have been quantified by varying the particle size in synthesis (or by crushing and grinding) and allowing measurements of how catalysis depends on the particle size (transport length). The work reported here is consistent with the literature, demonstrating that changes in particle size from acid-modulation also result in chemical and structural changes in the MOFs, but the complexity of the issues limits the ability to compare MOFs of various particle sizes—it is not evident how to make MOF particles that have different particle sizes and identical structures and compositions. Making particles smaller by crushing and grinding does not provide a simple answer, because as MOF particles grow the composition of the added layers changes. This nonuniformity of structure results in a complex challenge for materials synthesis, and it is regarded as a central challenge.

However, close observation of the literature SEM images of MOFs synthesized with various ratios of modulator to $ZrCl_4$ shows the transition from quasi-spherical to octahedral particle geometries occurring at different particle diameters.[4–7] It may be possible, by variation of the compositions of the synthesis constituents to generate samples with similar nodal chemistry at different sizes. A suggestion would be to use SEM to identify transitions from quasi-spherical to octahedral geometries of the particles (perhaps before lengthy washing and activating procedures) for syntheses at various compositions of constituents. Structures just after the transition could then be investigated with ^{1}H NMR spectroscopy of digested samples, particle size measurements, and surface area measurements to identify whether there are similarities in the MOF chemistry and structure with changes in the particle size. If the species are determined to be chemically and structurally similar, the reaction and deactivation rates for methanol dehydration, similar to those determined in this work, may then be compared between the MOFs of different particle sizes with differences in the rates providing insight to the transport effects.

Associated with the role of transport limitations in the methanol and isopropanol dehydration experiments of this work are questions pertaining to the state of the interior of the MOF particle. The SEM data suggest that methanol experienced less resistance to transport into the interior of the MOF particles than isopropanol and that a thicker shell of amorphized material was present on the particles of UiO-66 that underwent methanol catalysis than on those that underwent isopropanol dehydration. However, characterization of the interior of the MOF was not accomplished in this work, and information on the structure, crystallinity, and composition at various positions within MOF particles would be helpful in addressing questions about the transport effects. This work might be accomplished with transmission electron microscopy and observing changes in the particle crystallinity following different time of exposure to reaction conditions. Specifically, measurements of the thickness of the amorphous layer would lead to mechanistic insights about the transport limitations seen in these MOFs. However, these experiments would prove exceedingly difficult because the organic linkers of MOFs are rapidly destroyed by the electron beam.

Both proposed set of materials science experiments have complexities that are not easily resolved. Significant challenges are presented in obtaining chemical and structural uniformity in MOFs synthesized to yield batches with different particle sizes and in the use of imaging techniques to document the rate of amorphization of the MOF. Therefore, although with significant effort these research avenues would be worthy of a PhD level investigation, I cannot recommend them because of the complexities involved. However, close attention should be given to the development of imaging for sensitive materials such as MOFs because advances on these techniques are likely and facilitate these investigations. For example recently, beam damage effects on MOFs have shown to be mitigated by use of extremely low-dose imaging (dose rate of less than 0.1 electrons $Å^{-2}$ s^{-1}) and images of MOF NU-1000, in the same family as UiO-66, have been obtained that resolve the atomic structure of the nodes.[8]

Characterization of other MOFs. Combinations of materials characterization techniques and catalytic reactor data to investigate mechanisms of deactivation can be applied to reactions beyond methanol dehydration and isopropanol dehydration and to other MOFs. Comparisons of this work and to the work of Yang et al. with an investigation of ethanol dehydration and *tert*-butyl alcohol on UiO-66 synthesized with systematically varied degrees of acid modulation would complement the investigations of this work.[1,2] The SEM data of these investigations would be of particular interest as they might test the hypothesis of a trend of decreasing degree of amorphization and increased loss of particle size with increased ratios of modulator to $ZrCl_4$.

Additionally, this work would continue the story of changes in initial selectivity and in changes in selectivity with structural changes to the MOF under reactive conditions. Yang et al. proposed different mechanisms of alcohol dehydration for ethanol and *tert*-butyl alcohol, with the key difference likely related to ethanol being a primary alcohol and *tert*-butyl alcohol being a tertiary alcohol. Thus, in addition to the SEM data, the changes in selectivity with conversion are also of interest because they should provide further insight into the reaction mechanisms suggested by Yang et al. and are consistent with the results of this work.[1,2]

However, other information relating to the changes in surface area and crystallinity would not be expected to contribute to the work here. Additionally, the loss of inhibiting ligands for ethanol and *tert*-butyl alcohol dehydrations have been documented by Yang et al.,[1,2] and the methodology has been developed for these experiments, as discussed in this dissertation. Therefore, I do not believe that this work contains the scope required for a novel PhD project, but it would be sufficient for a master's project and would contribute meaningfully to this work.

REFERENCES

(1) Yang, D.; Ortuño, M. A.; Bernales, V.; Cramer, C. J.; Gagliardi, L.; Gates, B. C. Structure and Dynamics of Zr 6 O 8 Metal–Organic Framework Node Surfaces Probed with Ethanol Dehydration as a Catalytic Test Reaction. *Journal of the American Chemical Society* **2018**, 140 (10), 3751–3759. https://doi.org/10.1021/jacs.7b13330.

(2) Yang, D.; Gaggioli, C. A.; Ray, D.; Babucci, M.; Gagliardi, L.; Gates, B. C. Tuning Catalytic Sites on Zr 6 O 8 Metal–Organic Framework Nodes via Ligand and Defect Chemistry Probed with Tert -Butyl Alcohol Dehydration to Isobutylene. *Journal of the American Chemical Society* **2020**, 142 (17), 8044–8056. https://doi.org/10.1021/jacs.0c03175.

(3) Wang, Z.; Babucci, M.; Zhang, Y.; Wen, Y.; Peng, L.; Yang, B.; Gates, B. C.; Yang, D. Dialing in Catalytic Sites on Metal Organic Framework Nodes: MIL-53(Al) and MIL-68(Al) Probed with Methanol Dehydration Catalysis. *ACS Applied Materials & Interfaces* **2020**, 12 (47), 53537–53546. https://doi.org/10.1021/acsami.0c16559.

(4) Wei, R.; Gaggioli, C. A.; Li, G.; Islamoglu, T.; Zhang, Z.; Yu, P.; Farha, O. K.; Cramer, C. J.; Gagliardi, L.; Yang, D.; Gates, B. C. Tuning the Properties of Zr 6 O 8 Nodes in the Metal Organic Framework UiO-66 by Selection of Node-Bound Ligands and Linkers. *Chemistry of Materials* **2019**, 31 (5), 1655–1663. https://doi.org/10.1021/acs.chemmater.8b05037.

(5) Schaate, A.; Roy, P.; Godt, A.; Lippke, J.; Waltz, F.; Wiebcke, M.; Behrens, P. Modulated Synthesis of Zr-Based Metal-Organic Frameworks: From Nano to Single Crystals. Chemistry - *A European Journal* **2011**, 17 (24), 6643–6651. https://doi.org/10.1002/chem.201003211.

(6) Liu, N.; Shi, L.; Meng, X. Tuning the Adsorption Properties of UiO-66 via Acetic Acid Modulation. *Journal of Chemical Sciences* **2019**, 131 (6), 50. https://doi.org/10.1007/s12039-019-1628-3.

(7) Morris, W.; Wang, S.; Cho, D.; Auyeung, E.; Li, P.; Farha, O. K.; Mirkin, C. A. Role of Modulators in Controlling the Colloidal Stability and Polydispersity of the UiO-66 Metal–

Organic Framework. *ACS Applied Materials & Interfaces* **2017**, 9 (39), 33413–33418. https://doi.org/10.1021/acsami.7b01040.

(8) Mehdi, B. L.; Stevens, A. J.; Moeck, P.; Dohnalkova, A.; Vjunov, A.; Fulton, J. L.; Camaioni, D. M.; Farha, O. K.; Hupp, J. T.; Gates, B. C.; Lercher, J. A.; Browning, N. D. Low-Dose and In-Painting Methods for (Near) Atomic Resolution STEM Imaging of Metal Organic Frameworks (MOFs). *Microscopy and Microanalysis* **2017**, 23 (S1), 1804–1805. https://doi.org/10.1017/S1431927617009680.

Appendix Chapter 2

Life History of the Metal-Organic Framework UiO-66 Catalyzing Methanol Dehydration:

Synthesis, Activation, Deactivation, and Demise

Reproducibility of separate UiO-66aa30 batches as demonstrated by their catalytic performance.

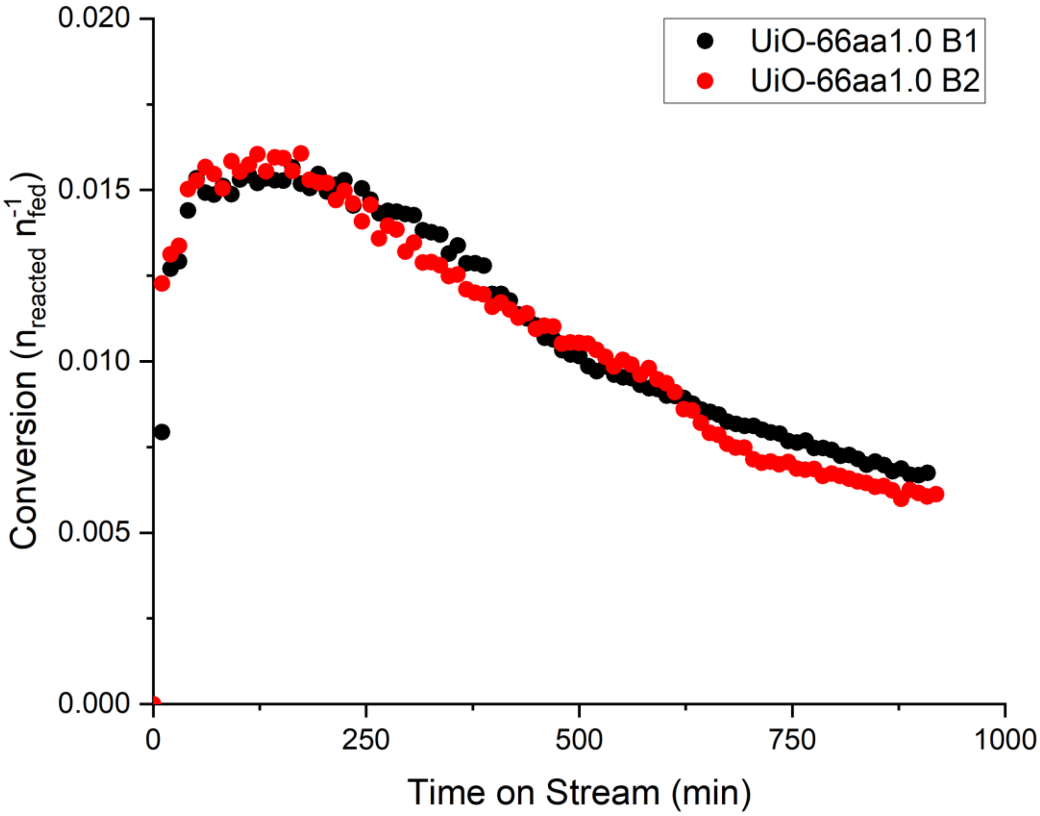

Figure A2.1. Conversion of methanol in dehydration to give dimethyl ether: data characterizing by separate catalyst synthesis batches (B1 and B2) of UiO-66aa30 characterizing the reproducibility of repeat synthesis. Reaction conditions: 473 K, feed partial pressure of 220 mbar of methanol and 780 mbar of helium; total flow rate 10 mL (NTP)/ min; catalyst mass, 50 mg of MOF and 1.00 g of α-Al_2O_3 particles mixed with mortar and pestle for 60 s. The symbol n represents number of mols of methanol.

Comparison of physical properties of the MOFs UiO-66aa6, UiO-66aa30, and UiO-66aa100 to literature values for similar UiO-66 MOFs synthesized with acetic acid modulator.

Table A2.1. Comparison of the synthesis conditions for UiO-66 with acetic acid modulator between this work and the literature. Abbreviations are as follows: BDC—1,4-benzenedicarboxylic acid; aa—acetic acid; DMF—N,N-dimethylformamide; THF—tetrahydrofuran. For washing procedure $\#_1$x$\#_2$d refers to the total number of washes ($\#_1$) spread out over a number of days.

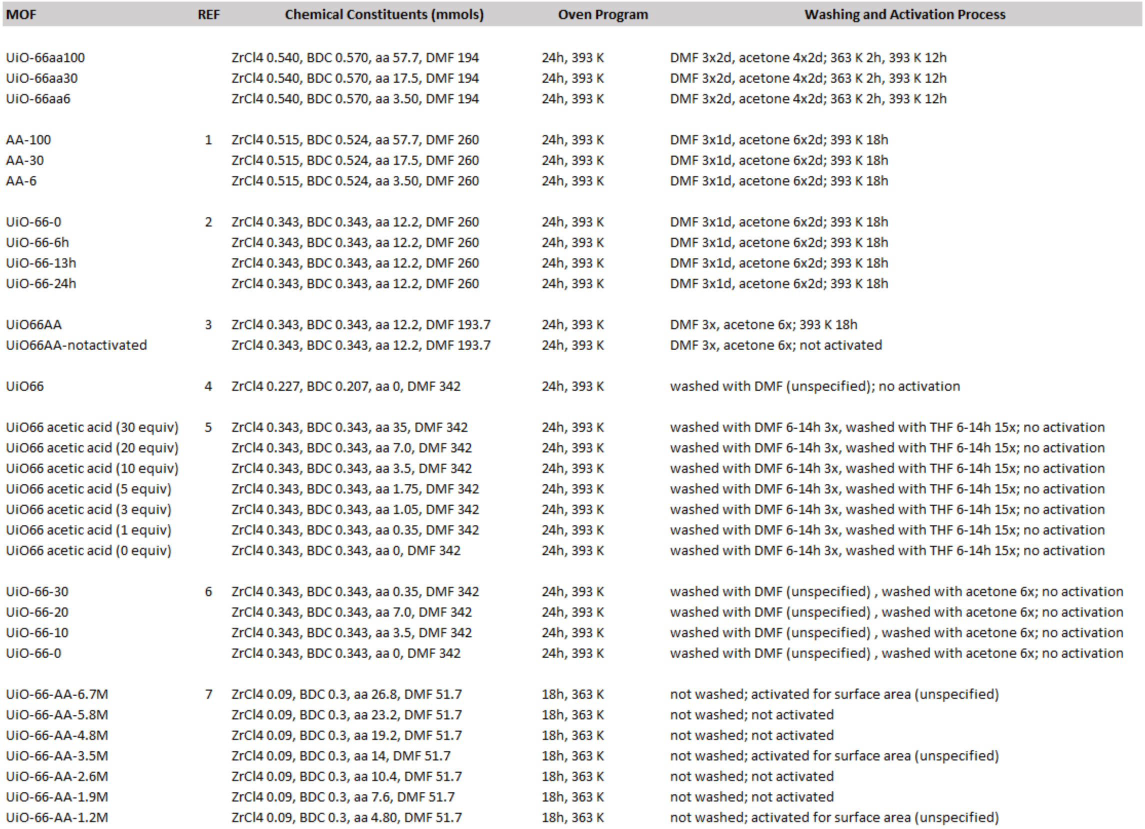

MOF	REF	Chemical Constituents (mmols)	Oven Program	Washing and Activation Process
UiO-66aa100		ZrCl4 0.540, BDC 0.570, aa 57.7, DMF 194	24h, 393 K	DMF 3x2d, acetone 4x2d; 363 K 2h, 393 K 12h
UiO-66aa30		ZrCl4 0.540, BDC 0.570, aa 17.5, DMF 194	24h, 393 K	DMF 3x2d, acetone 4x2d; 363 K 2h, 393 K 12h
UiO-66aa6		ZrCl4 0.540, BDC 0.570, aa 3.50, DMF 194	24h, 393 K	DMF 3x2d, acetone 4x2d; 363 K 2h, 393 K 12h
AA-100	1	ZrCl4 0.515, BDC 0.524, aa 57.7, DMF 260	24h, 393 K	DMF 3x1d, acetone 6x2d; 393 K 18h
AA-30		ZrCl4 0.515, BDC 0.524, aa 17.5, DMF 260	24h, 393 K	DMF 3x1d, acetone 6x2d; 393 K 18h
AA-6		ZrCl4 0.515, BDC 0.524, aa 3.50, DMF 260	24h, 393 K	DMF 3x1d, acetone 6x2d; 393 K 18h
UiO-66-0	2	ZrCl4 0.343, BDC 0.343, aa 12.2, DMF 260	24h, 393 K	DMF 3x1d, acetone 6x2d; 393 K 18h
UiO-66-6h		ZrCl4 0.343, BDC 0.343, aa 12.2, DMF 260	24h, 393 K	DMF 3x1d, acetone 6x2d; 393 K 18h
UiO-66-13h		ZrCl4 0.343, BDC 0.343, aa 12.2, DMF 260	24h, 393 K	DMF 3x1d, acetone 6x2d; 393 K 18h
UiO-66-24h		ZrCl4 0.343, BDC 0.343, aa 12.2, DMF 260	24h, 393 K	DMF 3x1d, acetone 6x2d; 393 K 18h
UiO66AA	3	ZrCl4 0.343, BDC 0.343, aa 12.2, DMF 193.7	24h, 393 K	DMF 3x, acetone 6x; 393 K 18h
UiO66AA-notactivated		ZrCl4 0.343, BDC 0.343, aa 12.2, DMF 193.7	24h, 393 K	DMF 3x, acetone 6x; not activated
UiO66	4	ZrCl4 0.227, BDC 0.207, aa 0, DMF 342	24h, 393 K	washed with DMF (unspecified); no activation
UiO66 acetic acid (30 equiv)	5	ZrCl4 0.343, BDC 0.343, aa 35, DMF 342	24h, 393 K	washed with DMF 6-14h 3x, washed with THF 6-14h 15x; no activation
UiO66 acetic acid (20 equiv)		ZrCl4 0.343, BDC 0.343, aa 7.0, DMF 342	24h, 393 K	washed with DMF 6-14h 3x, washed with THF 6-14h 15x; no activation
UiO66 acetic acid (10 equiv)		ZrCl4 0.343, BDC 0.343, aa 3.5, DMF 342	24h, 393 K	washed with DMF 6-14h 3x, washed with THF 6-14h 15x; no activation
UiO66 acetic acid (5 equiv)		ZrCl4 0.343, BDC 0.343, aa 1.75, DMF 342	24h, 393 K	washed with DMF 6-14h 3x, washed with THF 6-14h 15x; no activation
UiO66 acetic acid (3 equiv)		ZrCl4 0.343, BDC 0.343, aa 1.05, DMF 342	24h, 393 K	washed with DMF 6-14h 3x, washed with THF 6-14h 15x; no activation
UiO66 acetic acid (1 equiv)		ZrCl4 0.343, BDC 0.343, aa 0.35, DMF 342	24h, 393 K	washed with DMF 6-14h 3x, washed with THF 6-14h 15x; no activation
UiO66 acetic acid (0 equiv)		ZrCl4 0.343, BDC 0.343, aa 0, DMF 342	24h, 393 K	washed with DMF 6-14h 3x, washed with THF 6-14h 15x; no activation
UiO-66-30	6	ZrCl4 0.343, BDC 0.343, aa 0.35, DMF 342	24h, 393 K	washed with DMF (unspecified) , washed with acetone 6x; no activation
UiO-66-20		ZrCl4 0.343, BDC 0.343, aa 7.0, DMF 342	24h, 393 K	washed with DMF (unspecified) , washed with acetone 6x; no activation
UiO-66-10		ZrCl4 0.343, BDC 0.343, aa 3.5, DMF 342	24h, 393 K	washed with DMF (unspecified) , washed with acetone 6x; no activation
UiO-66-0		ZrCl4 0.343, BDC 0.343, aa 0, DMF 342	24h, 393 K	washed with DMF (unspecified) , washed with acetone 6x; no activation
UiO-66-AA-6.7M	7	ZrCl4 0.09, BDC 0.3, aa 26.8, DMF 51.7	18h, 363 K	not washed; activated for surface area (unspecified)
UiO-66-AA-5.8M		ZrCl4 0.09, BDC 0.3, aa 23.2, DMF 51.7	18h, 363 K	not washed; not activated
UiO-66-AA-4.8M		ZrCl4 0.09, BDC 0.3, aa 19.2, DMF 51.7	18h, 363 K	not washed; not activated
UiO-66-AA-3.5M		ZrCl4 0.09, BDC 0.3, aa 14, DMF 51.7	18h, 363 K	not washed; activated for surface area (unspecified)
UiO-66-AA-2.6M		ZrCl4 0.09, BDC 0.3, aa 10.4, DMF 51.7	18h, 363 K	not washed; not activated
UiO-66-AA-1.9M		ZrCl4 0.09, BDC 0.3, aa 7.6, DMF 51.7	18h, 363 K	not washed; not activated
UiO-66-AA-1.2M		ZrCl4 0.09, BDC 0.3, aa 4.80, DMF 51.7	18h, 363 K	not washed; activated for surface area (unspecified)

Table A2.2. Comparison of the structural properties for UiO-66 with acetic acid modulator between this work and the literature. Particle sizes for this work and the work by Morris et al. were calculated from SEM images. In the work by Schaate et al. the particle sizes were determined by the Scherrer equation.[5]

MOF	REF	Surface Area (m^2/g)	Particle Size (nm)	Particle Geometery	PXRD Different (Y/N)	Percentage Node Ligands Acetate	Percentage Node Ligands Formate
UiO-66aa100		1629	380 ± 30	octahedral	N (Fm-3m)	14	3
UiO-66aa30		1382	210 ± 39	quasi-spherical	N (Fm-3m)	12	4
UiO-66aa6		1530	140 ± 15	quasi-spherical	N (Fm-3m)	3	4
AA-100	1	1479	N/A	octahedral	N (Fm-3m)	14.5	1.6
AA-30		1391.5	N/A	quasi-spherical	N (Fm-3m)	6.7	2.1
AA-6		1343	N/A	quasi-spherical	N (Fm-3m)	2.5	2.7
UiO-66-0	2	1327	N/A	octahedral	N (Fm-3m)	6.7	2.1
UiO-66-6h		989	N/A	N/A	N (Fm-3m)	6.6	1.5
UiO-66-13h		1047	N/A	N/A	N (Fm-3m)	6.4	1.3
UiO-66-24h		988	N/A	N/A	N (Fm-3m)	6.3	1.25
UiO66AA	3	1546	N/A	quasi-spherical	N (Fm-3m)	7.2	1.6
UiO66AA-notactivated		1391	N/A	N/A	N/A	N/A	N/A
UiO66	4	1187	N/A	N/A	N (Fm-3m)	N/A	N/A
UiO66 acetic acid (30 equiv)	5	1400	171 dXRD	N/A	N (Fm-3m)	N/A	N/A
UiO66 acetic acid (20 equiv)		N/A	141 dXRD	N/A	N (Fm-3m)	N/A	N/A
UiO66 acetic acid (10 equiv)		N/A	87 dXRD	N/A	N (Fm-3m)	N/A	N/A
UiO66 acetic acid (5 equiv)		N/A	53 dXRD	N/A	Y (Fm-3m) broadening of peaks	N/A	N/A
UiO66 acetic acid (3 equiv)		N/A	62 dXRD	N/A	Y (Fm-3m) broadening of peaks	N/A	N/A
UiO66 acetic acid (1 equiv)		N/A	66 dXRD	N/A	Y (Fm-3m) broadening of peaks	N/A	N/A
UiO66 acetic acid (0 equiv)		N/A	72 dXRD	N/A	N (Fm-3m)	N/A	N/A
UiO-66-30	6	1424.03	N/A	N/A	N (Fm-3m)	N/A	N/A
UiO-66-20		1326.36	N/A	N/A	N (Fm-3m)	N/A	N/A
UiO-66-10		1169.5	N/A	N/A	N (Fm-3m)	N/A	N/A
UiO-66-0		987.95	N/A	N/A	N (Fm-3m)	N/A	N/A
UiO-66-AA-6.7M	7	1300	721 ± 56	octahedral	N (Fm-3m)	N/A	N/A
UiO-66-AA-5.8M			514 ± 88	octahedral	N (Fm-3m)	N/A	N/A
UiO-66-AA-4.8M			270 ± 48	octahedral	N (Fm-3m)	N/A	N/A
UiO-66-AA-3.5M		1280	208 ± 56	mix	N (Fm-3m)	N/A	N/A
UiO-66-AA-2.6M			72 ± 18	mix	N (Fm-3m)	N/A	N/A
UiO-66-AA-1.9M			34 ± 22	quasi-spherical	N (Fm-3m)	N/A	N/A
UiO-66-AA-1.2M		1050	17 ± 2	quasi-spherical	N (Fm-3m)	N/A	N/A

PXRD patterns of the three samples: UiO-66aa6, UiO-66aa30, and UiO-66aa100.

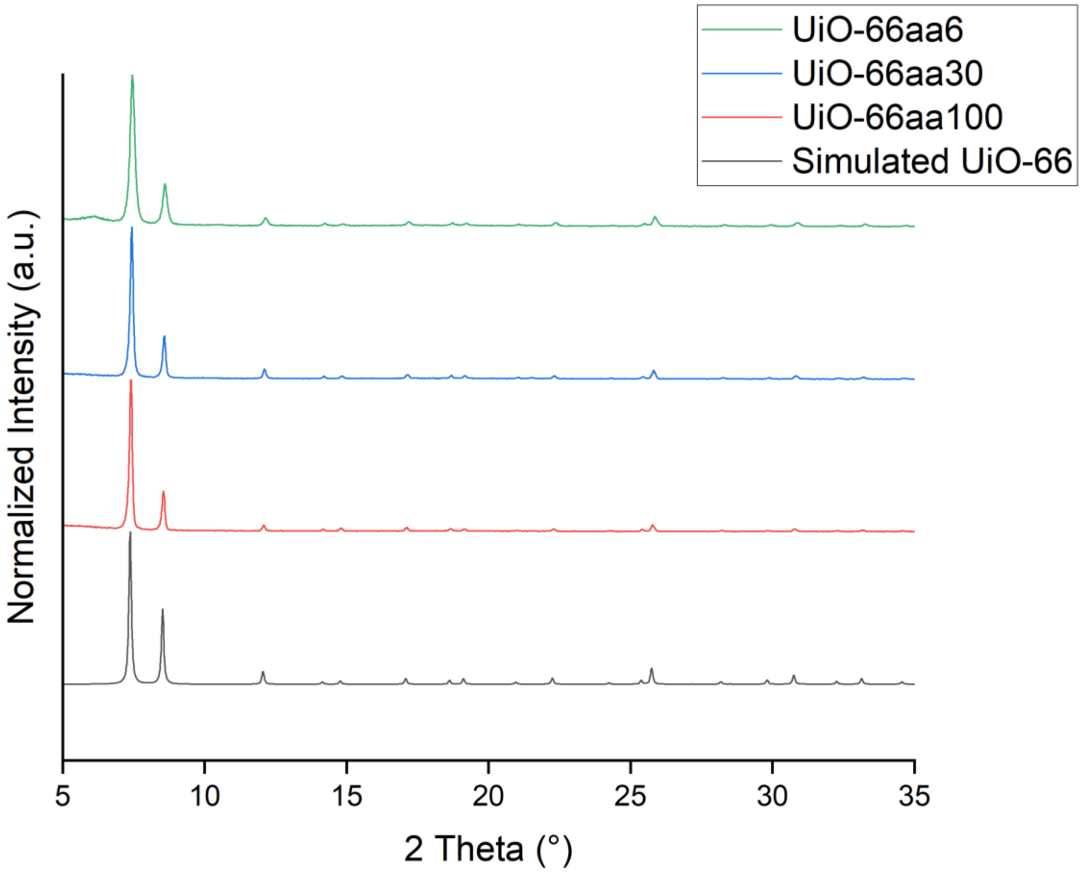

Figure A2.2. Simulated and observed PXRD patterns characterizing UiO-66 synthesized with various ratios of acetic acid modulator to zirconium chloride. The patterns have been normalized to the height of the largest peak at 2θ = 7.45°.

SEM images of UiO-66aa6, UiO-66aa30, and UiO-66aa100.

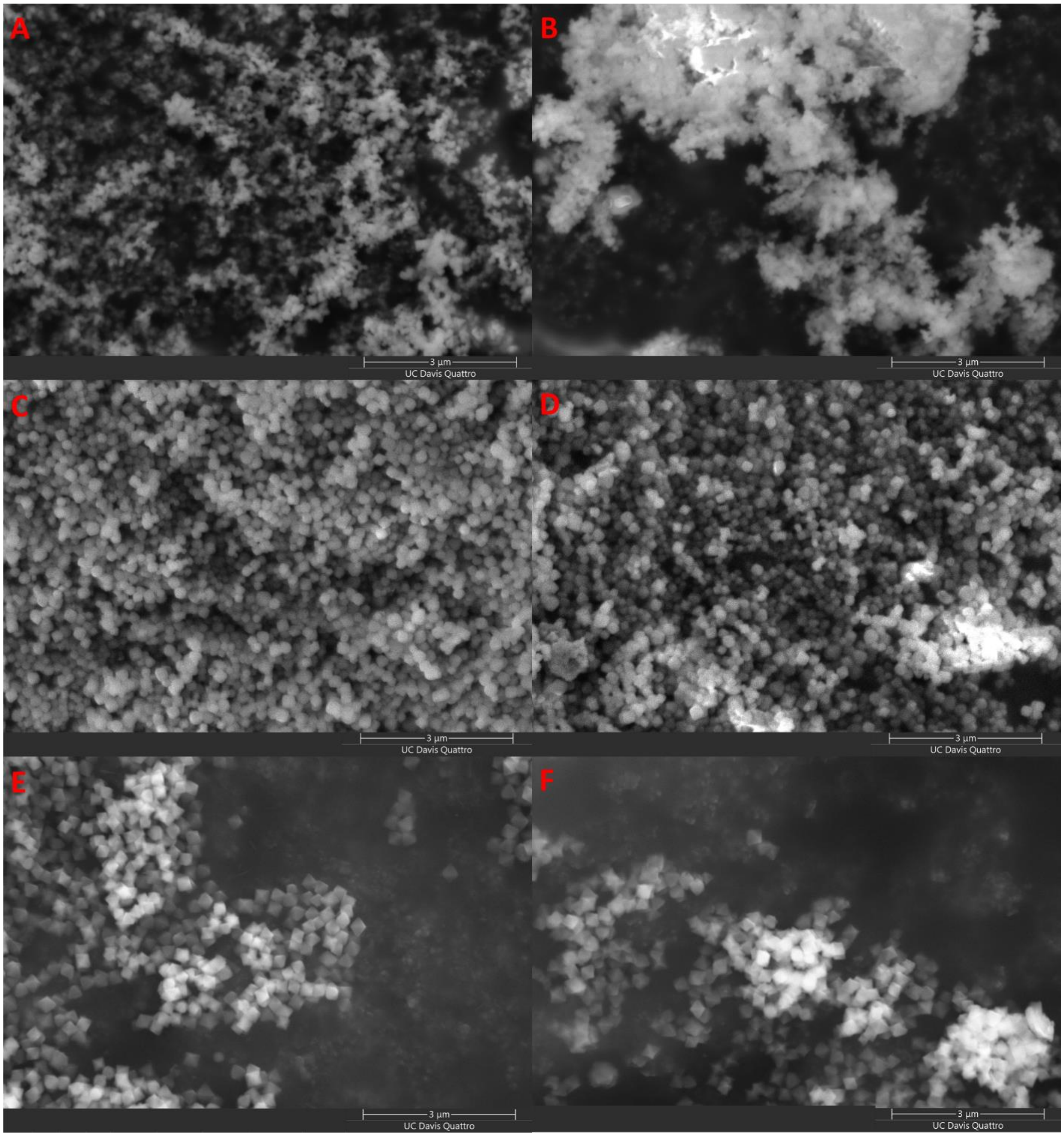

Figure A2.3. SEM images of UiO-66 modulated with 6 (A), 30 (C), and 100 (E) mols of acetic acid per mol of $ZrCl_4$. Each sample was imaged at the same 20-K magnification, and a corresponding scale bar is provided. As more acetic acid was introduced in the synthesis, the particles became larger and less nearly spherical and more nearly octahedral in shape. SEM images of the three sets of MOF particles after (B, D, F) catalyst activation during 45 min on stream in the flow reactor. See text for discussion of lack of sharpness of images of used catalysts.

Determination of catalytic reaction rates from differential conversion data.

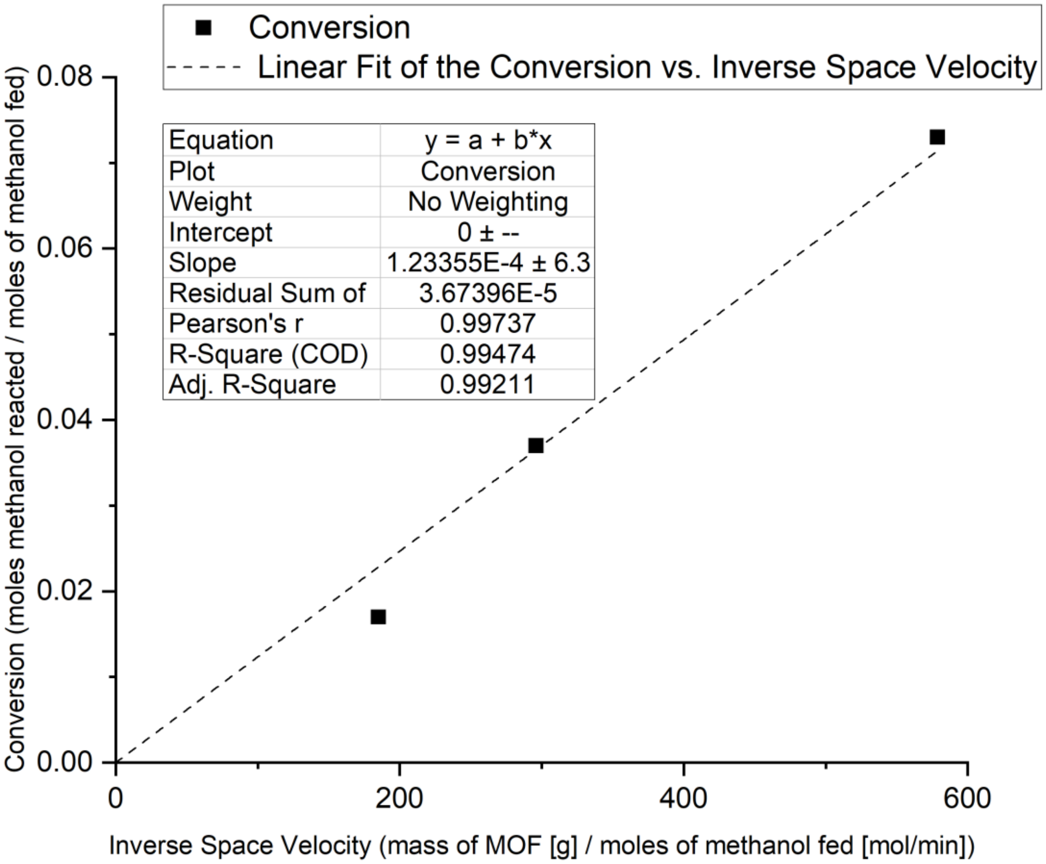

Figure A2.4. Differential conversion of methanol dehydration to dimethyl ether catalyzed by UiO-66aa30. Reaction conditions: 548 K, feed partial pressures: methanol, 220, helium, 780 mbar; total flow rate, 12.5 mL (NTP)/min; catalyst mass, varied between 20 and 50 mg MOF mixed with 1.00 g of particles of α-Al_2O_3.The linearity of this plot that passes through the origin demonstrates that the data determine rates (TOF values) directly as the slope of the line.

Analysis of catalytic reaction products: Chromatograms of methyl formate and methyl acetate.

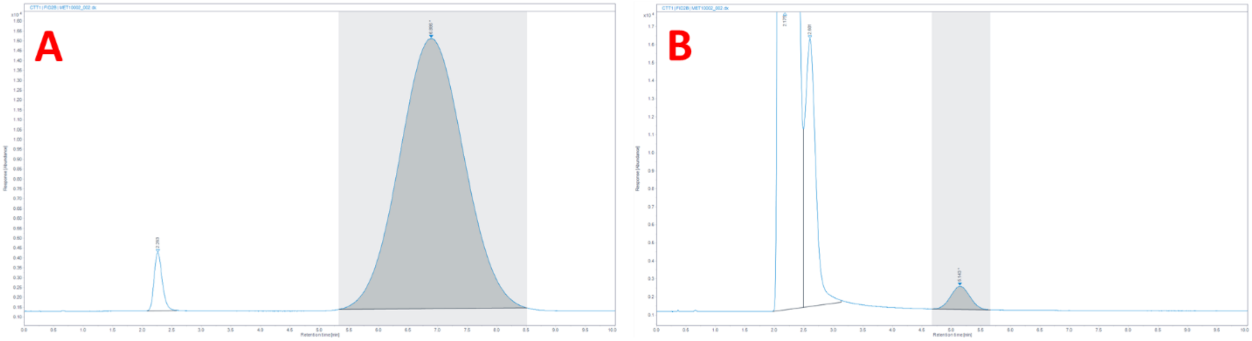

Figure A2.5. Chromatogram of methanol and methyl acetate signals as detected with retention times of 2.2 and 6.8 min respectively (A). Signal was generated by passing methyl acetate through an inert bed of 1.00 g of α-Al_2O_3 with an aliquot of the effluent gas stream pyrolyzed at the FID. Small amounts (<3% of signal) of methanol remained in the sparger and reactor components and are detected in this chromatogram. Chromatogram of products of methanol dehydration catalyzed by UiO-66aa30 demonstrating conversion at 10 min time on stream (B). The emergence of the peak at 5.14 min corresponds to methyl formate. This peak appears before the emergence of the peak for methyl acetate. Reaction conditions: 473 K, feed partial pressure, 220 mbar methanol and 780 mbar helium; total flow rate, 12.5 mL(NTP)/ min; catalyst mass, 50 mg MOF and 1.00 g α-Al_2O_3.

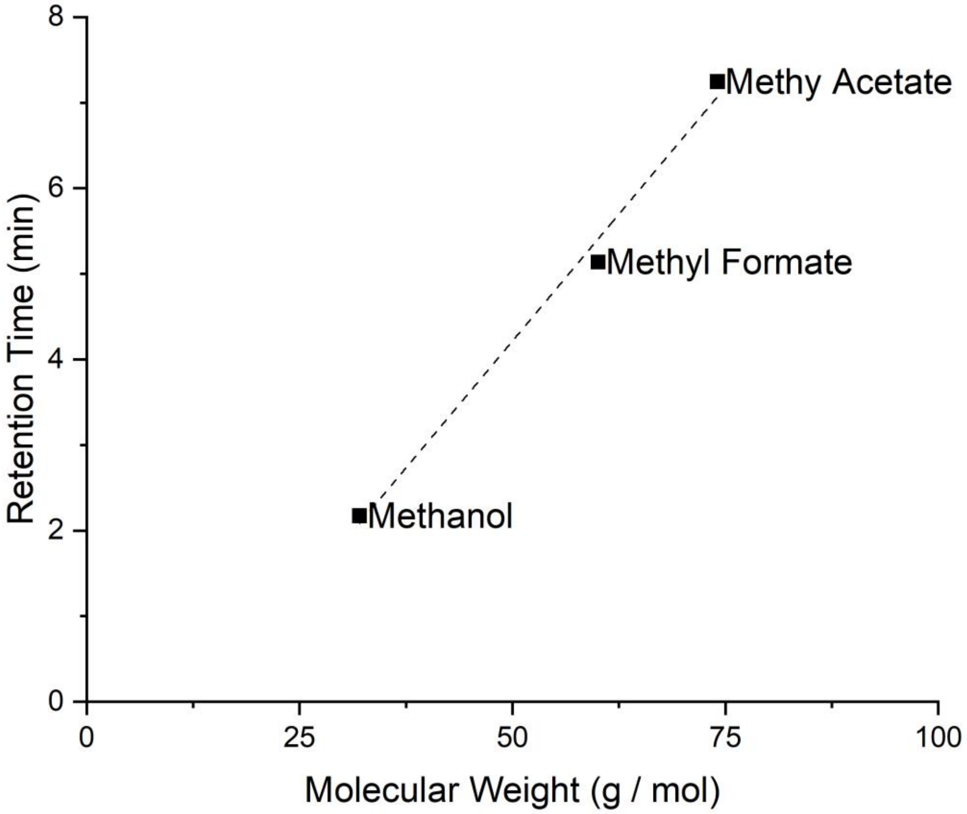

Figure A2.6. Relationship of the retention times in the GC column and molecular weights of methanol, methyl formate, and methyl acetate. The linear fit gives a slope of 0.12 ± 0.01, a y-intercept of -1.7 ± 0.6, and a R-squared value of 0.991.

Calculation of the rate of desorption of the alkyl esters methyl formate and methyl acetate.

Rates were calculated as follows: changes in numbers of carboxylate ligands were found from the mass balance data provided by the ^{1}H NMR analyses, which provided the numbers of mols at time on stream = 0 and time on stream = 45 min. These values were normalized to the total mass of catalyst digested, so that the value was amount of ligand changed per gram of catalyst. For the formate ligands, this value was divided by the time (45 min). However, the acetate began to leave the MOF 10 min after the formate began to leave. Depending on the amount of acetate removed, the process took from 12 to 35 min; these were the times used to determine the approximate rate. These carboxylates were all largely removed by 45 min on stream, which is the time when the acetate had been almost completely removed. The rates at which the ligands were removed from the MOFs were close to each other, and perhaps almost independent of their relative amounts on the MOF nodes.

Catalyst Activation by Removal of Methyl Acetate and Methyl Formate at 548 K.

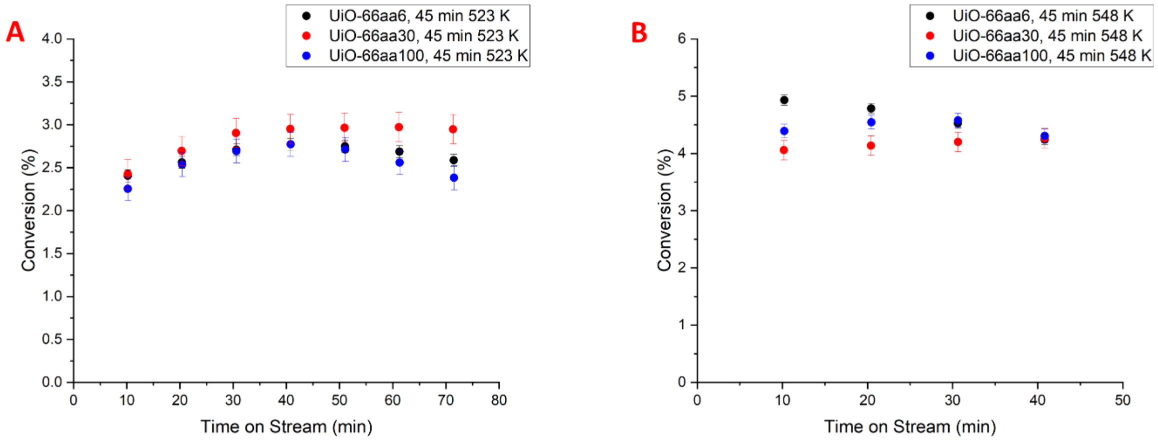

Figure A2.7. Catalytic performance of MOF UiO-66 samples during the first 45 min of catalytic conversion of methanol. Reaction conditions: 523 K (A) and 548 K (B), feed partial pressures: 220 mbar of methanol and 780 mbar of helium; total feed flow rate 12.5 mL (NTP)/min; catalyst mass, 25 mg of MOF particles mixed with 1.00 g of particles of α-Al_2O_3. Error bars correspond to standard errors that were determined from four repeat catalysis experiments.

At 523 K periods of increasing conversion are evident for all three MOFs. In contrast, at 548 K periods of increasing conversion are evident for UiO-66aa30 and UiO-66100, but no such activation period was observed for UiO-66aa6 which is inferred to have undergone activation prior to analysis of the first product sample. This behavior is likely explained by UiO-66aa6's having significantly less acetate bonded, as shown by the desorption of methyl formate and methyl acetate and by the ^{1}H NMR analysis.

Alumina particles in the SEM images.

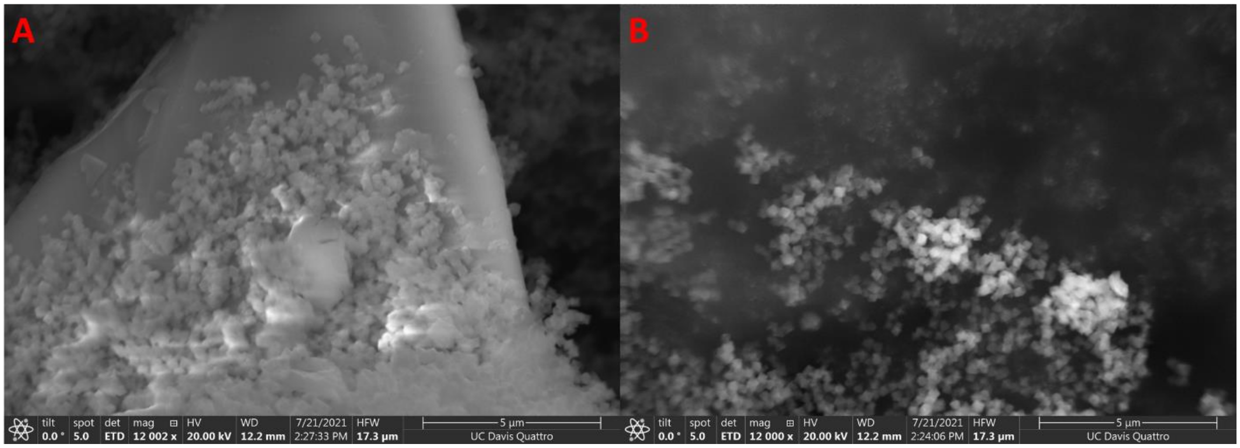

Figure A2.8. Comparison of UiO-66aa100 on the surface of a much larger particle of α-Al_2O_3 (A) and of the MOF in between the particles of α-Al_2O_3. The MOF particle diameters are approximately 350 ± 33 nm, averaged over 100 measured particles, and are not significantly different between the two images.

Example of the extrapolation of differential conversion data to calculate initial rates.

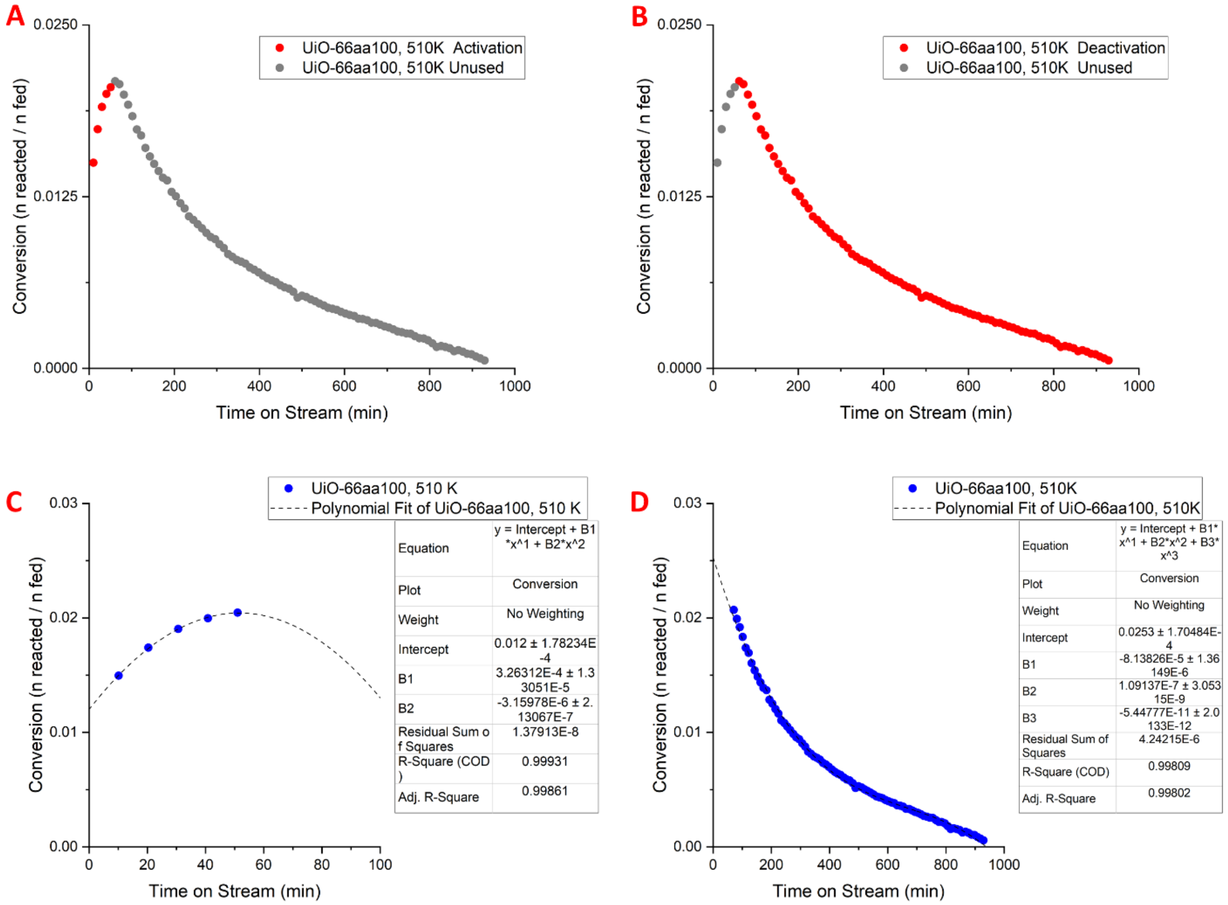

Equation	y = Intercept + B1 *x^1 + B2*x^2
Plot	Conversion
Weight	No Weighting
Intercept	0.012 ± 1.78234E -4
B1	3.26312E-4 ± 1.3 3051E-5
B2	-3.15978E-6 ± 2. 13067E-7
Residual Sum o f Squares	1.37913E-8
R-Square (COD)	0.99931
Adj. R-Square	0.99861

Equation	y = Intercept + B1* x^1 + B2*x^2 + B3* x^3
Plot	Conversion
Weight	No Weighting
Intercept	0.0253 ± 1.70484E- 4
B1	-8.13826E-5 ± 1.36 149E-6
B2	1.09137E-7 ± 3.053 15E-9
B3	-5.44777E-11 ± 2.0 133E-12
Residual Sum of Squares	4.24215E-6
R-Square (COD)	0.99809
Adj. R-Square	0.99802

Figure A2.9. Analysis of the kinetics of the catalytic dehydration of methanol to dimethyl ether by UiO-66aa100 at 510 K. The data selected for analysis of the activation of the MOF (A) and the deactivation of the MOF (B) are separated by the maximum of the conversion vs. time on stream data sets and are highlighted in red. The extrapolation of the conversion vs. time on stream data characterizing the activation data was fit to order-2 polynomial functions, with the y-intercept giving the initial differential conversion (C). The extrapolation for the deactivation data was fit to an order-3 polynomial function (D). The initial differential conversion was multiplied by the space velocity (molecular feed rate of reactant methanol/the mass of catalyst) to obtain the rate. Reaction conditions: 510 K, feed partial pressures: 220 mbar methanol and 780 mbar helium; total feed flow rate 12.5 mL (NTP)/min; catalyst mass, 25 mg of MOF mixed with 1.00 g of α-Al_2O_3.

Arrhenius Plots showing the Estimated Initial Rates.

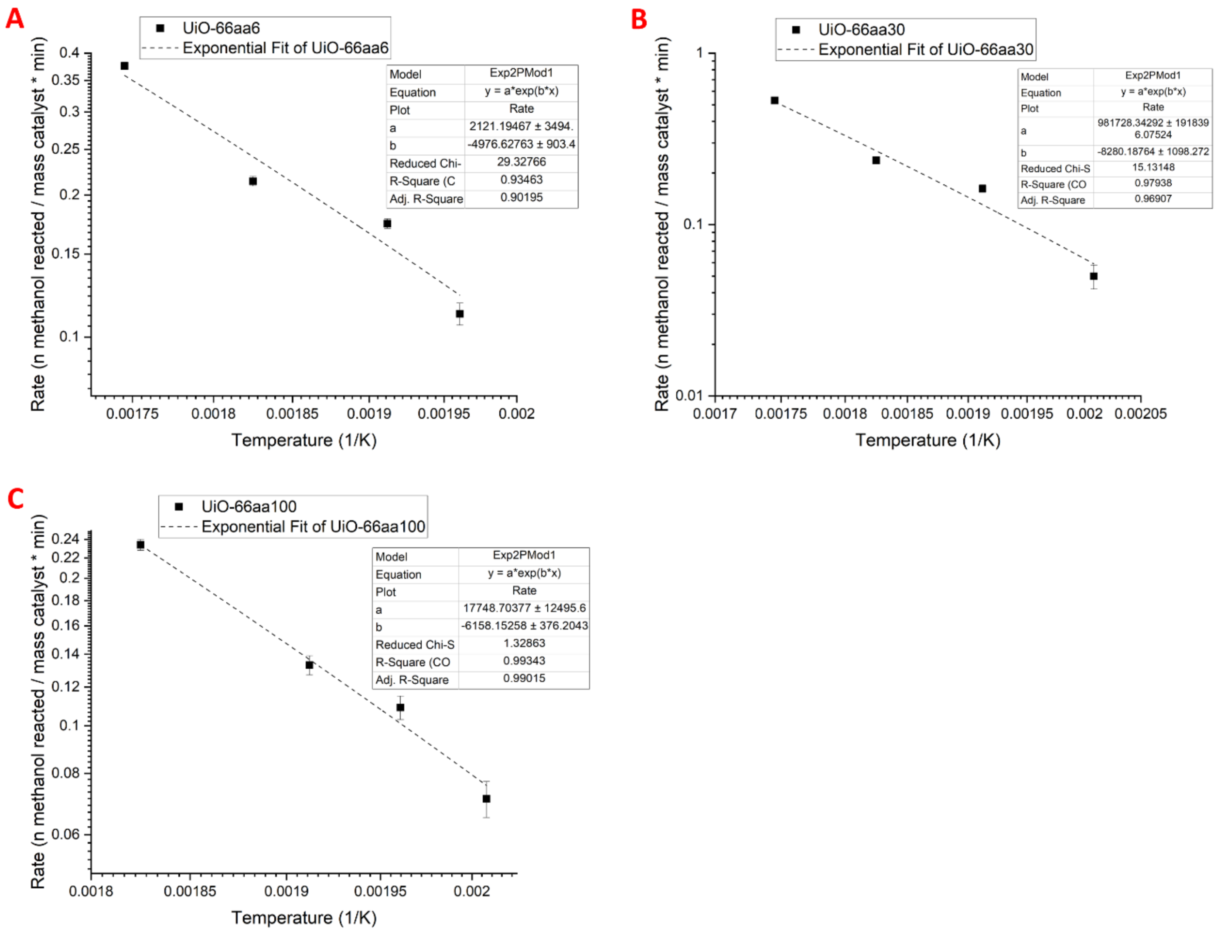

Model	Exp2PMod1
Equation	y = a*exp(b*x)
Plot	Rate
a	2121.19467 ± 3494.
b	-4976.62763 ± 903.4
Reduced Chi-	29.32766
R-Square (C	0.93463
Adj. R-Square	0.90195

Model	Exp2PMod1
Equation	y = a*exp(b*x)
Plot	Rate
a	981728.34292 ± 191839 6.07524
b	-8280.18764 ± 1098.272
Reduced Chi-S	15.13148
R-Square (CO	0.97938
Adj. R-Square	0.96907

Model	Exp2PMod1
Equation	y = a*exp(b*x)
Plot	Rate
a	17748.70377 ± 12495.6
b	-6158.15258 ± 376.2043
Reduced Chi-S	1.32863
R-Square (CO	0.99343
Adj. R-Square	0.99015

Figure A2.10. Arrhenius plots of the initial rates to determine the apparent activation energies of the methanol dehydration reaction for UiO-66aa6 (A), UiO-66aa30 (B), and UiO-66aa100(C).

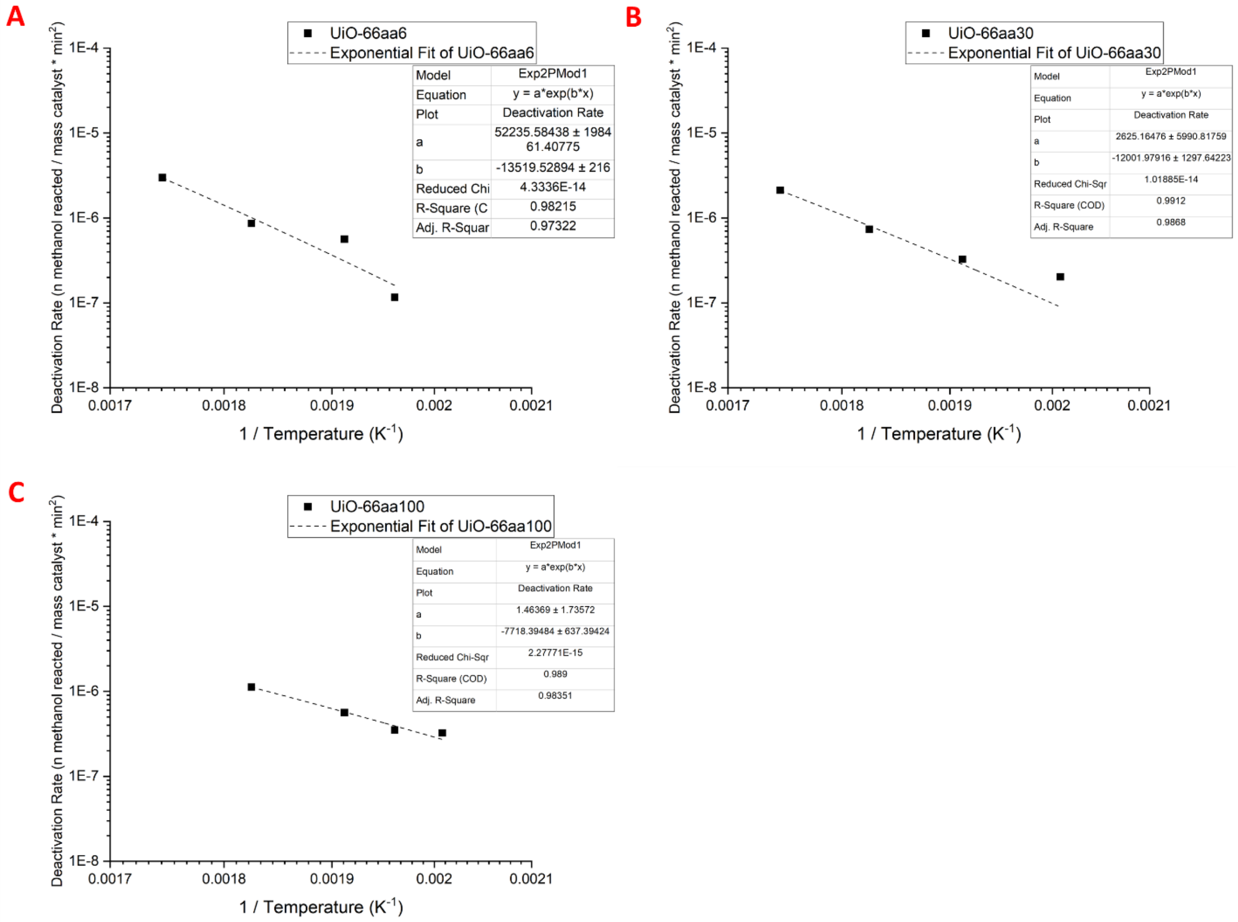

Model	Exp2PMod1
Equation	y = a*exp(b*x)
Plot	Deactivation Rate
a	52235.58438 ± 1984 61.40775
b	-13519.52894 ± 216
Reduced Chi	4.3336E-14
R-Square (C	0.98215
Adj. R-Squar	0.97322

Model	Exp2PMod1
Equation	y = a*exp(b*x)
Plot	Deactivation Rate
a	2625.16476 ± 5990.81759
b	-12001.97916 ± 1297.64223
Reduced Chi-Sqr	1.01885E-14
R-Square (COD)	0.9912
Adj. R-Square	0.9868

Model	Exp2PMod1
Equation	y = a*exp(b*x)
Plot	Deactivation Rate
a	1.46369 ± 1.73572
b	-7718.39484 ± 637.39424
Reduced Chi-Sqr	2.27771E-15
R-Square (COD)	0.989
Adj. R-Square	0.98351

Figure A2.11. Arrhenius plots of the initial rates to determine the apparent activation energies of the deactivation rate of UiO-66aa6 (A), UiO-66aa30 (B), and UiO-66aa100(C).

Relationship between conversion and material properties

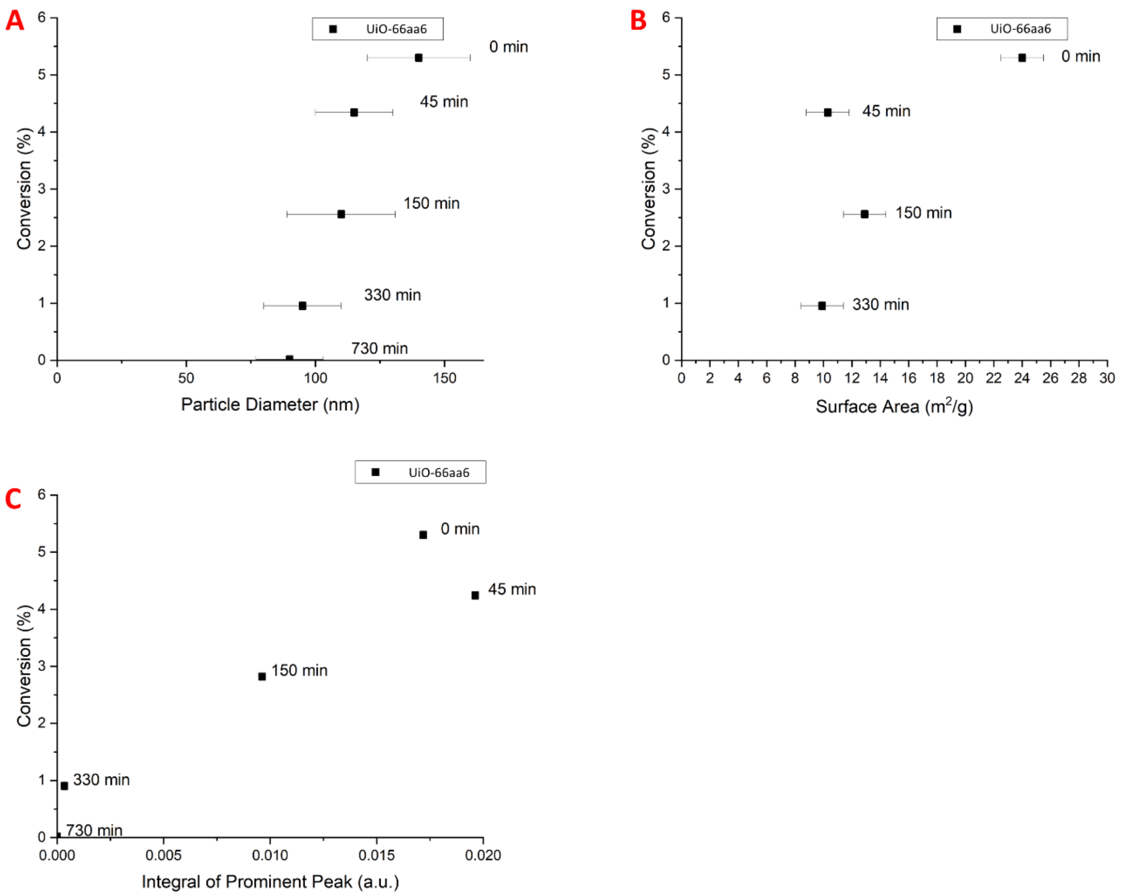

Figure A2.12. Degradation of MOF UiO-66aa6 demonstrating the correlation between loss of catalytic activity and MOF structure as characterized by the particle diameter (A), surface area (B), and loss of crystallinity quantified by the integral of the characteristic peak of UiO-66 at 2θ = 7.45 (C). Values for conversion were averaged across experiments when multiple runs were available.

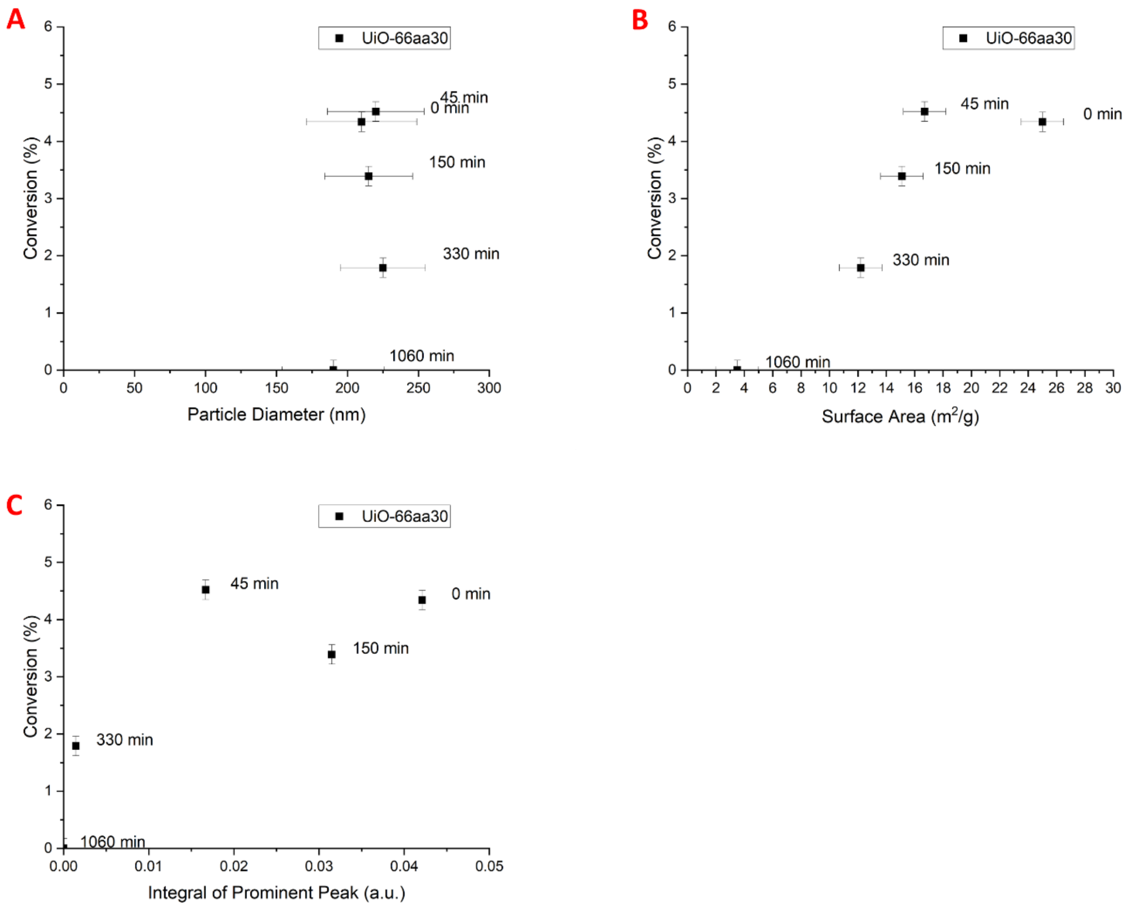

Figure A2.13. Degradation of MOF UiO-66aa30 demonstrating the correlation between loss of catalytic activity and MOF structure as characterized by the particle diameter (A), surface area (B), and loss of crystallinity quantified by the integral of the characteristic peak of UiO-66 at 2θ = 7.45 (C). Values for conversion were averaged across experiments when data from multiple runs were available.

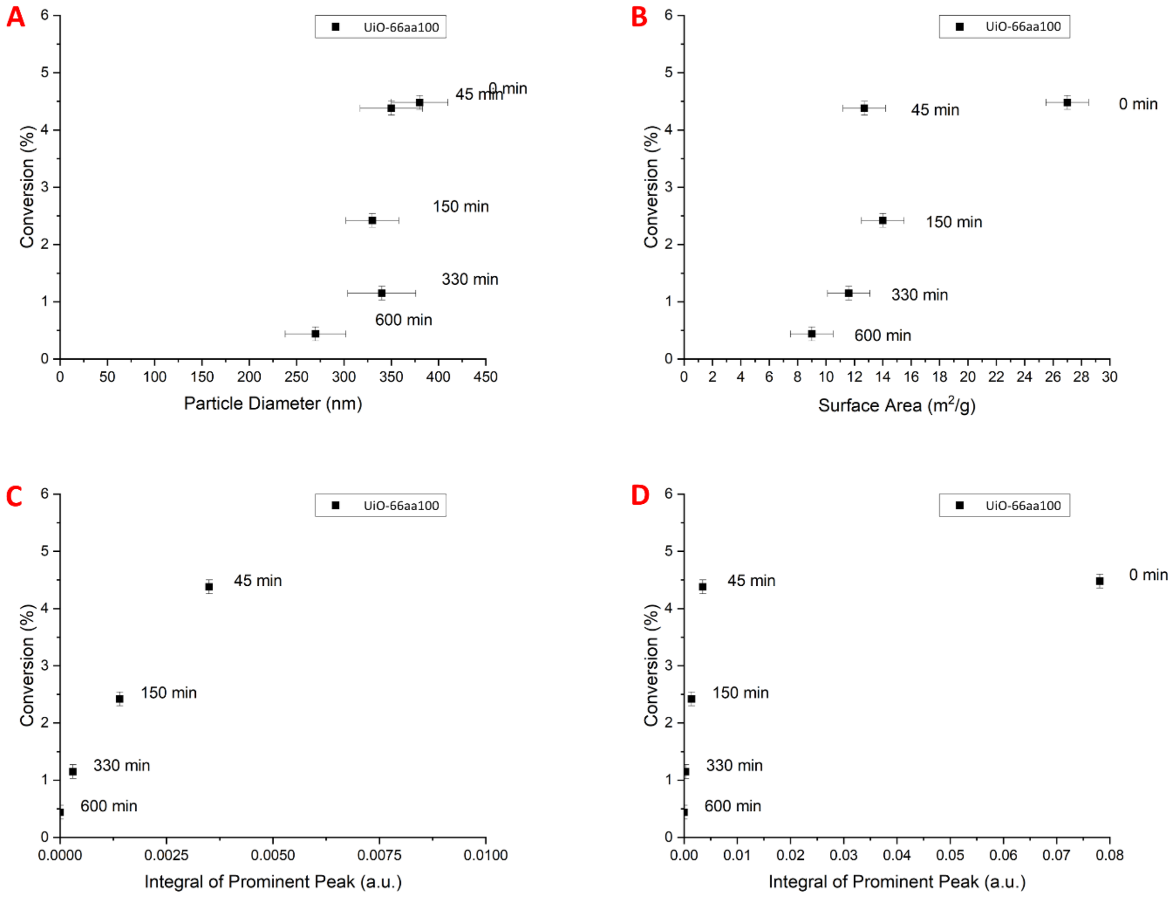

Figure A2.14. Degradation of MOF UiO-66aa30 demonstrating the correlation between loss of catalytic activity and MOF structure as characterized by the particle diameter (A), surface area (B), and loss of crystallinity quantified by the integral of the characteristic peak of UiO-66 at 2θ = 7.45 (C,D). Values for conversion were averaged across experiments when multiple runs were available.

Relationship between methanol conversion and MOF catalyst particle sizes.

The loss of particle sizes of UiO-66aa6, UiO-66aa30, and UiO-66aa100 correlate with the loss in conversion, which is expected because both decrease with time exposed to reaction conditions. However, the particles of UiO-66aa6, UiO-66aa30, and UiO-66aa100 were not completely digested by the end of the reaction, as conversion reached zero while the particle diameters remained approximately 60, 90, and 80 % of their initial values. UiO-66aa6 is the only

MOF in this work that decreased in particle size in line with the conversion. UiO66-aa30 and UiO66-aa100 did not show a consistent pattern of decrease in particle size with conversion.

Relationship between conversion and MOF surface area.

During the activation process, UiO-66aa6, UiO-66aa30, and UiO-66aa100 experienced a severe drop in surface area upon exposure to reaction conditions, as shown by the difference between the measurements at time on stream = 0 and 45 min, decreasing by 43, 33, and 53 %, respectively, with only slight (< 1%) changes in conversion. For UiO-66aa30, the change in conversion is positive because of its longer period of activation. As the conversion decreased, the change in surface area had a general decreasing trend, but with changes that were difficult to quantify when considering the experimental error. Following the trend of surface area with conversion for each MOF to 0 %, the trends arrive at a surface area of approximately 8 $m^2 g^{-1}$. The exception to this is the surface area measurement of UiO-66aa30 at 1060 min time on stream, characterized by a measurement of 3.5 ± 1.5 $m^2 g^{-1}$. The data characterizing UiO-66aa30 also most consistently gave evidence of a pattern of decreased surface area with decreasing conversion.

Relationship between conversion and MOF crystallinity.

The crystallinity of each MOF decreased with increasing time on stream as evidenced by the PXRD patterns and characterized by the loss of intensity at $2\theta = 7.45°$. This loss was the most rapid for UiO-66aa100, for which the decrease was more than 95% with negligible loss in conversion. After the initial loss in crystallinity, the measured area under the peak at $2\theta = 7.45°$ for UiO-66aa100 reached essentially zero with a conversion of 4.5%. UiO-66aa6 and UiO-66aa30 did undergo the rapid loss of crystallinity as shown for UiO-66aa100. Furthermore, there is scatter in the conversion/crystallinity data for UiO-66aa6 and UiO-66aa30 that challenges a quantitative assessment of the rate of loss of conversion and its correlation with the crystallinity. UiO-66aa6 and UiO66aa1.0 approached 0.8 and 1.5% methanol conversion, respectively, as the peak area approached zero.

Accounting and rationale for the allotment of recovered samples.

The recovered catalyst bed after each exposure to reaction conditions (45 min, 150 min, 330 min, and at a time that fully captured the deactivated MOF) consisted of about 975 mg of α-Al_2O_3 and 25 mg of MOF. The samples were characterized with PXRD, SEM, and ^{1}H NMR spectroscopy of samples digested for 24 h in 1.00-*M* NaOH in D_2O, and BET N_2 adsorption isotherms. An allotment of 100 mg of sample was used each of the four tests. This left 600 mg of sample for repeat experiments, which were used to confirm results and methodology, and allowed for at least one repeat experiment for each characterization method.

Reactor design for the once-through plug flow reactor

Figure A2.15. Image taken of reactor constructed by the author and used for experimentation.

The once-through tubular plug flow reactor was constructed out of stainless steel (s.s.) tubing and compression fittings. The catalyst bed was supported by a stainless steel frit that was positioned in the ¼” s.s. adapter in the center of the reactor. The inlet, at the top of image A2.15, and the outlet, facing right at the bottom of image A2.15, were sealable with 1-way valves which allowed for transfer of the reactor between the gas-flow manifold and the glovebox without exposure of the catalyst bed to atmosphere. The catalyst bed was loaded in the glove box with a funnel at the top of the reactor by disconnecting the ¼” tube from the ¼” to ½” adapter piece just below the inlet valve. Following sample recovery, the reactor was removed from the glovebox and the ¼” tube that held the catalyst sample and center adapter were cleaned with house-air before the next experiment. The K-type thermocouple was fed though the bottom of the reactor with the tip positioned just below the stainless steel frit that supported the catalyst bed. The reactor pieces needed to be replaced periodically during experimentation as the compression fittings and tubing were worn from repeated use. In particular, the tube and adapter that were removed for routine cleaning after each experiment needed to be replaced approximately once every two months to avoid leaking from the reactor as compression fittings degraded.

When positioning the reactor in the furnace care was taken to wrap many lines of insulating tape around the reactor to help maintain isothermal conditions and good contact with the furnace walls. Heating lines placed after the reactor, necessary to prevent condensation in the effluent gas stream, can slowly destroy the outlet valve and the O-ring of the thermocouple adapter, so it is important to test these pieces periodically for damage. The best method for this is to measure the outlet flow rate before experiments each day to verify there are no leaks.

References

(1) Wei, R.; Gaggioli, C. A.; Li, G.; Islamoglu, T.; Zhang, Z.; Yu, P.; Farha, O. K.; Cramer, C. J.; Gagliardi, L.; Yang, D.; Gates, B. C. Tuning the Properties of Zr_6O_8 Nodes in the Metal- Organic Framework UiO-66 by Selection of Node-Bound Ligands and Linkers. *Chem. Mater.* **2019**, *31*, 1655–1663.

(2) Yang, D.; Gaggioli, C. A.; Ray, D.; Babucci, M.; Gagliardi, L.; Gates, B. C. Tuning Catalytic Sites on Zr_6O_8 Metal–Organic Framework Nodes via Ligand and Defect Chemistry Probed with *tert*-Butyl Alcohol Dehydration to Isobutylene. *J. Am. Chem. Soc.* **2020**, *142*, 8044–8056.

(3) Yang, D.; Ortuño, M. A.; Bernales, V.; Cramer, C. J.; Gagliardi, L.; Gates, B. C. Structure and Dynamics of Zr_6O_8 Metal–Organic Framework Node Surfaces Probed with Ethanol Dehydration as a Catalytic Test Reaction. *J. Am. Chem. Soc.* **2018**, *140*, 3751–3759.

(4) Cavka, J. H.; Jakobsen, S.; Olsbye, U.; Guillou, N.; Lamberti, C.; Bordiga, S.; Lillerud, K. P. A New Zirconium Inorganic Building Brick Forming Metal Organic Frameworks with Exceptional Stability. *J. Am. Chem. Soc.* **2008**, *130*, 13850–13851.

(5) Schaate, A.; Roy, P.; Godt, A.; Lippke, J.; Waltz, F.; Wiebcke, M.; Behrens, P. Modulated Synthesis of Zr-Based Metal-Organic Frameworks: From Nano to Single Crystals. *Chem. Eur. J.* **2011**, *17*, 6643–6651.

(6) Liu, N.; Shi, L.; Meng, X. Tuning the Adsorption Properties of UiO-66 *via* Acetic Acid Modulation. *J. Chem. Sci.* **2019**, *131*, 50.

(7) Morris, W.; Wang, S.; Cho, D.; Auyeung, E.; Li, P.; Farha, O. K.; Mirkin, C. A. Role of Modulators in Controlling the Colloidal Stability and Polydispersity of the UiO-66 Metal–Organic Framework. *ACS Appl. Mater. Interf.* **2017**, *9*, 33413–33418.

Appendix Chapter 3

Characterization of UiO-66 under catalysis for isopropanol dehydration.

Analysis of catalytic reaction products: Chromatograms of isopropanol, diisopropyl ether, propyl formate and propyl acetate.

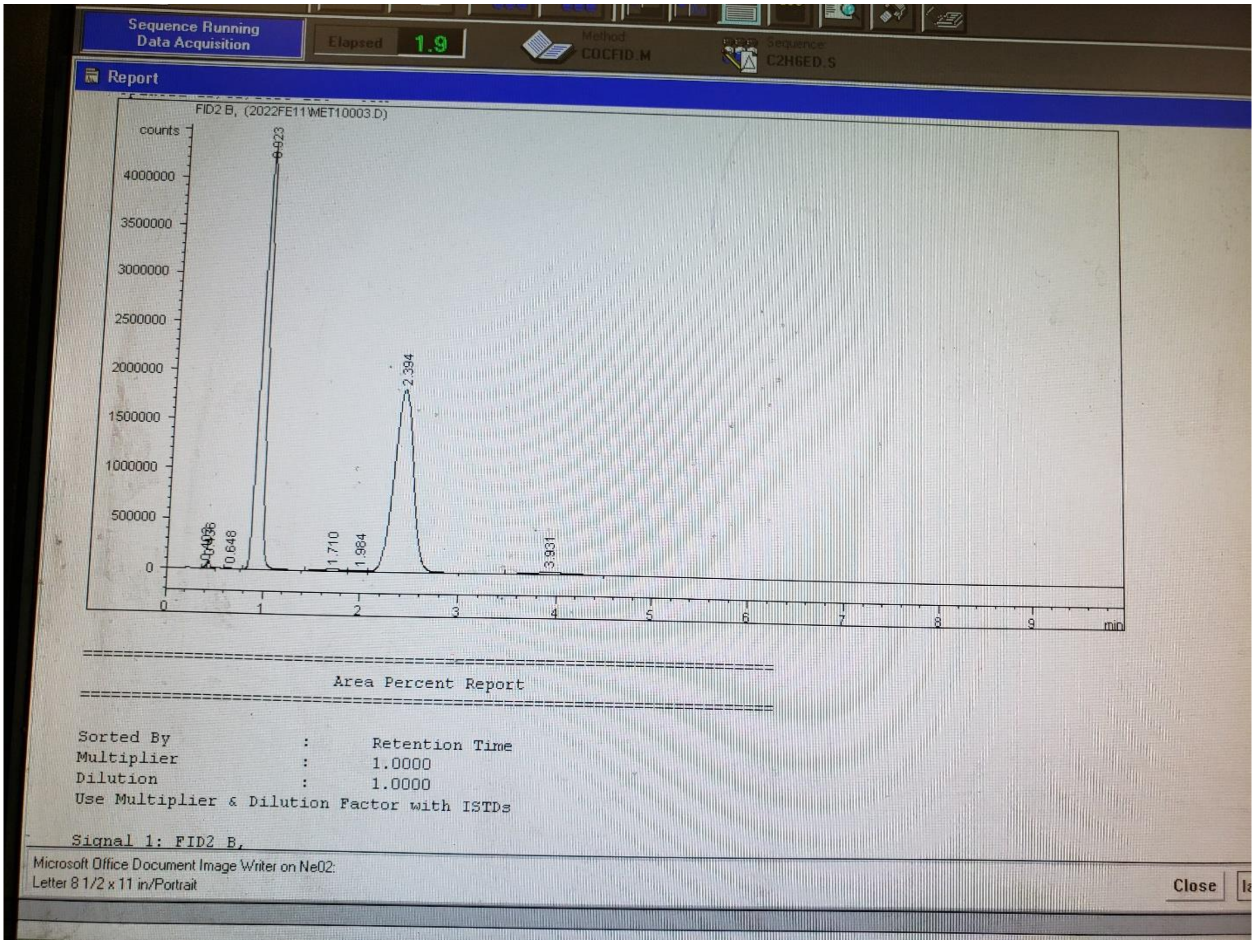

```
=====================================================================
                        Area Percent Report
=====================================================================

Sorted By              :      Retention Time
Multiplier             :      1.0000
Dilution               :      1.0000
Use Multiplier & Dilution Factor with ISTDs

Signal 1: FID2 B,
```

Figure A3.1. Chromatogram of isopropanol and diisopropyl ether signals as detected with retention times of 0.923 and 2.394 min respectively. Signal was generated by passing isopropanol and diisopropyl ether through an inert bed of 1.00 g of α-Al_2O_3 with an aliquot of the effluent gas stream pyrolyzed at the FID.

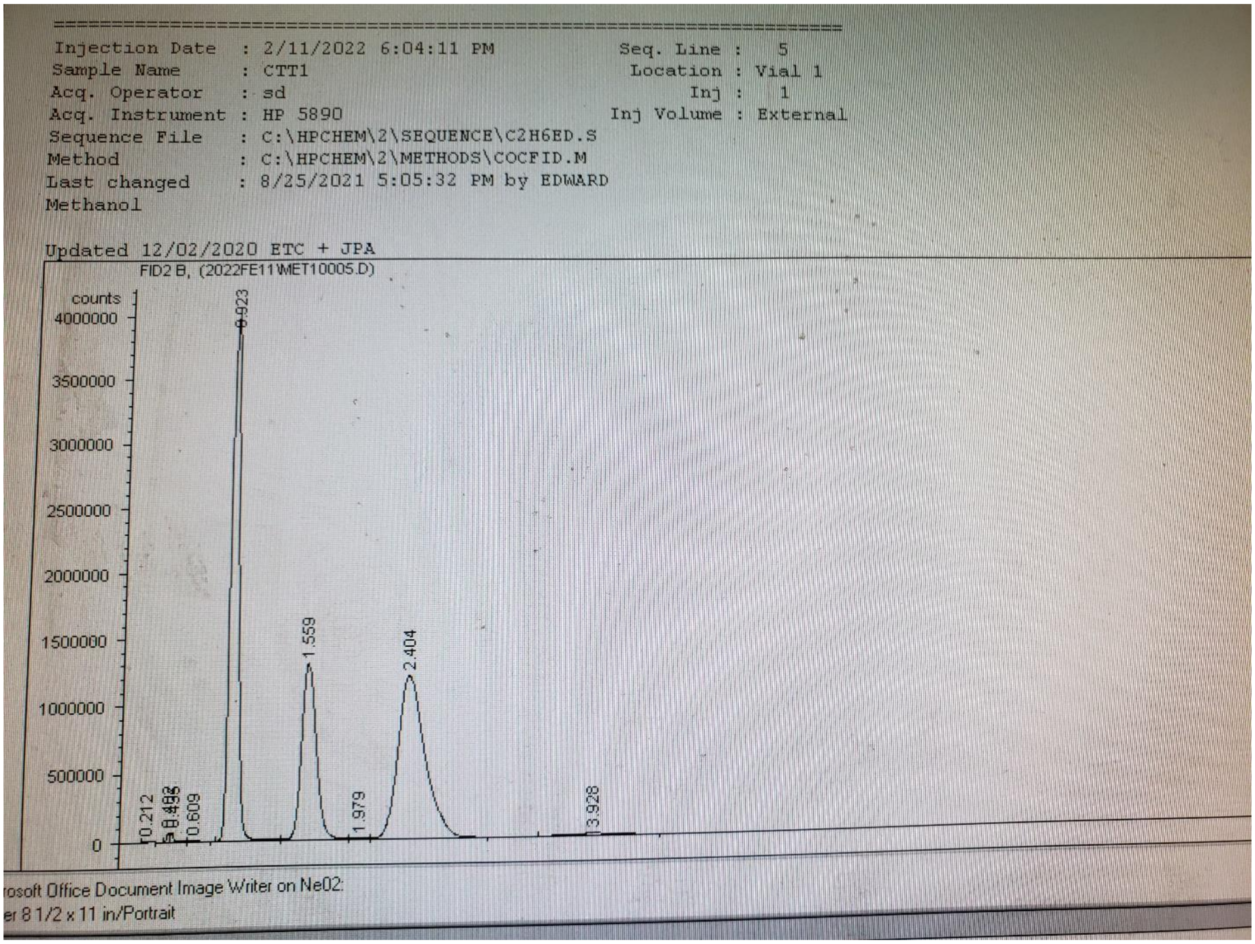

```
=====================================================================
 Injection Date  : 2/11/2022 6:04:11 PM          Seq. Line :   5
 Sample Name     : CTT1                           Location : Vial 1
 Acq. Operator   : sd                                  Inj :   1
 Acq. Instrument : HP 5890                      Inj Volume : External
 Sequence File   : C:\HPCHEM\2\SEQUENCE\C2H6ED.S
 Method          : C:\HPCHEM\2\METHODS\COCFID.M
 Last changed    : 8/25/2021 5:05:32 PM by EDWARD
 Methanol

 Updated 12/02/2020 ETC + JPA
```

rosoft Office Document Image Writer on Ne02:
er 8 1/2 x 11 in/Portrait

Figure A3.2. Chromatogram of isopropanol, isopropyl formate, and isopropyl acetate signals as detected with retention times of 0.923, 1.559, and 2.404 min respectively. Signal was generated by passing isopropanol, isopropyl formate, and isopropyl acetate through an inert bed of 1.00 g of α-Al_2O_3 with an aliquot of the effluent gas stream pyrolyzed at the FID.

Isopropanol Dehydration Maintained after 15 hours on Stream.

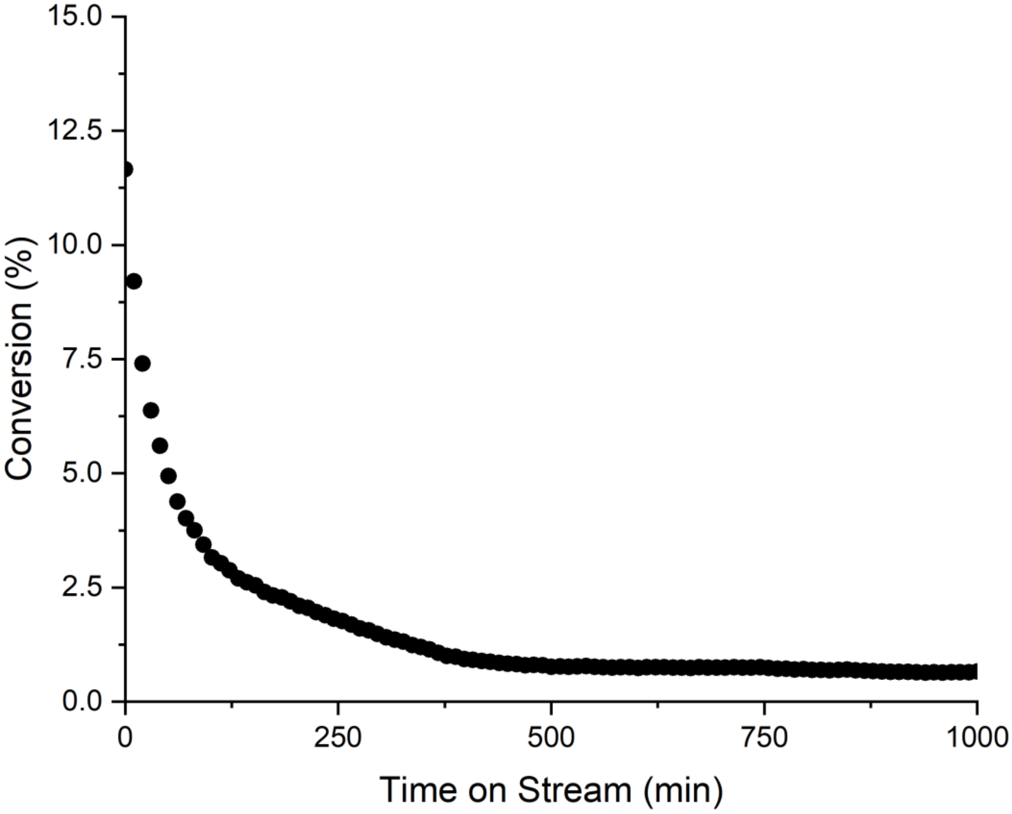

Figure A3.3. Conversion of isopropanol to propylene and diisopropyl ether catalyzed by UiO-66aa30 at 548 K after 15 hours of time on stream. After the first 10 hours, the system appears to be in steady-state hovering at approximately 0.6% conversion. This behavior was observed for all MOFs studied in this work for isopropanol dehydration, with the terminal stage of the MOF holding at steady state conversions of < 1%. Reaction conditions: 473 K, feed partial pressure of 80 mbar of isopropanol and 920 mbar of helium; total flow rate 12.5 mL (NTP)/ min; catalyst mass, 25 mg of MOF and 1.00 g of α-Al_2O_3 particles mixed with mortar and pestle for 60 *s.*

Loss of Activation of Conversion with Temperature

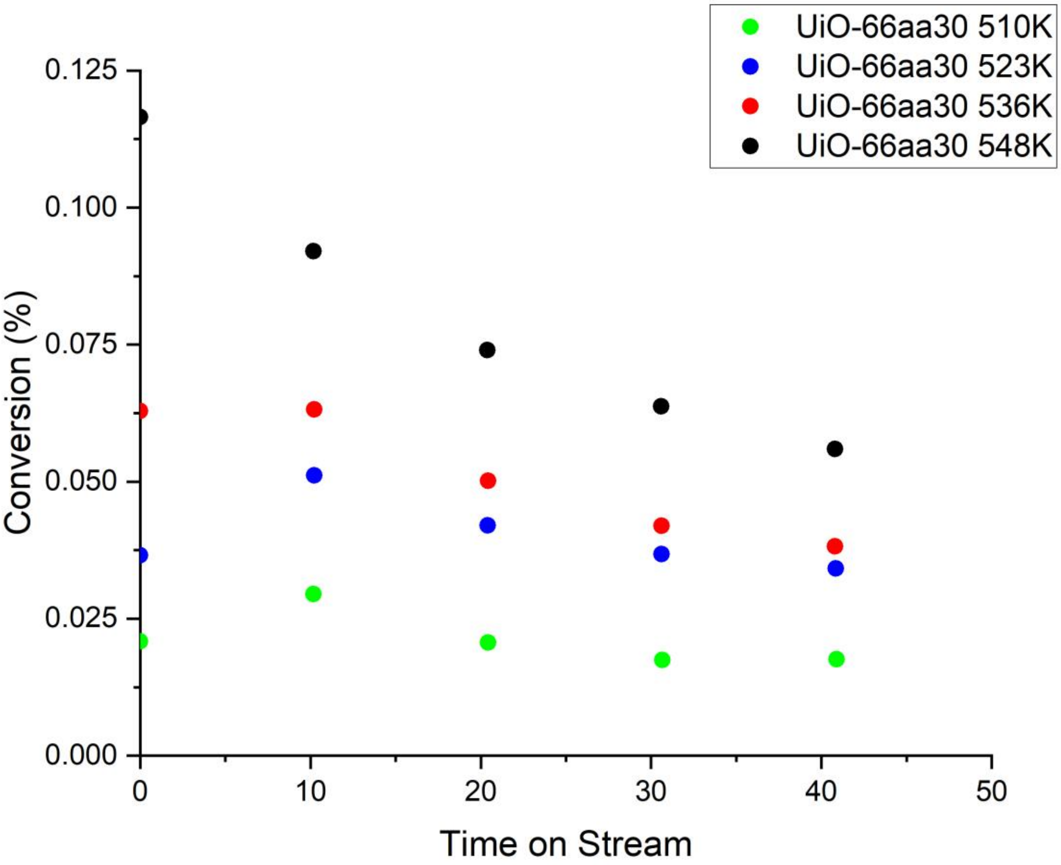

Figure A3.4. Conversion of isopropanol to propylene and diisopropyl ether catalyzed by UiO-66aa30 at temperatures ranging from 510-548 K in the first 45 minutes of time on stream. Activation of the conversion is observed at 510, 523, slightly at 536 K, and with no activation profile observed at 548 K demonstrating the decrease in the prevalence of the activation step as temperature increases. Reaction conditions: 510, 523, 536, and 548 K, feed partial pressure of 80 mbar of isopropanol and 920 mbar of helium; total flow rate 12.5 mL (NTP)/ min; catalyst mass, 25 mg of MOF and 1.00 g of α-Al_2O_3 particles mixed with mortar and pestle for 60 s.

Extrapolation of the Catalysis Reaction Data to Determine the Initial Reaction Rate and Deactivation Rate

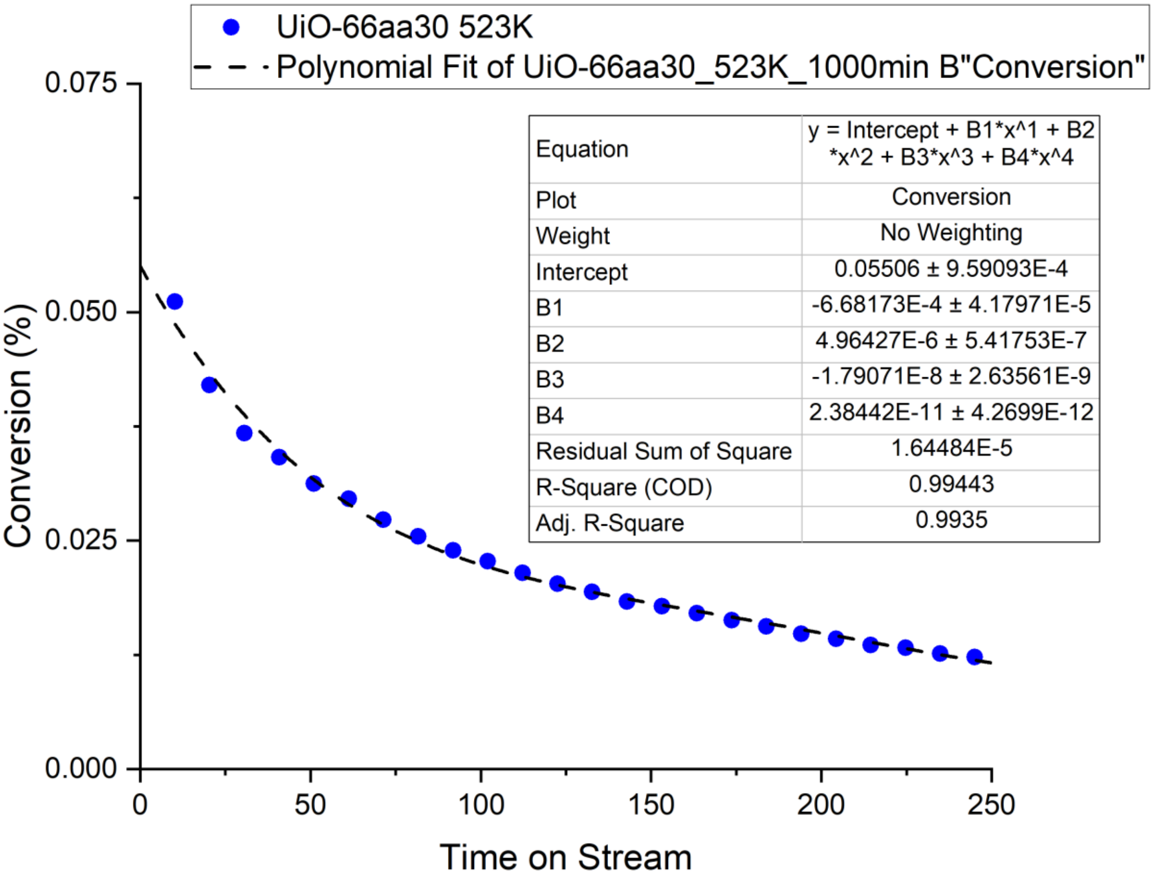

Equation	y = Intercept + B1*x^1 + B2 *x^2 + B3*x^3 + B4*x^4
Plot	Conversion
Weight	No Weighting
Intercept	0.05506 ± 9.59093E-4
B1	-6.68173E-4 ± 4.17971E-5
B2	4.96427E-6 ± 5.41753E-7
B3	-1.79071E-8 ± 2.63561E-9
B4	2.38442E-11 ± 4.2699E-12
Residual Sum of Square	1.64484E-5
R-Square (COD)	0.99443
Adj. R-Square	0.9935

Figure A3.5. Analysis of the kinetics of the catalytic dehydration of methanol to dimethyl ether by UiO-66aa30 at 523 K. The extrapolation for the deactivation data was fit to an order-3 polynomial function (B). The initial differential conversion was multiplied by the space velocity (molecular feed rate of reactant methanol/the mass of catalyst) to obtain the rate. Reaction conditions: 523 K, feed partial pressures: 80 mbar isopropanol and 920 mbar helium; total feed flow rate 12.5 mL (NTP)/min; catalyst mass, 25 mg of MOF mixed with 1.00 g of α-Al_2O_3.

Arrhenius Plots showing the Estimated Initial Rates.

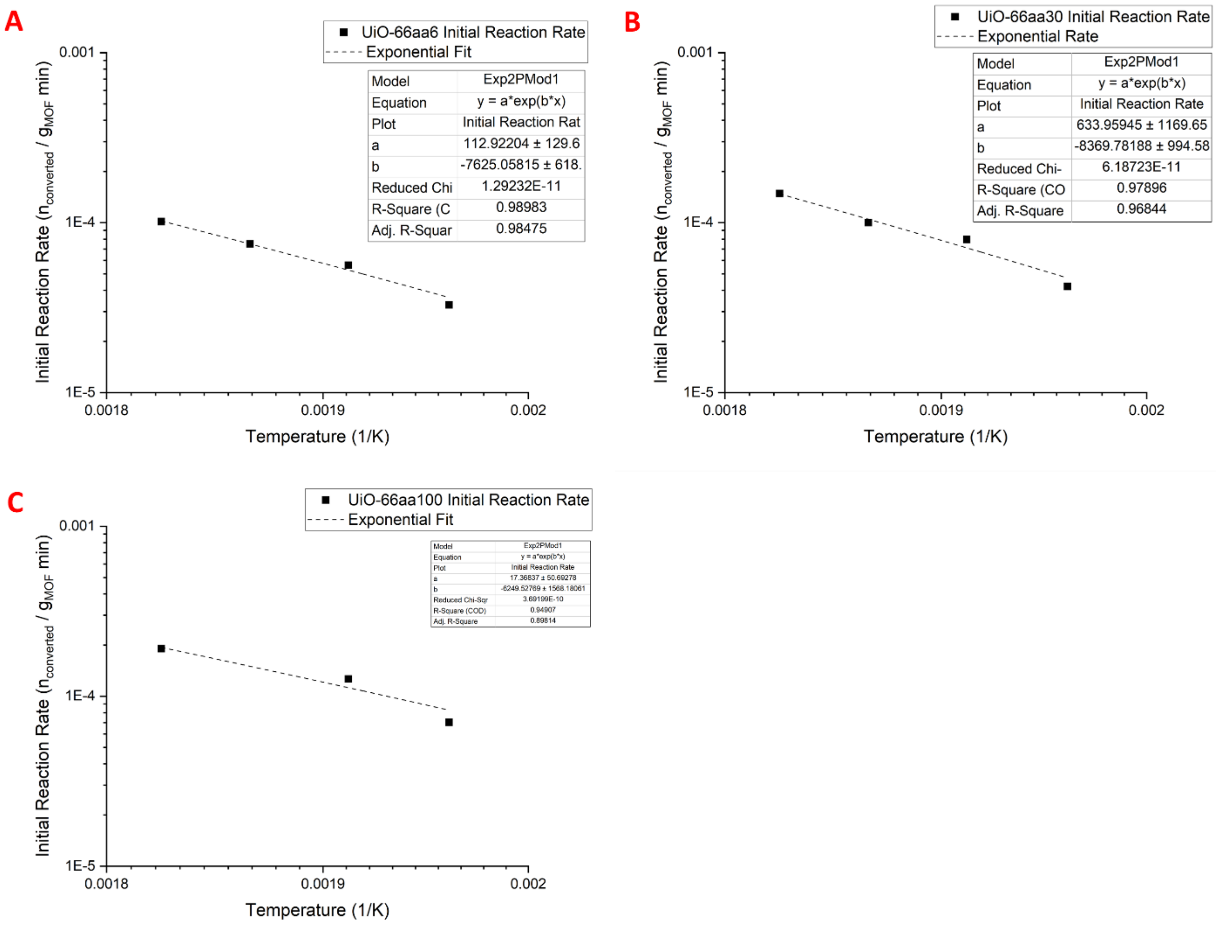

Figure A3.6. Arrhenius plots of the initial rates to determine the apparent activation energies of the isopropanol dehydration reaction for UiO-66aa6 (A), UiO-66aa30 (B), and UiO-66aa100(C).

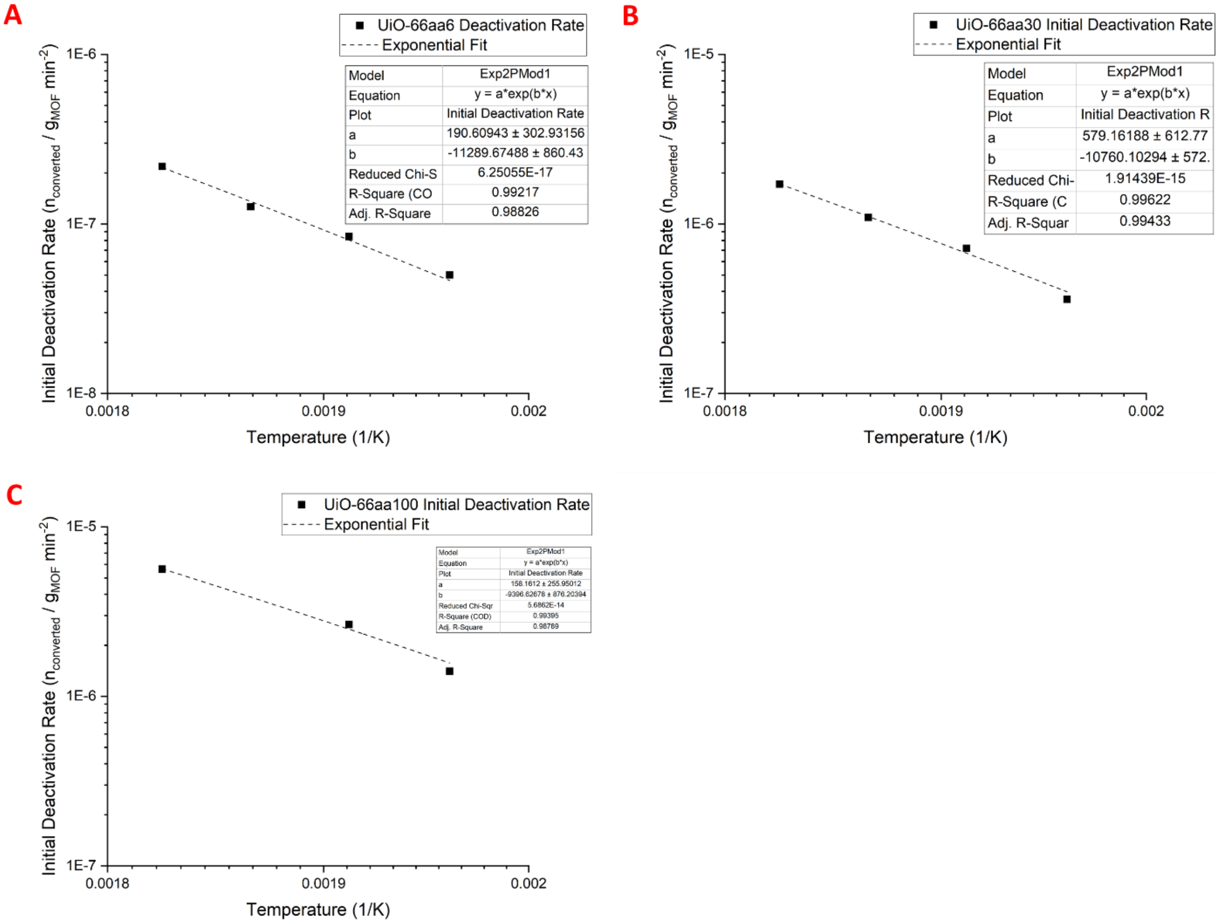

Model	Exp2PMod1
Equation	y = a*exp(b*x)
Plot	Initial Deactivation Rate
a	190.60943 ± 302.93156
b	-11289.67488 ± 860.43
Reduced Chi-S	6.25055E-17
R-Square (CO	0.99217
Adj. R-Square	0.98826

Model	Exp2PMod1
Equation	y = a*exp(b*x)
Plot	Initial Deactivation R
a	579.16188 ± 612.77
b	-10760.10294 ± 572.
Reduced Chi-	1.91439E-15
R-Square (C	0.99622
Adj. R-Squar	0.99433

Model	Exp2PMod1
Equation	y = a*exp(b*x)
Plot	Initial Deactivation Rate
a	158.1612 ± 255.95012
b	-9396.62678 ± 876.20394
Reduced Chi-Sqr	5.6862E-14
R-Square (COD)	0.99395
Adj. R-Square	0.98789

Figure A3.7. Arrhenius plots of the initial rates to determine the apparent activation energies of the deactivation rate of UiO-66aa6 (A), UiO-66aa30 (B), and UiO-66aa100(C).

Relationship between Catalytic Conversion and Catalytic Selectivity for Isopropanol Dehydration by UiO-66aa6, UiO-66aa30, and UiO-66aa100 during the first 400 minutes of Time on Stream.

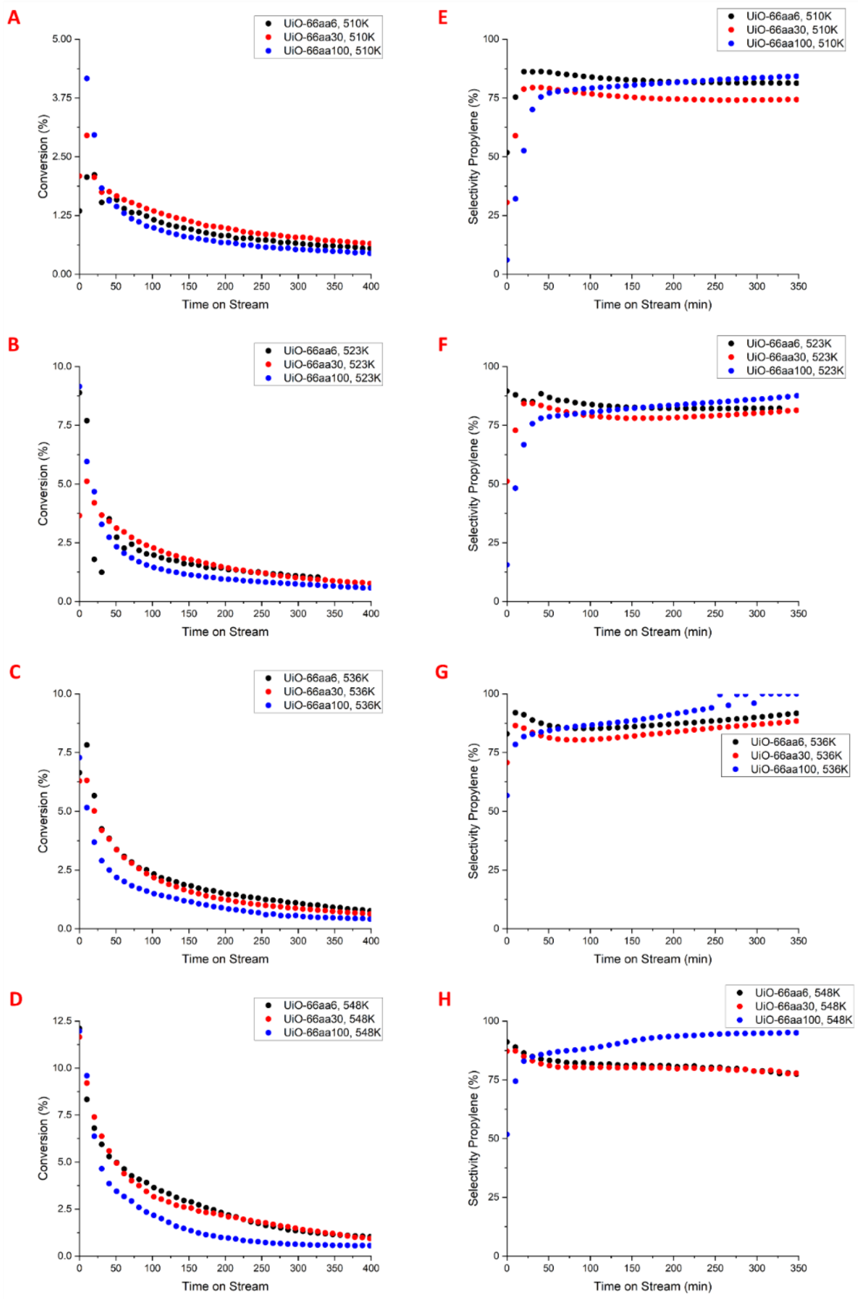

Figure A3.8: Comparison of the conversion at 510 (A), 523 (B), 536 (C), and 548 K (D) to the selectivity for propylene at the same respective temperatures (E-H) for UiO-66aa6 UiO-66aa30 and UiO-66aa100 (blue, red, black). The temperature dependence demonstrates the loss of initial ether selectivity and with changes in the selectivity trend following the first 45 minutes of time on stream. Reaction conditions: 510, 523, 536, and 548 K, feed partial pressure of 80 mbar of isopropanol and 920 mbar of helium; total flow rate 12.5 mL (NTP)/ min; catalyst mass, 25 mg of MOF and 1.00 g of α-Al_2O_3 particles mixed with mortar and pestle for 60 s.